

Title	A tight-binding analysis of the electronic properties of III-nitride semiconductors
Authors	Coughlan, Conor Terence
Publication date	2016
Original Citation	Coughlan, C. T. 2016. A tight-binding analysis of the electronic properties of III-nitride semiconductors. PhD Thesis, University College Cork.
Type of publication	Doctoral thesis
Rights	© 2016, Conor Terence Coughlan. - http://creativecommons.org/licenses/by-nc-nd/3.0/
Download date	2024-04-24 09:27:28
Item downloaded from	https://hdl.handle.net/10468/2761

A tight-binding analysis of the electronic properties of III-nitride semiconductors

Conor Terence Coughlan



Thesis submitted in partial fulfilment of the requirements
of the degree of Doctor of Philosophy

at the
Department of Physics,
University College Cork

Supervisor: Prof. Eoin O'Reilly
Head of Department: Prof. John McInerney

May 2016

Declaration of Authorship

I, Conor Terence Coughlan, declare that this thesis titled, ‘A tight binding analysis of the electronic properties of III-nitride semiconductors’ and the work presented in it are my own. I confirm that:

- This work was done wholly or mainly while in candidature for a research degree at this University.
- Where any part of this thesis has previously been submitted for a degree or any other qualification at this University or any other institution, this has been clearly stated.
- Where I have consulted the published work of others, this is always clearly attributed.
- Where I have quoted from the work of others, the source is always given. With the exception of such quotations, this thesis is entirely my own work.
- I have acknowledged all main sources of help.
- Where the thesis is based on work done by myself jointly with others, I have made clear exactly what was done by others and what I have contributed myself.

Signed:

Date:

Abstract

This thesis divides into two distinct parts, both of which are underpinned by the tight-binding model. The first part covers our implementation of the tight-binding model in conjunction with the Berry phase theory of electronic polarisation to probe the atomistic origins of spontaneous polarisation and piezoelectricity as well as attempting to accurately calculate the values and coefficients associated with these phenomena. We first develop an analytic model for the polarisation of a one-dimensional linear chain of atoms. We compare the zincblende and ideal wurtzite structures in terms of effective charges, spontaneous polarisation and piezoelectric coefficients, within a first nearest neighbour tight-binding model. We further compare these to real wurtzite structures and conclude that accurate quantitative results are beyond the scope of this model but qualitative trends can still be described. The second part of this thesis deals with implementing the tight-binding model to investigate the effect of local alloy fluctuations in bulk AlGa_N alloys and InGa_N quantum wells. We calculate the band gap evolution of Al_{1-x}Ga_xN across the full composition range and compare it to experiment as well as fitting bowing parameters to the band gap as well as to the conduction band and valence band edges. We also investigate the wavefunction character of the valence band edge to determine the composition at which the optical polarisation switches in Al_{1-x}Ga_xN alloys. Finally, we examine electron and hole localisation in InGa_N quantum wells. We show how the built-in field localises the carriers along the *c*-axis and how local alloy fluctuations strongly localise the highest hole states in the *c*-plane, while the electrons remain delocalised in the *c*-plane. We show how this localisation affects the charge density overlap and also investigate the effect of well width fluctuations on the localisation of the electrons.

Acknowledgements

This thesis began in earnest as a final year undergraduate project in the Photonics Theory Group in Tyndall. Under the guidance of my eventual Phd supervisor, Prof Eoin O' Reilly, and with the help of Masoud Seifikar I was given my first genuine experience of scientific research and I loved it! This project paved the way for a Masters which quickly evolved into a Phd. Along the way I have had the pleasure to meet and work with many wonderful people. First mention has to go to my supervisor, Eoin. I am grateful to him not only for the opportunity he gave me but also his continued support throughout my research as well as the benefit of his vast experience.

There have been many members of the Photonics Theory Group during my time there, both permanent and transient. All of whom, it has been a pleasure to work with and know. A special mention has to go to Chris Broderick who I also did my undergraduate with, Miguel Caro, Masoud Seifikar and Stefan Schulz, who I collaborated closely with on the second half of my research. I can safely say this wouldn't have happened without any of you.

To everyone I shared an office with, at one time or another, thank you for the help, enlightening conversations but most of all the entertainment. One of the most rewarding ventures I took part in during my Phd was joining the Postgraduate Committee. Through this I really got to know and appreciate the wonderful characters and personalities in the wider Tyndall community and the great work they do. Ye are a lovely bunch!

Finally, I would like to thank my friends and family for their unwavering support throughout.

Contents

Declaration of Authorship	i
Abstract	ii
Acknowledgements	iii
1 Introduction and overview	1
1.1 Background and motivation	1
1.2 Thesis outline and overview	2
2 Theory and Methods	5
2.1 Periodic Crystal Lattices	5
2.2 Tight Binding Model	8
2.3 Berry Phase Theory of Polarisation	15
2.3.1 The Adiabatic Theorem	15
2.3.2 The Berry Phase	18
2.3.3 Modern Theory of Polarisation	20
3 Berry phase polarisation calculations of III-V materials	22
3.1 Introduction	22
3.1.1 Motivation and Overview	22
3.1.2 Zinc blende and wurtzite structures	23
3.1.3 Previous work	24
3.2 Linear Chain Model	25
3.3 Numerical Implementation	31
3.3.1 Grids and Strings	31
3.3.2 Choice of Unit Cells	33
3.3.3 The Need for a Reference Structure	34
3.4 Phase surfaces and Convergence	35
3.4.1 Homopolar Test	35
3.4.2 Phase surfaces	36
3.4.3 Convergence of the number of strings	37

3.5	Zinc blende and ideal wurtzite comparison	39
3.5.1	Third Nearest Neighbors	40
3.5.2	Effective charges	42
3.5.3	Piezoelectric Coefficients	44
3.6	Real Wurtzite	48
3.6.1	Spontaneous Polarisation	48
3.6.2	Piezoelectric Coefficients	50
3.7	Conclusions	53
4	Band gap bowing and optical polarisation switching in $\text{Al}_{1-x}\text{Ga}_x\text{N}$ alloys	55
4.1	Introduction	55
4.2	Method	57
4.3	Results	60
4.3.1	AlGa _N band gap	61
4.3.2	Composition dependence of the band edge energies	62
4.3.3	Optical polarisation switching	62
4.4	Conclusions	66
5	Electron and hole localization in $\text{In}_x\text{Ga}_{1-x}\text{N}$ quantum wells	67
5.1	Introduction	67
5.2	$\text{In}_{0.25}\text{Ga}_{0.75}\text{N}$ flat quantum wells	69
5.2.1	Localisation metrics used	70
5.2.2	Participation Ratio	70
5.2.3	Charge density overlap	72
5.2.4	Probability density in a layer	74
5.2.5	Hole localisation	75
5.2.6	Hole overlap	76
5.2.7	Summary of $\text{In}_{0.25}\text{Ga}_{0.75}\text{N}$ flat QWs.	78
5.3	$\text{In}_{0.25}\text{Ga}_{0.75}\text{N}$ quantum wells with well width fluctuations	79
5.4	$\text{In}_{0.10}\text{Ga}_{0.90}\text{N}$ flat quantum wells	82
5.4.1	Participation Ratio	82
5.4.2	Probability density in a layer	83
5.4.3	Energy separation of states	84
5.4.4	Charge density overlap	84
5.4.5	Hole localisation	85
5.4.6	Hole overlap	87
5.4.7	Summary of $\text{In}_{0.10}\text{Ga}_{0.90}\text{N}$ flat QWs.	87
5.5	$\text{In}_{0.10}\text{Ga}_{0.90}\text{N}$ quantum wells with well width fluctuations	88
5.6	Conclusions	91
6	Summary, conclusions and outlook	92
6.1	Summary and Conclusions	92
6.2	Outlook and future work	95

*“The most exciting phrase to hear in science,
the one that heralds the most discoveries,
is not “Eureka!” (I found it!) but ‘That’s funny...’ ”*

Isaac Asimov.

Chapter 1

Introduction and overview

We begin this thesis with a short background and motivation, in Sec 1.1, on why we studied the electronic properties of III-nitride material using the tight-binding model. This is then followed in Sec.1.2 by an outline of the structure of the thesis and an overview of the primary results.

1.1 Background and motivation

III-nitride semiconductors are a technologically important set of materials. The alloys of InN, GaN and AlN have photon emission wavelengths that span a range from the near infrared, through the visible spectrum and into the deep ultraviolet giving them a wide range of applications. These applications include, but are not restricted to, detectors, light-emitting diodes, and lasers operating in the UV range with applications such as power electronics, optical storage, medical diagnostics and treatment, sterilization processes, Blu-ray DVD lasers and the basis for white light LEDs [1, 2]. Consequently interest in the fundamental properties of these materials has steadily grown over the past 20 years since the first demonstration of III-nitride LEDs by Nakamura and co-workers in 1993, work for which he, Amano and Akasaki were awarded the Nobel Prize for Physics in 2014.

As appealing as the applications of the III-nitride materials are, they are equally difficult to realise. One of the fundamental differences between the III-nitrides (to clarify, by III-nitrides we are referring to InN, GaN, AlN and their respective alloys) and other III-V semiconductors is the structure. The III-nitrides form in

the wurtzite crystallographic phase while III-V materials (such as arsenide- and phosphide-based compounds from which devices such as LEDs and laser diodes are commonly fabricated) form in the zincblende phase. When fabricating low-dimensional structures, such as quantum wells, wires or dots from wurtzite materials spontaneous polarisation contributes to a ‘built-in’ potential that localises electrons and holes at opposite interfaces, decreasing their overlap and also, as a result, the optical recombination efficiency of the device. Another characteristic of III-nitride materials is their strong piezoelectric response. Piezoelectricity is the name given to the phenomenon where applying strain to certain (polar) crystalline solids induces a polarisation field in the material. Strain, induced from either the large lattice mismatch at the interfaces or from local alloy fluctuations, further contributes to the built-in polarisation potential in III-nitride nanostructures. Defects in the growth of these structures also affect optical recombination in these devices, but in spite of high defect densities they still exhibit high quantum efficiencies [3, 4]. In order to better inform the growth and design of III-nitride based materials and devices, both in Tyndall and by partners in European projects (DEEPEN and ALIGHT), we investigated these processes and effects at an atomistic level.

In order to model these effects we employed the semi-empirical tight-binding model to calculate the electronic structure of III-nitride materials. The strongest features of the tight-binding (TB) model are that it is atomistic and can deal with large nanostructures (up to $\approx 10^5 - 10^6$ atoms). It employs a minimal basis set constructed from linear combinations of atomic-like orbitals. This atomic basis allows us to investigate the effect of specific interactions and to calculate the electronic structure of large supercells while still being able to include atomistic effects. We employ the TB model in conjunction with the Berry phase theory of modern polarisation to analyse the microscopic origins of spontaneous polarisation and the piezoelectric effect in wurtzite materials. We also implement the TB model to include local atomistic effects in supercell calculations of bulk $\text{Al}_{1-x}\text{Ga}_x\text{N}$ alloys and $\text{In}_x\text{Ga}_{1-x}\text{N}$ quantum wells.

1.2 Thesis outline and overview

Chapter 2, *Theory and Methods*, introduces the TB model as well as the Berry phase theory of polarisation. This chapter is written with the audience of a final

year undergraduate or first year postgraduate physics student in mind so as to serve as a general introduction to the tight-binding method. We begin with a discussion of periodic crystal lattices and how we can exploit their symmetry to simplify our calculations. Then after introducing the idea of Bloch sums we develop the TB model and show how the Hamiltonian is constructed. The foundations of the modern theory of polarisation are presented in the second half of this chapter, where we introduce the concept of the Berry Phase.

Chapter 3, *Berry phase polarisation calculations of III-V materials*, deals with our implementation of the TB model in conjunction with the modern theory of polarisation to investigate, on a microscopic scale, the piezoelectric effect and spontaneous polarisation in III-nitride semiconductors. We first present an analytic implementation of this theory by studying a linear chain of atoms. With a minimal basis of one s -orbital per site we show how the Berry phase varies linearly with strain and also linearly for small values of the bond polarity α_p . This simple model helped us to build an understanding of how to implement and benchmark the numerical calculations for the full 3-dimensional structure.

For the full 3-dimensional calculations we first show the similarity between ideal wurtzite and zincblende structures in terms of effective charges, spontaneous polarisation and piezoelectric coefficients, within a first nearest neighbour TB model. We demonstrate how accurate quantitative results are inaccessible with this model and explain how this may be due to a fundamental limitation of the model. We investigate the effect of specific third nearest neighbour interactions on the spontaneous polarisation and crystal field splitting of ideal wurtzite structures. When investigating real wurtzite (which differs from the ideal case in that not all the bond lengths and bond angles are equal) we show the parameter sensitivity of the model. We again show how quantitative results are beyond the scope of this model but demonstrate that qualitative trends can be described.

In terms of timeline, this work represents the first three years of my research. Extensive efforts were undertaken to improve the model and extract useful results but this proved, ultimately fruitless and had to be abandoned. We then changed focus for the second half of the thesis, implementing our knowledge of the TB model within supercell calculations of III-nitride alloys. In conjunction with models previously developed within the Photonics Theory Group here in Tyndall, we analysed the effect of local alloy fluctuations, on an atomistic scale, on the electronic properties of bulk $\text{Al}_{1-x}\text{Ga}_x\text{N}$ alloys and $\text{In}_x\text{Ga}_{1-x}\text{N}$ quantum wells.

In chapter 4, *Band gap bowing and optical polarisation switching in $Al_{1-x}Ga_xN$ alloys*, we present a detailed theoretical study of the band gap bowing of wurtzite AlGa_xN alloys over the full composition range. Our theoretical framework, based on the atomistic TB model, includes local strain and built-in potential variations due to random alloy fluctuations. We extract a bowing parameter for the band gap of $b = 0.94$ eV, which is in good agreement with experimental data. Our analysis shows that the bowing of the band gap mainly arises from bowing of the conduction band edge; for the composition dependence of the valence band edge energy we find a close to linear behaviour. Finally, we investigate the wave function character of the valence band edge as a function of GaN content x . Our analysis reveals an optical polarisation switching around $x = 0.75$, which is in the range of reported experimental data. This work has been accepted for publication in *Physica Status Solidi (b)*.

Chapter 5, *Electron and hole localization in $In_xGa_{1-x}N$ quantum wells*, presents our analysis of how local alloy fluctuations affect the localisation of electron and hole state in $In_xGa_{1-x}N$ quantum wells. We examined two different compositions; $In_{0.10}Ga_{0.90}N$ and $In_{0.25}Ga_{0.75}N$ for structures both with and without well width fluctuations (WWFs). The QWs with the higher InN composition of 25% were found to have a strong built-in potential which confined the carriers to opposite sides of the QW. In addition to this the local alloy variations gave rise to local strain and polarisation potential fluctuations which were found to strongly localise the highest hole states in the c -plane. This was shown to affect the charge density overlap with the electrons, which were found to be delocalised in the c -plane. The WWFs were found to strongly localise the first two electron states while having no effect on the hole states. The charge density overlap was slightly reduced compared to the flat QWs as a result of the WWFs. The $In_{0.10}Ga_{0.90}N$ QWs, as a result of their lower InN composition, had a lower built-in field. This reduced built-in field allow both the electron and hole states to extend further into the QW resulting in increased charge density overlap in general. Some of this work has been accepted for publication in *Physical Review B*, while the rest of it is currently in preparation.

Finally, in chapter 6, we present our conclusions drawn from the work presented in this thesis. We summarise the results and outline possible future areas of investigation.

Chapter 2

Theory and Methods

This chapter presents the formal theory behind the models implemented in this thesis. It begins with a discussion on periodic crystal lattices in Sec. 2.1, Sec. 2.2 introduces the semi-empirical tight binding model, both formally and practically, and finally Sec. 2.3 gives an exposition of the Berry phase theory of polarisation.

2.1 Periodic Crystal Lattices

The materials studied in this thesis are all tetrahedrally bonded crystalline solids. Our aim is to determine the electronic and optical properties of these materials, by solving the time independent Schrödinger equation (TISE):

$$\mathcal{H}\psi(\mathbf{r}) = E\psi(\mathbf{r}). \quad (2.1)$$

This is an eigenvalue problem where the Hamiltonian operator \mathcal{H} , which represents the total energy of the system, acts on a wavefunction ψ to give the energy eigenvalue E associated with ψ . The Hamiltonian takes the form

$$\mathcal{H} = \frac{p^2}{2m_0} + V_0(\mathbf{r}), \quad (2.2)$$

where p is the momentum operator and $V_0(\mathbf{r})$ is the potential, which includes terms due to the Coulomb potentials of the nuclei and the inner electrons, as well

as others due to the repulsive interaction between the valence electrons.

$$V_0(\mathbf{r}) = \frac{1}{4\pi\epsilon_0} \sum_i^N \frac{e^2 Z}{|\mathbf{r} - \mathbf{r}'|} + \dots \quad (2.3)$$

We cannot solve this Hamiltonian analytically; there are simply too many terms. Even computationally it is not possible to diagonalise this Hamiltonian with the exact potential. To proceed we make approximations to this potential. These approximations come in various flavours and varieties, and will be discussed in more detail in the next section. Before we implement any approximations, we first utilise the periodicity and symmetry of the crystal structure which are embedded in the potential.

Firstly, due to the periodic structure of the crystal the potential is invariant under translations by a lattice vector \mathbf{R}_n

$$V_0(\mathbf{r}) = V_0(\mathbf{r} + \mathbf{R}_n). \quad (2.4)$$

A lattice vector connects two identical points in an infinite crystal lattice and is expressed in terms of basis vectors \mathbf{a}_i that span the unit cell. The unit cell is the smallest part of the structure that can be copied ad infinitum in the directions of the basis vectors to create an infinite crystal, with an arbitrary lattice vector \mathbf{R}_n then given by

$$\mathbf{R}_n = \sum_i^3 n_i \mathbf{a}_i, \quad n_i \in \mathbb{Z} \quad (2.5)$$

The points connected by lattice vectors in the crystal, being identical, must also have equal electron probability distributions:

$$|\psi(\mathbf{r})|^2 = |\psi(\mathbf{r} + \mathbf{R}_n)|^2. \quad (2.6)$$

This implies that the wavefunctions themselves must be identical up to a phase factor:

$$\psi(\mathbf{r} + \mathbf{R}_n) = e^{i\phi} \psi(\mathbf{r}). \quad (2.7)$$

One possible ansatz for the form of this phase factor ϕ is:

$$\phi = \mathbf{k} \cdot \mathbf{R}_n + 2\pi N \quad (2.8)$$

where the wavenumber \mathbf{k} represents the crystal momentum and the $2\pi N$ term reflects the fact that the phase is invariant modulo 2π , which is again a consequence of the translational symmetry of the crystal. We can redefine this term as a *reciprocal lattice vector* \mathbf{G}_m :

$$e^{i\mathbf{k}\cdot\mathbf{R}_n} \equiv e^{i(\mathbf{k}+\mathbf{G}_m)\cdot\mathbf{R}_n} \quad (2.9)$$

and then expand \mathbf{G}_m in a basis \mathbf{b}_i :

$$\mathbf{G}_m = \sum_i^3 m_i \mathbf{b}_i, \quad m_i \in \mathbb{Z}. \quad (2.10)$$

If we choose \mathbf{b}_i so that:

$$\mathbf{b}_i \cdot \mathbf{a}_j = 2\pi\delta_{ij}, \quad i, j \in \{1, 2, 3\} \quad (2.11)$$

we still have:

$$\mathbf{G}_m \cdot \mathbf{R}_n = \sum_{ij} m_i n_j \mathbf{b}_i \cdot \mathbf{a}_j = 2\pi N. \quad (2.12)$$

Then, by construction, \mathbf{b}_i is orthogonal to \mathbf{a}_j and \mathbf{a}_k for $i \neq j, k$ and \mathbf{b}_i can be written as:

$$\mathbf{b}_i = c \mathbf{a}_j \times \mathbf{a}_k. \quad (2.13)$$

The scaling constant c can be found by taking the dot product of this with \mathbf{a}_i :

$$\mathbf{a}_i \cdot \mathbf{b}_i = c \mathbf{a}_i \cdot (\mathbf{a}_j \times \mathbf{a}_k) = 2\pi. \quad (2.14)$$

This then gives:

$$\mathbf{b}_i = 2\pi \frac{\mathbf{a}_j \times \mathbf{a}_k}{\mathbf{a}_i \cdot (\mathbf{a}_j \times \mathbf{a}_k)}. \quad (2.15)$$

Thus, by defining a real space unit cell spanned by the basis vectors \mathbf{a}_i we also define a reciprocal lattice unit cell spanned by \mathbf{b}_i . The real lattice unit cell, known as the *Wigner-Seitz cell*, is invariant under translations by \mathbf{R}_n and represents a reproducible part of the crystal structure that can be copied to give an infinite lattice. The reciprocal lattice unit cell, known as the *Brillouin Zone*, is invariant under translations by \mathbf{G}_m . Looking at Eq. 2.9 we can restrict k to the range $-\frac{\mathbf{G}_i}{2} \leq \mathbf{k}_i \leq \frac{\mathbf{G}_i}{2}$ (where i denotes direction) since all greater values of \mathbf{k} are accessed by adding multiples of \mathbf{G}_i . Hence this restricted range of \mathbf{k} , known as the first Brillouin zone, represents the entire dynamics of an electron in a periodic

crystal. This reciprocal space is also known as ‘ \mathbf{k} -space’ or ‘*quasi-momentum space*’, since the wave vector \mathbf{k} is related to the momentum via $\mathbf{p} = \hbar\mathbf{k}$. Formally, the reciprocal lattice is the dual of the real lattice; the reciprocal lattice of the reciprocal lattice is the real lattice. It can also be thought of as a discrete Fourier transform of the real lattice.

Considerations (similar to Eq. 2.7) of what form the wave function of an electron in a periodic crystal should take lead F. Bloch to formulate the theorem that takes his name. It states that the wave function can be described as the product of a slowly varying plane wave times a rapidly varying cell periodic function, known as the Bloch function. The plane wave part describes the extended behaviour of the state due to the periodicity of the crystal.

$$\psi_n(\mathbf{k}, \mathbf{r}) = e^{i\mathbf{k}\cdot\mathbf{r}} u_n(\mathbf{k}, \mathbf{r}). \quad (2.16)$$

The Bloch function, $u_n(\mathbf{k}, \mathbf{r})$, changes spatially on an atomic scale and describes the variation within the unit cell. These wave functions are complete and orthonormal,

$$\int_{\Omega} d^3r \psi_n^*(\mathbf{k}, \mathbf{r}) \psi_{n'}(\mathbf{k}', \mathbf{r}) = \delta_{n,n'} \delta_{\mathbf{k},\mathbf{k}'} \quad (2.17)$$

where Ω is the unit cell volume. The wave functions are normalized to the unit cell volume since we employ periodic boundary conditions. Periodic boundary conditions assume that one surface of the unit cell is connected to the opposite surface, for each direction (i.e. in an orthorhombic cell the top surface is connected to the bottom, left to right and back to front). These periodic boundary conditions allow us to model infinite crystals with a finite number of atoms while also eliminating surface effects.

2.2 Tight Binding Model

We now turn our attention to the tight binding (TB) model, the central method employed in this thesis to calculate the allowed energies and corresponding eigenvectors of an electron in a crystal lattice. The TB model evolved from the linear combination of atomic orbitals (LCAO) model and its name contains the first approximation of the TB model; the wave functions are described by a superposition

of the electron states of the isolated atoms:

$$\psi(\mathbf{r}) = \sum_n a_n \phi_n(\mathbf{r}). \quad (2.18)$$

The next assumption made by this model is contained within its own name: namely that the electrons are tightly bound to their respective atoms. This model is most appropriate when electrons move slowly through the crystal, or not at all in the case of an insulator, and therefore ‘belong’ to an atom for an appreciable amount of time before they move on. This means electrons on neighbouring sites have little overlap and next or second nearest neighbours (NN) have negligible overlap as the relevant overlap integrals decrease exponentially with distance. As a result, only first NN interactions are taken into account in our model. The basis of isolated atoms used consists of the valence electrons that contribute to bonding and antibonding states. To model the valence bands and also the first conduction band near the zone centre, an sp^3 basis of one s -like and three p -like states is sufficient. To improve the fitting of the conduction band another excited s -like state, known as s^* , is required. For a proper description of further excited states higher up in the conduction band five d -like orbitals are implemented. The work presented in this thesis is primarily concerned with the behaviour of the valence bands and the lowest conduction band so sp^3 and sp^3s^* basis sets are sufficient. We can write a Bloch sum of these isolated atomic orbitals as

$$\psi_{i\alpha}(\mathbf{k}, \mathbf{r}) = \frac{1}{\sqrt{N}} \sum_{\mathbf{R}} e^{i\mathbf{k} \cdot (\mathbf{R} + \mathbf{r}_i)} \phi_{\alpha}(\mathbf{r} - \mathbf{r}_i), \quad (2.19)$$

where the index i is a site index which runs over the atoms in the unit cell, \mathbf{r}_i is the position of each atom in the unit cell, α represents the orbital type (s, p, d etc.) and N is the number of unit cells included in the sum. We can therefore expand the wave function for a given state in a basis of these Bloch sums

$$\Psi(\mathbf{k}, \mathbf{r}) = \sum_n a_n(\mathbf{k}) \psi_n(\mathbf{k}, \mathbf{r}), \quad (2.20)$$

$$\Psi(\mathbf{k}, \mathbf{r}) = \frac{1}{\sqrt{N}} \sum_{i,\alpha} a_{i\alpha}(\mathbf{k}) e^{i\mathbf{k} \cdot (\mathbf{R} + \mathbf{r}_i)} \phi_{\alpha}(\mathbf{r} - \mathbf{r}_i). \quad (2.21)$$

Here n is a composite index of i and α . We now substitute this into Eq. 2.1 (TISE), multiply on the left by the conjugate of an arbitrary state $\psi_m(\mathbf{k}, \mathbf{r})$ and integrate

over the crystal, which gives us

$$\sum_n \mathcal{H}_{m,n}(\mathbf{k}) a_n(\mathbf{k}) = E(\mathbf{k}) \sum_n \mathcal{S}_{m,n}(\mathbf{k}) a_n(\mathbf{k}), \quad (2.22)$$

where the matrix elements of the tight binding Hamiltonian $\mathcal{H}_{m,n}(\mathbf{k})$ are given by;

$$\mathcal{H}_{m,n}(\mathbf{k}) \equiv \int d^3r \psi_m^*(\mathbf{k}, \mathbf{r}) \mathcal{H} \psi_n(\mathbf{k}, \mathbf{r}) \quad (2.23)$$

and the overlap matrix, $\mathcal{S}_{m,n}(\mathbf{k})$ is

$$\mathcal{S}_{m,n}(\mathbf{k}) \equiv \int d^3r \psi_m^*(\mathbf{k}, \mathbf{r}) \psi_n(\mathbf{k}, \mathbf{r}). \quad (2.24)$$

Expanding out the integral in Eq. 2.23, with the state m being denoted by the basis state β and site j ,

$$\begin{aligned} \mathcal{H}_{m,n} &= \mathcal{H}_{j,\beta;i,\alpha}(\mathbf{k}) = \\ &= \frac{1}{N} \sum_{\mathbf{R}_1, \mathbf{R}_2} e^{i\mathbf{k} \cdot (\mathbf{R}_1 - \mathbf{R}_2 + \mathbf{r}_i - \mathbf{r}_j)} \int d^3r \phi_\beta^*(\mathbf{r} - \mathbf{R}_2 - \mathbf{r}_j) \mathcal{H} \phi_\alpha(\mathbf{r} - \mathbf{R}_1 - \mathbf{r}_i) \end{aligned} \quad (2.25)$$

We can change the sum over \mathbf{R}_2 to a sum over the difference between \mathbf{R}_1 and \mathbf{R}_2 , $\mathbf{R} = \mathbf{R}_1 - \mathbf{R}_2$. The sum over \mathbf{R}_1 then just gives a factor of N , the number of unit cells in the calculation and we have:

$$\mathcal{H}_{m,n} = e^{i\mathbf{k} \cdot (\mathbf{r}_j - \mathbf{r}_i)} \int d^3r \phi_\beta^*(\mathbf{r}) \sum_{\mathbf{R}} e^{i\mathbf{k} \cdot \mathbf{R}} \mathcal{H} \phi_\alpha(\mathbf{r} - \mathbf{R}) \quad (2.26)$$

The integral in Eq. 2.26 represents the probability that an electron on atom i , orbital α will ‘hop’ to atom j , orbital β . It is the amount by which the Hamiltonian couples the two orbitals. If the two orbitals $\phi_{i\alpha}$ and $\phi_{j\beta}$ are far enough apart their overlap goes to zero and their interaction can be neglected. Again, to reiterate, we restrict our model to first NN interactions and special cases of second and third NN interactions for this reason. Note that an analogous expression to Eq. 2.26 can be derived for the overlap matrix $\mathcal{S}_{m,n}(\mathbf{k})$ but this is not necessary since, at a given \mathbf{k} value we can choose that these states are, by construction, complete and orthonormal.

$$\mathcal{S}_{m,n}(\mathbf{k}) = \delta_{mn}. \quad (2.27)$$

We first deal with what are known as the ‘*on-site*’ matrix elements of the Hamiltonian $\langle \phi_n | \mathcal{H} | \phi_n \rangle$ (using Dirac notation). Since the ϕ orbitals are built from an initial basis of isolated atomic orbitals, the energies of these terms follow similar trends to the atomic eigenvalues. Different orbitals on the same site, being orthonormal, have no overlap and thus the corresponding matrix elements are set to zero.

$$\langle \phi_{i\beta} | \mathcal{H} | \phi_{i\alpha} \rangle = \epsilon_\alpha \delta_{\alpha\beta} \quad (2.28)$$

Adjustments are commonly made to these eigenvalues to model effects due to asymmetries in the crystal. These asymmetries, which can be due to internal properties of the crystal (*e.g.* crystal field splitting) or external influences (*e.g.* strain) cause a splitting in some eigenvalues that would otherwise be degenerate. More detail of these methods is given in Sec. 4.2; for the moment it is sufficient to say that the on-site matrix elements are fitted by starting from their respective atomic eigenvalues.

The interaction terms $\langle \phi_m | \mathcal{H} | \phi_n \rangle$, also known as ‘*hopping*’ matrix elements, contain potentials from three different atoms requiring numerous and difficult three centre integrals to be calculated. Slater and Koster [5] introduced a two centre integral approximation in which the effects of the three centre terms can be neglected or incorporated into the two centre approach. In their paper Slater and Koster provide a formalism for evaluating the hopping matrix elements in terms of these two centre integrals and direction cosines. Direction cosines are the projection of an orbital’s amplitude in the direction of a bond vector joining two atoms.

The direction cosines associated with a hopping matrix element gives the proportion of the relevant orbitals pointing along the vector joining their two sites. In some sense it is a measure of the overlap of the two orbitals. The strength or magnitude of the interaction is given by the two centre integral parameters or interaction parameters.

For an sp^3 or sp^3s^* basis the interaction parameters are classified into two different types σ and π (there is a third, δ , but this is only associated with d -states). These parameters are depicted in Fig. 2.1. $V_{ss\sigma}$ models two interacting s -states. $V_{sa p_c \sigma}$ and $V_{sc p_a \sigma}$ represent the interactions between an s -state and one of the lobes of a p -state, the difference between them being where the states are situated- on the cations (c) or anions (a). Interactions between two p -states are split between two terms, $V_{pp\sigma}$ and $V_{pp\pi}$. The σ term describes that part of the interaction that

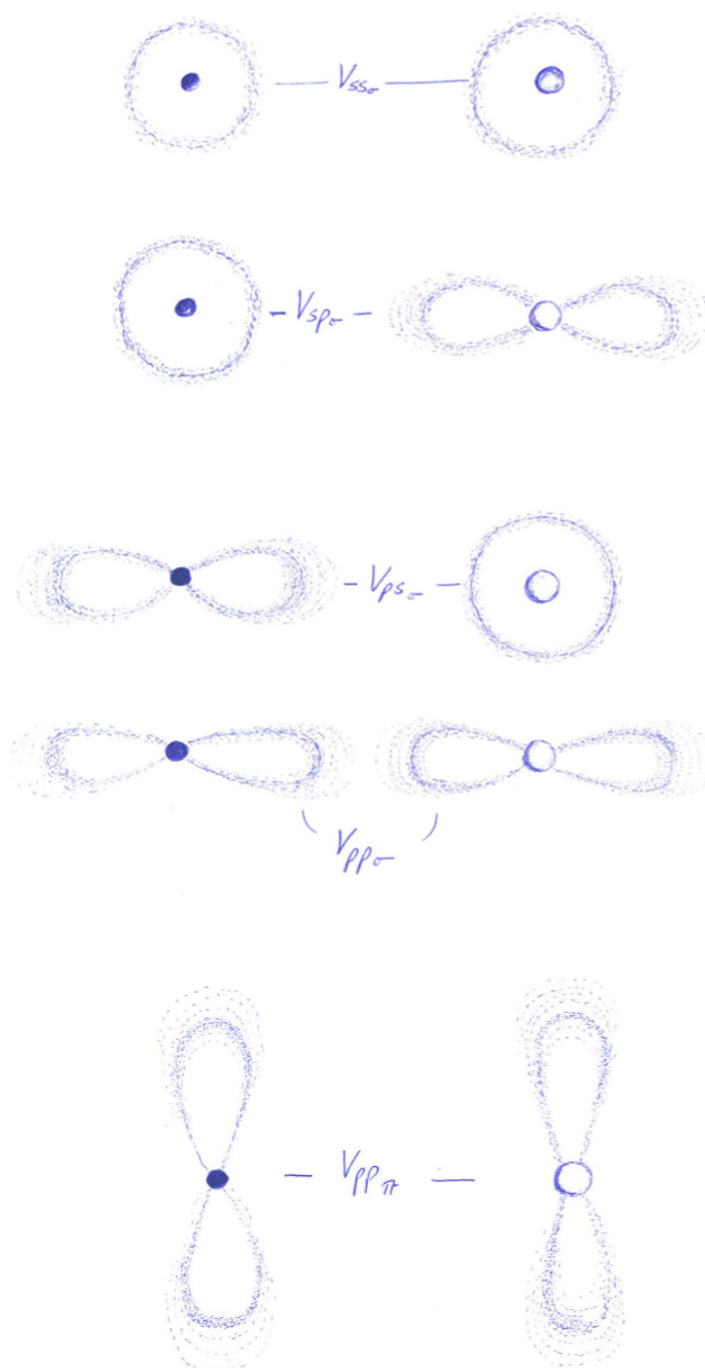


FIGURE 2.1: An “artist’s”(!) impression of the different types of two centre integral parameters for s and p type orbitals

results from the fraction of the lobes that are pointed directly towards each other while the π term describes the contribution from the fraction of the p -states that are aligned in parallel, as depicted below in Fig. 2.2.

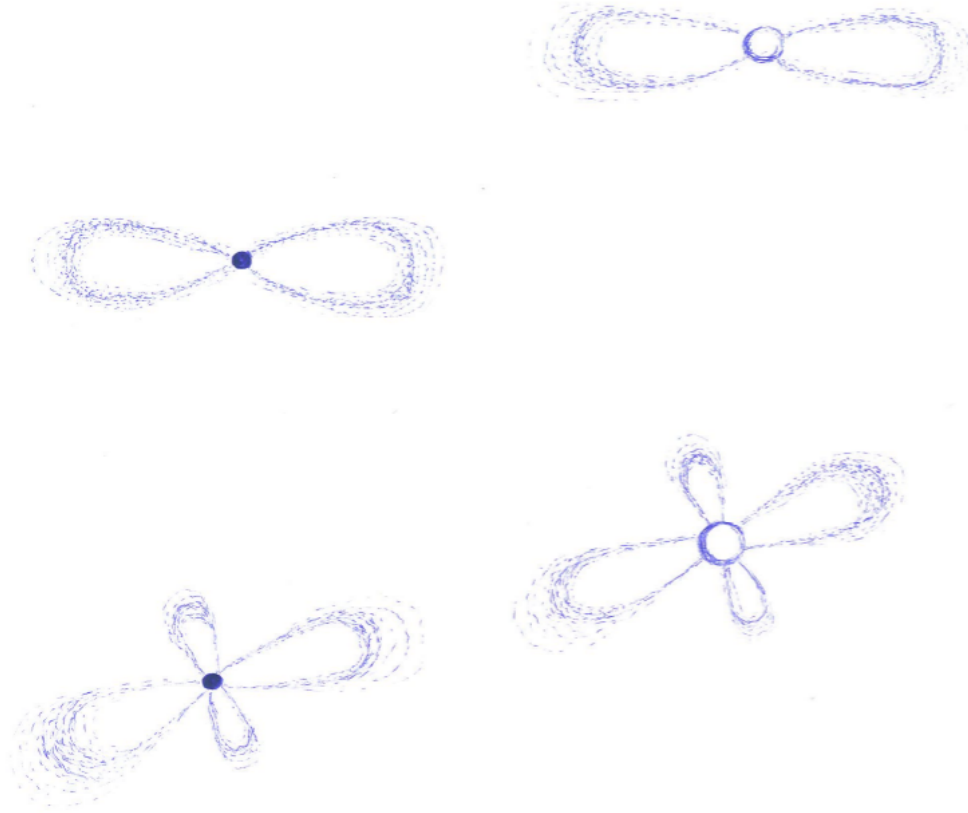


FIGURE 2.2: The decomposition of two p_x orbitals in directions normal and parallel to the bond vector, that contribute to the π and σ interactions respectively.

The interaction terms for the s^* orbitals mirror the form of those for the s states. In practice however, the $V_{ss^*\sigma}$ and $V_{s^*s^*\sigma}$ are generally neglected in the sp^3s^* Hamiltonian as the $V_{s^*p\sigma}$ terms provide the required modulation of the conduction band.

These interaction parameters are combined with the direction cosines to give the relevant Hamiltonian matrix elements, according to the following formalism provided by Slater and Koster:

$$\langle s | \mathcal{H} | s \rangle = V_{ss\sigma} \quad (2.29)$$

$$\langle s | \mathcal{H} | p_x \rangle = l(V_{sp\sigma}) \quad (2.30)$$

$$\langle p_x | \mathcal{H} | p_x \rangle = l^2(V_{pp\sigma}) + (1 - l^2)(V_{pp\pi}) \quad (2.31)$$

$$\langle p_x | \mathcal{H} | p_y \rangle = lm(V_{pp\sigma}) - lm(V_{pp\pi}) \quad (2.32)$$

$$\langle p_x | \mathcal{H} | p_z \rangle = ln(V_{pp\sigma}) - ln(V_{pp\pi}) \quad (2.33)$$

where l , m , and n are the direction cosines of the bond vector. In our model, because we deal with III-V materials which are binary compounds, we distinguish between two types of $V_{sp\sigma}$ interaction, namely $V_{s_a p_c \sigma}$ and $V_{s_c p_a \sigma}$. These specify on which atomic species the particular orbitals are based, i.e if the s orbital is on the cation or anion site.

Particular care must be given as to how the sign of these interaction terms are assigned. The rigorous way to do this is to take the absolute value of the direction cosines and obtain the sign from the sign of the interacting orbital lobes. The s states are defined to be positive and p states have both positive and negative lobes. If two positive lobes are overlapping it gives a negative interaction and if two lobes of opposite sign interact it gives a positive interaction term. It is for this reason that $V_{ss\sigma}$ and $V_{pp\pi}$ are defined as negative. An issue arises when the p orbitals are interacting with their neighbouring s states. The p orbitals are generally, by convention chosen to be oriented with their positive lobes along the positive directions of the cartesian axes. This means that the p states have the same symmetry, in terms of sign, as the axes and hence also the direction cosines. The s states, being spherically symmetric (positive in all directions) do not have this symmetry.

The sign of the interactions between an s and a p_x orbital placed at the origin and along the positive axis then depends on whether the p -state is placed at the origin ($V_{ps\sigma}$) or the s -state is at the origin ($V_{sp\sigma}$). By convention it is presumed that the first of the two states named in the subscript is at the origin and so $V_{ps\sigma}$ is taken to be negative (positive orbital overlap) and $V_{sp\sigma}$ is taken to be positive (positive s orbital overlapping with negative p orbital lobe). This issue also applies to the s^* states since they have the same symmetry as the s states.

Before we construct our tight-binding Hamiltonian with the on-site energies and hopping matrix elements we must first deal with how strain affects the eigenvalues and eigenvectors of the crystal. One approach to model the effects of strain on the band structure is to introduce corrections to the on-site energies [6, 7]- we follow this approach in chapters 4 and 5. This procedure only fits the band structure correctly at the zone centre ($\mathbf{k} = 0$, also known as the Γ point) and certain other high symmetry points. To model the strain effects on the full band structure bond length scaling and bond bending terms are introduced. The bond length scaling terms are taken to depend on the ratio of the equilibrium bond length (d_0) over the strained bond length (d) raised to the power of a free parameter (η). How

the Hamiltonian matrix elements change due to a change in bond angle is already included through the way the direction cosines are defined. The interaction terms are then scaled by these terms,

$$V_{\alpha\beta'm} \left(\frac{d_0}{d} \right)^{\eta_{\alpha\beta'm}} \quad (2.34)$$

where α and β are indices over basis states and m is the interaction type. The scaling exponents were originally set to 2 by Harrison, based on band structure scaling arguments [8]. However setting all the exponents to 2 does not provide a good description of the strain dependence of high symmetry energy states. Therefore, several authors have developed exponent sets chosen to give an improved fit to key deformation potentials, which we follow in chapter 3 in our Berry phase analysis of spontaneous polarisation and piezoelectricity.

The method of making corrections to the on-site energies is described in more detail in chapters 4 and 5, where it is used to help determine the effects of local strain due to alloy fluctuations in both bulk III-nitrides and quantum well structures.

2.3 Berry Phase Theory of Polarisation

We now turn our attention to how the wavefunctions, calculated from the tight binding model, are used to calculate the electronic polarisation in periodic crystals. The method is known as the Berry phase theory of polarisation and has its roots in the adiabatic theorem of quantum mechanics.

2.3.1 The Adiabatic Theorem

The adiabatic theorem was first proven by Born and Fock in 1928 [9] and states that if a particle is initially in the n th eigenstate of the Hamiltonian \mathcal{H} and the Hamiltonian evolves sufficiently slowly in time then the particle will remain in the n th eigenstate of the final Hamiltonian. We will now give a brief proof of this to show the origins of the Berry phase.¹

¹This proof follows that given by D. Griffiths [10].

As mentioned in the previous section the TISE gives the allowed eigenvalues and eigenvectors of a system if the Hamiltonian is independent of time. The states then evolve by picking up a phase factor, known as the dynamical phase,

$$\Psi_n(t) = \psi_n e^{-iE_n t/\hbar} \quad (2.35)$$

where E_n is the eigenvalue corresponding to the state ψ_n . (Note that the position dependence of the system is implied but not explicitly stated, as we are only interested here in the time dependence.) When the Hamiltonian changes with time the eigenvalues and eigenvectors are also time dependent:

$$\mathcal{H}(t)\psi_n(t) = E_n(t)\psi_n(t). \quad (2.36)$$

These eigenvectors form an instantaneous orthonormal set

$$\langle \psi_n(t) | \psi_m(t) \rangle = \delta_{nm} \quad (2.37)$$

and are also complete. As a result the general solution to the time dependent Schrödinger equation (TDSE)

$$\mathcal{H}(t)\Psi(t) = i\hbar \frac{\partial}{\partial t} \Psi(t) \quad (2.38)$$

can be written as a linear combination of the instantaneous eigenvectors

$$\Psi(t) = \sum_n c_n(t) \psi_n(t) e^{i\theta_n(t)} \quad (2.39)$$

where

$$\theta_n(t) = -\frac{1}{\hbar} \int_0^t E_n(t') dt' \quad (2.40)$$

represents the dynamical phase. We can substitute Eq. 2.39 into Eq. 2.38 to give

$$i\hbar \sum_n \left[\dot{c}_n \psi_n + c_n \dot{\psi}_n + i c_n \psi_n \dot{\theta}_n \right] e^{i\theta_n} = \sum_n c_n \mathcal{H} \psi_n e^{i\theta_n}. \quad (2.41)$$

The $\dot{\theta}_n$ term gives $-E_n/\hbar$ so by Eq. 2.36 the third term on the left cancels with the term on the right, leaving

$$\sum_n \dot{c}_n \psi_n e^{i\theta_n} = - \sum_n c_n \dot{\psi}_n e^{i\theta_n} \quad (2.42)$$

If we take the inner product with arbitrary eigenvector $\langle \psi_m |$, and using the fact that the eigenvectors are instantaneously orthonormal, we have on the left $\langle \psi_m | \psi_n \rangle = \delta_{mn}$ which gives

$$\dot{c}_m(t) = - \sum_n c_n \langle \psi_m | \dot{\psi}_n \rangle e^{i(\theta_n - \theta_m)}. \quad (2.43)$$

In order to evaluate the $\langle \psi_m | \dot{\psi}_n \rangle$ term we differentiate Eq. 2.36 with respect to time

$$\dot{\mathcal{H}}\psi_n + \mathcal{H}\dot{\psi}_n = \dot{E}_n\psi_n + E_n\dot{\psi}_n, \quad (2.44)$$

and, again, taking the inner product with $\langle \psi_m |$

$$\langle \psi_m | \dot{\mathcal{H}} | \psi_n \rangle + \langle \psi_m | \mathcal{H} | \dot{\psi}_n \rangle = \dot{E}_n \delta_{mn} + E_n \langle \psi_m | \dot{\psi}_n \rangle \quad (2.45)$$

Noting that, again by Eq. 2.36, $\langle \psi_m | \mathcal{H} | \dot{\psi}_n \rangle = E_m \langle \psi_m | \dot{\psi}_n \rangle$ for $n \neq m$ we then have

$$\langle \psi_m | \dot{\mathcal{H}} | \psi_n \rangle = (E_n - E_m) \langle \psi_m | \dot{\psi}_n \rangle. \quad (2.46)$$

Inserting this into Eq. 2.43 we get

$$\dot{c}_m(t) = -c_m \langle \psi_m | \dot{\psi}_m \rangle - \sum_{n \neq m} c_n \frac{\langle \psi_m | \dot{\mathcal{H}} | \psi_n \rangle}{(E_n - E_m)} e^{(-i/\hbar) \int_0^t [E_n(t') - E_m(t')] dt'} \quad (2.47)$$

There are two important things to note at this point. Firstly it is obvious from the denominator in Eq. 2.47 that we are assuming that none of the eigenvalues are degenerate. This is an important issue in implementing these calculations and will be revisited later. Secondly up to this point the above expression is exact. We now implement the adiabatic approximation by assuming that $\dot{\mathcal{H}}$ is very small. (This is not a trivial thing to prove rigorously, see [11]). Hence the sum over $n \neq m$ drops out leaving

$$\dot{c}_m(t) = -c_m \langle \psi_m | \dot{\psi}_m \rangle \quad (2.48)$$

which is a linear first order differential equation with the solution

$$c_m(t) = c_m(0) e^{i\gamma_m(t)} \quad (2.49)$$

where

$$\gamma_m(t) = i \int_0^t \left\langle \psi_m(t') \left| \frac{\partial}{\partial t'} \psi_m(t') \right. \right\rangle dt' \quad (2.50)$$

Thus, if a particle starts out in the n th eigenstate (which means $c_n(0) = 1$ and then $c_m(0) = 0$ for all m) and the Hamiltonian evolves adiabatically then the particle remains in the n th eigenstate and has changed only by a phase factor

$$\Psi_n(t) = e^{i\theta_n(t)} e^{i\gamma_n(t)} \psi_n(t). \quad (2.51)$$

This is the adiabatic theorem as stated, QED. The quantity γ_n is the phase change in a wavefunction as the system changes adiabatically from an initial state at time $t' = 0$ to some final point $t' = t$. A geometric phase, as these type of phase changes are generally known, can arise from a change in any ‘slowly’ varying parameter on which the Hamiltonian is implicitly dependent.

2.3.2 The Berry Phase

When Born and Fock originally proved the adiabatic theorem in 1928 [9] they correctly suggested that the geometric phase could be cancelled out by a change of gauge and hence ignored it. The translational invariance of any closed system means that a coordinate transformation, a shift of the origin, simply induces a phase shift in the system which does not change the physics of the system. Thus by selecting the change of gauge that induces an equal and opposite phase change to that of the geometric phase, Born and Fock argued that the geometric phase can be ignored. The idea of geometric phase lay dormant for the best part of thirty years until S. Pancharatnam discovered that the phase difference between two nonorthogonal states of polarized light had geometric origins [12]. However it was not until Michael Berry’s seminal paper in 1984 [13] that the geometric phase came to prominence again. He showed that geometric phases that resulted from adiabatic and importantly *cyclic* evolutions are gauge invariant and consequently have real observable effects. The Berry phase can be defined generally as

$$\gamma_n(C) = i \int_C \langle \psi_n(R) | \nabla_R | \psi_n(R) \rangle dR \quad (2.52)$$

where R is any adiabatically varying parameter on which the system depends and C is the closed path traced out by R in its parameter space. As a result of the closed path requirement all changes of gauge cancel in the inner product giving a nontrivial γ . The inner product that is integrated over is known as the gauge potential or Berry connection, and this is gauge dependent. A simple example of

a Berry phase is that of parallel transport. Imagine a vector at the north pole of a sphere and pointing in an arbitrary direction. If this vector is transported in a closed loop down a line of longitude to the equator, across the equator and back to the north pole via any other line of longitude the vector is then pointing in a new direction. The angle between the old and new direction is equivalent to the solid angle enclosed by the closed loop traversed and is also the geometric phase picked up by the process. Effects resulting from geometric phases are often described as 'global change without local change'. Foucault's pendulum, falling cats and parallel parking are all everyday examples of this [14]. ²

In light of this discovery, many phenomena were realised in retrospect to be manifestations of a geometric phase. Pancharatnam obviously was credited with the first discovery, though it is still more commonly called the Berry phase. Mead and Truhlar [16] when considering the Born-Oppenheimer approximation revealed an additional geometric phase but they neglected it for similar reasons to Born and Fock. The Guoy effect, a result of something called the Bargmann invariant, was also realised to be equivalent to the Berry phase [17]. In 1959 Aharonov and Bohm postulated that a potential is in itself a fundamental physical entity (a new idea at the time) and that a nonzero vector potential could still interact with an electron in the absence of an electric or magnetic field and hence any acting force [18]. This was shown to have its roots in a geometric phase. The Jahn Teller effect [19] and quantum Hall effect [20] are also explained in terms of a geometric phase.

After Michael Berry's paper in 1984 there were many extensions and generalisations of the idea. The more important ones for our interests are Wilczek and Zee's generalisation for degenerate Hamiltonians [21] and Zak's derivation of the Berry phase for energy bands in a solid [22]. Wilczek and Zee's work is important because it allows us to deal with band crossings which otherwise create poles in Eq. 2.47. Zak makes use of the periodicity of the Brillouin zone to form a closed path and thus reduces the calculation to an integral over a one-dimensional parameter space.

²This phenomenon, known as anholonomy in physics or holonomy in mathematics, was already known to Gauss. In mathematics holonomy is described by Hannay angles [15].

2.3.3 Modern Theory of Polarisation

Classically, the polarisation of a crystalline solid is defined as the integrated dipole moment of the charged particles within a unit cell divided by the cell volume Ω_0

$$\Delta \mathbf{P} = \frac{1}{\Omega_0} \int_{\Omega_0} d^3 \mathbf{r} \mathbf{r} \rho(\mathbf{r}) \quad (2.53)$$

where $\rho(\mathbf{r})$ is the charge density. Due to the delocalised nature of the electrons it is not possible to define the polarisation in this way without introducing a dependency on the shape of the cell. A breakthrough came when Resta [23] and also Vanderbilt and King-Smith [24] developed what became known as the modern theory of polarisation. Resta proposed that the change in the electronic contribution to the polarisation is due to an adiabatic current flowing through the crystal. This current is induced by an adiabatic change in a parameter upon which the crystal Hamiltonian implicitly depends (e.g. strain, temperature, electric field or sub-lattice displacements etc.).

$$\Delta \mathbf{P}_e = \Delta \mathbf{P}_e(\Delta t) - \Delta \mathbf{P}_e(0) = \int_0^{\Delta t} dt \mathbf{j}(t). \quad (2.54)$$

This was then interpreted in terms of geometric phases and the electronic polarisation was recast as

$$\Delta \mathbf{P}_e = -\frac{if|e|}{(2\pi)^3} \sum_{n=1}^M \int_{BZ} d^3 \mathbf{k} \langle u_{n\mathbf{k}} | \nabla_{\mathbf{k}} | u_{n\mathbf{k}} \rangle \quad (2.55)$$

where f is the occupation number of the states, $u_{n\mathbf{k}}$ is the cell periodic part of the Bloch wavefunction $\psi_{n\mathbf{k}}$ and M is the number of occupied bands. The integrand is of course the Berry connection. There are two important things to note here. Firstly, because of the closed path requirement of the Berry phase formalism we can only calculate polarisation differences, from an initial state to a final state. Secondly, since Eq. 2.55 is effectively the Berry phase times a constant factor, and the phase is defined modulo 2π , the polarisation is defined modulo $\frac{e\mathbf{R}}{\Omega}$ (where \mathbf{R} is a lattice constant parallel to \mathbf{P}). Numerically Eq. 2.55 is implemented as

$$P_{e_i} = -\frac{fe(\Delta \mathbf{k})^2}{(2\pi)^3} \sum_{\mathbf{k}_{\perp}} \Phi_{\mathbf{k}_{\perp}} \quad (2.56)$$

where $\Phi(\mathbf{k})$, the Berry phase, is calculated as

$$\Phi_{\mathbf{k}_\perp} = \text{Im} \ln \prod_{j=0}^{J-1} \det \langle u_{m,\mathbf{k}_\perp,\mathbf{k}_j} | u_{n,\mathbf{k}_\perp,\mathbf{k}_{j+1}} \rangle. \quad (2.57)$$

This represents a discretization of the Brillouin zone into a mesh of parallel strings each positioned at \mathbf{k}_\perp and divided into J points, denoted by \mathbf{k}_j . This is clarified in the next chapter.

The numerical implementation of this model for calculating the spontaneous and piezoelectric polarisation of group III-V materials in both wurtzite and zinc blende structures is the focus of chapter 3.

Chapter 3

Berry phase polarisation calculations of III-V materials

3.1 Introduction

3.1.1 Motivation and Overview

We present in this chapter our implementation of the tight-binding model in conjunction with the Berry phase theory of polarisation. The TB method has, overall, proved very useful in describing many properties of III-V and related materials, as we will show in chapters 4 & 5. This motivates the question of whether we can use the TB method with the Berry phase theory of polarisation to provide an atomistic description of the contributing factors to spontaneous polarisation (P_{spont}), effective charges and the piezoelectric (PZ) effect. The PZ effect and P_{spont} are well documented processes in the growth and band structure engineering of semiconductor heterostructures. There was, however, when this study began, no clear understanding of trends in these effects at a microscopic level. The TB model gives us an atomistic description of the electronic structure of III-nitride materials. It also allows us to examine the contributions from specific interactions to the polarisation properties of these materials.

We begin the chapter by presenting a fully analytic model of a linear chain of atoms that shows how the Berry phase varies as strain, polarity and asymmetries in the interaction potentials are introduced. We show how, for small values of these

parameters, the Berry phase of the system changes linearly and as the polarity increases non-linear effects become more dominant. We then discuss some of the technical considerations involved in the numerical calculation such as convergence and the mesh of \mathbf{k} points used. Finally, we present our numerical results. We show the similarity of zinc blende (ZB) and ideal wurtzite(WZ) structures, within our TB description, in terms of P_{spn} , effective charges and PZ coefficients. The same properties are then calculated for real WZ structures and we demonstrate that, although the model gives a reasonable qualitative description of the electronic polarisation, accurate quantitative results that depend on the total polarisation are beyond the scope of this model.

3.1.2 Zinc blende and wurtzite structures

We now introduce the specific structures we examined. Fig. 3.1 shows a 12 atom, [111] oriented zinc blende (ZB) unit cell, a 12 atom ideal wurtzite (WZ) cell and a 12 atom real WZ cell. The Bravais lattice of the ZB system is face-centered cubic (FCC), while the Bravais lattice of the WZ structure is hexagonal-closed-packed (HCP). The ZB structure consists of two interpenetrating FCC lattices, one consisting of cations and the other of anions, offset along the diagonal of the cell by one bond length. The WZ structure can be thought of as two interpenetrating HCP lattices offset by $5/8$ of the c -lattice vector along the c -axis. When looking at the ZB structure along the [111]-direction and the WZ structure along the c -axis ([0001]-direction) we see how the individual layers of atoms are very similar and the atoms in both are arranged hexagonally giving them a C_{3v} symmetry. The difference between the two structures is how these layers are stacked. The main difference between ZB and ideal WZ can be seen by looking at the atom labelled ‘E’ in the ZB cell (third red atom from the bottom). In the WZ structures this atom is placed directly above atoms ‘A’ and ‘B’, it has undergone a rotation of 180° (because of the tetrahedral structure, this is equivalent to a 60° rotation). If you translate atom ‘A’ through atom ‘C’ in ZB you reach the same position as atom ‘E’. Applying the same operation to the ideal WZ cell does not find another anion or cation. Real WZ, as the name suggests is the geometry that is the most energetically stable and hence found in nature. Ideal WZ is a hypothetical structure that is strained so that all the bond lengths and bond angles are equal and hence has the same tetrahedral environment as ZB. In real WZ there are internal asymmetries in the tetrahedra denoted by two dimensionless parameters

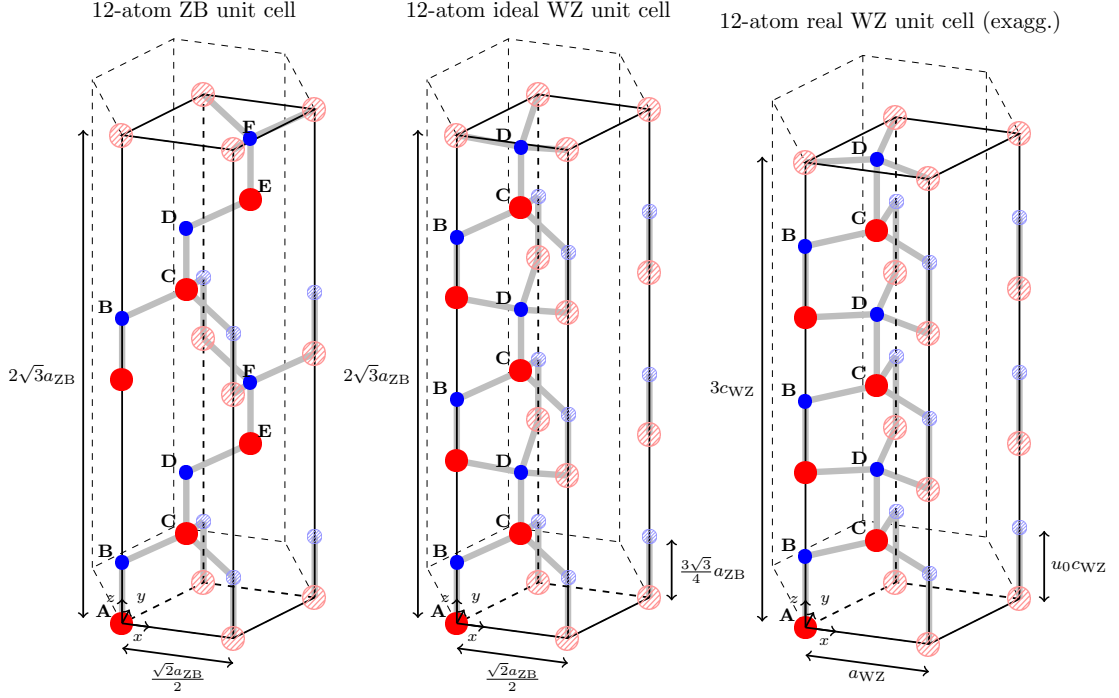


FIGURE 3.1: 12 atom unit cells for ZB, ideal WZ and real WZ (Taken from the thesis of Dr. Miguel Caro with authors permission).

u and c/a . The *internal displacement parameter* u scales the bond length of the bond oriented along the \mathbf{c} axis only. The c/a ratio has the effect of changing the bond angles and also slightly changing the bond lengths of the other three bonds. These effects are exaggerated in the real WZ unit cell depicted in Fig. 3.1.

3.1.3 Previous work

There were three previous investigations which implemented the model as we have; Bennetto and Vanderbilt [25], Di Ventura and Fernandez [26] and Iessi *et al* [27]. All three attempted to calculate Born effective charges by measuring the polarisation induced due to a sub-lattice shift. Bennetto and Vanderbilt reported a consistent underestimation of the published experimental values by a factor of 20%. They also noted that the two improvements they tried to make to the model “were actually found to lead to a worsening agreement with experiment”. These two improvements involved including the non-orthogonality of the wavefunctions and using an off diagonal position operator. Di Ventura and Fernandez presented similar findings but noted that the use of an extended basis set including an excited s^* orbital does offer some small improvement. Iesse *et al* focused on the sensitivity of the results to the values of scaling exponents used. They also showed that

in the tight-binding model, when using a diagonal position operator, the Bloch phase (the plane wave factor in the wavefunctions) cancels out in Eq. 3.28. For these reasons we also used a diagonal position operator. All of the issues raised by these papers are addressed at different stages in this chapter. We still required more insight into the model than was available in the published literature. It was for this purpose we examined a simple one-dimensional model of a distorted linear chain of atoms and analytically calculated the Berry phase as various factors were changed. The purpose of this was not only to develop an understanding and intuition for trends in the piezoelectric response but also as a method to develop simple benchmark tests for the full numerical 3D calculation.

3.2 Linear Chain Model

The model we set up was a linear chain of atoms with one s-orbital per site and two atoms per unit cell. Specific cases were then examined to probe the effects of various parameters on the Berry phase, e.g strain, polarity and asymmetry in the tight-binding interaction parameters. The general model, presented below, was a polar chain of atoms where one sub-lattice (red, in Fig. 3.2) has been displaced by a distance d . This displacement causes an asymmetry in the interatomic interaction potentials which is denoted by Δ . The two atom unit cell has length L and a relaxed bond length of $\frac{L}{2}$. The on site energies of the s-orbitals are taken as $+\epsilon$ and $-\epsilon$ respectively. Note that the Berry phase that we calculate here corresponds to the electronic polarisation only, not the total polarisation.

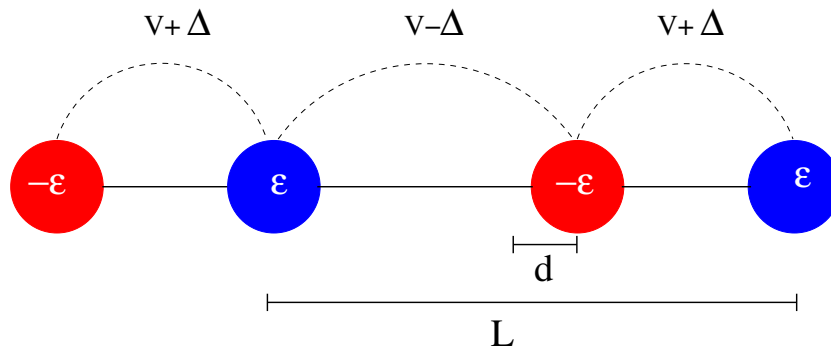


FIGURE 3.2: Linear chain of atoms with asymmetric interactions ($V \pm \Delta$), on-site energies ϵ (blue) and $-\epsilon$ (red), with the red sub-lattice displaced by a distance d relative to the blue sub-lattice.

The Hamiltonian for the above system for Bloch states with wave number \mathbf{k} is given by;

$$H_{\mathbf{k}} = \begin{pmatrix} \epsilon & 2e^{i\mathbf{k}d}[V \cos(\frac{\mathbf{k}L}{2}) - i\Delta \sin(\frac{\mathbf{k}L}{2})] \\ 2e^{-i\mathbf{k}d}[V \cos(\frac{\mathbf{k}L}{2}) + i\Delta \sin(\frac{\mathbf{k}L}{2})] & -\epsilon \end{pmatrix} \quad (3.1)$$

with the lower eigenvalue given by

$$E(k) = -\sqrt{\epsilon^2 + 4V^2 \cos^2\left(\frac{\mathbf{k}L}{2}\right) + 4\Delta^2 \sin^2\left(\frac{\mathbf{k}L}{2}\right)} \quad (3.2)$$

From Eq. 3.1 we also have that;

$$(\epsilon - E)\alpha + 2e^{i\mathbf{k}d} \left[V \cos\left(\frac{\mathbf{k}L}{2}\right) - i\Delta \sin\left(\frac{\mathbf{k}L}{2}\right) \right] \beta = 0 \quad (3.3)$$

so that,

$$\beta = \frac{(E - \epsilon)\alpha}{2[V^2 \cos^2(\frac{\mathbf{k}L}{2}) + \Delta^2 \sin^2(\frac{\mathbf{k}L}{2})]} e^{-i\mathbf{k}d} \left[V \cos\left(\frac{\mathbf{k}L}{2}\right) + i\Delta \sin\left(\frac{\mathbf{k}L}{2}\right) \right] \quad (3.4)$$

where α and β are the amplitude of the eigenstate ψ on the blue ($+\epsilon$) and red ($-\epsilon$) sites respectively. We wish to compute the matrix element $\langle \psi(\mathbf{k}) | \psi(\mathbf{k} + d\mathbf{k}) \rangle$ and then use the calculated product to evaluate the phase ϕ . This can be done using the normalisation of ψ and the above equation to get expressions for α and β but it is much simpler if we set the amplitude on one of the basis states to be purely real. Now if we fix α to be purely real then β must have the same phase as

$$e^{-i\mathbf{k}d} \left[V \cos\left(\frac{\mathbf{k}L}{2}\right) + i\Delta \sin\left(\frac{\mathbf{k}L}{2}\right) \right] \quad (3.5)$$

We can now define ψ as

$$\psi(\mathbf{k}) = \begin{pmatrix} \alpha(\mathbf{k}) \\ [\beta_0(\mathbf{k}) + i\gamma] e^{-i\mathbf{k}d} \end{pmatrix} \quad (3.6)$$

and if we expand $\psi(\mathbf{k} + d\mathbf{k})$, to linear order, we get

$$\psi(\mathbf{k} + d\mathbf{k}) = \begin{pmatrix} \alpha(\mathbf{k}) + \frac{d\alpha_0}{d\mathbf{k}} d\mathbf{k} \\ \beta_0 e^{-i\mathbf{k}d} + \frac{d}{d\mathbf{k}} (\beta_0 e^{-i\mathbf{k}d}) d\mathbf{k} + i(\gamma e^{-i\mathbf{k}d}) + \frac{d}{d\mathbf{k}} (\gamma e^{-i\mathbf{k}d}) d\mathbf{k} \end{pmatrix} \quad (3.7)$$

We can now use this to compute $\langle \psi(\mathbf{k}) | \psi(\mathbf{k} + d\mathbf{k}) \rangle$;

$$\begin{aligned} \langle \psi(\mathbf{k}) | \psi(\mathbf{k} + d\mathbf{k}) \rangle = & \alpha^2 + \alpha \frac{d\alpha_0}{d\mathbf{k}} d\mathbf{k} \\ & + \beta_0^2 + \beta_0 \frac{d\beta_0}{d\mathbf{k}} d\mathbf{k} - id\beta_0^2 d\mathbf{k} \\ & + i\gamma\beta_0 + i\beta_0 \frac{d\gamma}{d\mathbf{k}} d\mathbf{k} + d\gamma\beta_0 d\mathbf{k} \\ & - i\gamma\beta_0 - i\gamma \frac{d\beta_0}{d\mathbf{k}} d\mathbf{k} - d\gamma\beta_0 d\mathbf{k} + \gamma^2 \\ & + \gamma \frac{d\gamma}{d\mathbf{k}} d\mathbf{k} - id\gamma^2 d\mathbf{k} \end{aligned} \quad (3.8)$$

From requiring ψ to be normalised we have $\alpha_0^2 + \beta_0^2 + \gamma^2 = 1$. Some terms also cancel to give us

$$\begin{aligned} \langle \psi(\mathbf{k}) | \psi(\mathbf{k} + d\mathbf{k}) \rangle = & 1 + \alpha \frac{d\alpha_0}{d\mathbf{k}} d\mathbf{k} + \beta_0 \frac{d\beta_0}{d\mathbf{k}} d\mathbf{k} - id\beta_0^2 d\mathbf{k} + i\beta_0 \frac{d\gamma}{d\mathbf{k}} d\mathbf{k} - i\gamma \frac{d\beta_0}{d\mathbf{k}} d\mathbf{k} - id\gamma^2 d\mathbf{k} \\ \approx_e & \alpha \frac{d\alpha_0}{d\mathbf{k}} d\mathbf{k} + \beta_0 \frac{d\beta_0}{d\mathbf{k}} d\mathbf{k} - id\beta_0^2 d\mathbf{k} + i\beta_0 \frac{d\gamma}{d\mathbf{k}} d\mathbf{k} - i\gamma \frac{d\beta_0}{d\mathbf{k}} d\mathbf{k} - id\gamma^2 d\mathbf{k} \end{aligned} \quad (3.9)$$

Which, when the product of \mathbf{k} -values is computed from one end of the Brillouin zone to the other, gives us

$$\prod_{j=0}^{j=J-1} \langle \psi(\mathbf{k}) | \psi(\mathbf{k} + d\mathbf{k}) \rangle = e^{\int_{-\frac{\pi}{L}}^{\frac{\pi}{L}} \left[\alpha \frac{d\alpha_0}{d\mathbf{k}} + \beta_0 \frac{d\beta_0}{d\mathbf{k}} - id\beta_0^2 + i\beta_0 \frac{d\gamma}{d\mathbf{k}} - i\gamma \frac{d\beta_0}{d\mathbf{k}} - id\gamma^2 \right] d\mathbf{k}} \quad (3.11)$$

Both α_0 and β_0 are even in \mathbf{k} so the first two terms, being odd in \mathbf{k} , drop out of the integral. Then, when the imaginary part of the log of this product is taken, we get an expression for the Berry phase as

$$\Phi = \text{Im} \ln \prod_{j=0}^{j=J-1} \langle \psi(\mathbf{k}) | \psi(\mathbf{k} + d\mathbf{k}) \rangle \quad (3.12)$$

$$= \int_{-\frac{\pi}{L}}^{\frac{\pi}{L}} \left(\beta_0 \frac{d\gamma}{d\mathbf{k}} - \gamma \frac{d\beta_0}{d\mathbf{k}} - d\beta_0^2 - d\gamma^2 \right) d\mathbf{k}. \quad (3.13)$$

To assist in solving Eq. 3.13, we note that $|\beta^2|$ can be defined as $\frac{1-\alpha_p(\mathbf{k})}{2}$, where

$$\alpha_p(\mathbf{k}) = \frac{\epsilon}{\sqrt{\epsilon^2 + 4[V^2 \cos^2(\frac{\mathbf{k}L}{2}) + \Delta^2 \sin^2(\frac{\mathbf{k}L}{2})]}}. \quad (3.14)$$

Using this expression for the modulus and getting the phase from Eq. 3.5, we can write β_0 and γ as

$$\begin{aligned} \beta_0 &= g(\mathbf{k})V \cos\left(\frac{\mathbf{k}L}{2}\right) \\ \gamma &= g(\mathbf{k})\Delta \sin\left(\frac{\mathbf{k}L}{2}\right) \end{aligned} \quad (3.15)$$

where

$$g(\mathbf{k}) = \sqrt{\frac{1 - \alpha_p(\mathbf{k})}{2[V^2 \cos^2(\frac{\mathbf{k}L}{2}) + \Delta^2 \sin^2(\frac{\mathbf{k}L}{2})]}} \quad (3.16)$$

Using these expressions for γ and β_0 the integral for the Berry phase gives

$$\phi = \int_{-\frac{\pi}{L}}^{\frac{\pi}{L}} g(\mathbf{k})^2 \left[\frac{V\Delta L}{2} - dV^2 \cos^2\left(\frac{\mathbf{k}L}{2}\right) - d\Delta^2 \sin^2\left(\frac{\mathbf{k}L}{2}\right) \right] d\mathbf{k} \quad (3.17)$$

which simplifies to

$$\phi = \int_{-\frac{\pi}{L}}^{\frac{\pi}{L}} \frac{1 - \alpha_p(\mathbf{k})}{[V^2 \cos^2(\frac{\mathbf{k}L}{2}) + \Delta^2 \sin^2(\frac{\mathbf{k}L}{2})]} \frac{V\Delta L}{4} - \frac{d(1 - \alpha_p(\mathbf{k}))}{2} d\mathbf{k} \quad (3.18)$$

or

$$\phi = \int_{-\frac{\pi}{L}}^{\frac{\pi}{L}} g(\mathbf{k})^2 \frac{V\Delta L}{2} - \frac{d(1 - \alpha_p(\mathbf{k}))}{2} d\mathbf{k} \quad (3.19)$$

The above integral has two competing terms which we shall call ‘spontaneous’ and ‘strain-induced’, respectively. Both of these terms have both covalent and polar contributions. These can be separated out as follows;

$$\phi = \int_{-\frac{\pi}{L}}^{\frac{\pi}{L}} \underbrace{\frac{\Delta L}{4V} \frac{1}{\cos^2\left(\frac{\mathbf{k}L}{2}\right) + \frac{\Delta^2}{V^2} \sin^2\left(\frac{\mathbf{k}L}{2}\right)}}_{\text{covalent}} d\mathbf{k} \quad (3.20)$$

$$\begin{aligned} & - \underbrace{\frac{\Delta L}{4V} \frac{\alpha_p(\mathbf{k})}{\left(\cos^2\left(\frac{\mathbf{k}L}{2}\right) + \frac{\Delta^2}{V^2} \sin^2\left(\frac{\mathbf{k}L}{2}\right)\right)}}_{\text{polar}} \\ & + \underbrace{\frac{-d}{2}}_{\text{covalent}} + \underbrace{\frac{d\alpha_p(\mathbf{k})}{2}}_{\text{polar}} dk \end{aligned} \quad (3.21)$$

where the first two terms are the ‘spontaneous’ ones and the last two are the ‘strain-induced’ terms. The ‘strain-induced’ terms are linear in d , due to our expansion of ψ to only linear order, and are responsible for the piezoelectric response in the crystal. We make the following approximation for $\alpha_p(k)$, which should be appropriate for small Δ ($\Delta \ll \epsilon$).

$$\begin{aligned} \alpha_p(\mathbf{k}) &= \frac{\epsilon}{\sqrt{\epsilon^2 + 4V^2 \cos^2\left(\frac{\mathbf{k}L}{2}\right)}} \\ &= \frac{\epsilon}{\sqrt{\epsilon^2 + 4V^2 - 4V^2 \sin^2\left(\frac{\mathbf{k}L}{2}\right)}} \\ &= \frac{\epsilon}{\sqrt{\epsilon^2 + 4V^2}} \frac{1}{\sqrt{1 - \frac{4V^2}{\epsilon^2 + 4V^2} \sin^2\left(\frac{\mathbf{k}L}{2}\right)}} \\ &= \frac{\alpha_p}{\sqrt{1 - \alpha_c^2 \sin^2\left(\frac{\mathbf{k}L}{2}\right)}} \end{aligned} \quad (3.22)$$

where α_p and α_c are defined as the bond polarity and covalence, respectively, and also $\alpha_p^2 + \alpha_c^2 = 1$. Our expression for ϕ now has the form

$$\begin{aligned} \phi &= \int_{-\frac{\pi}{L}}^{\frac{\pi}{L}} \underbrace{\frac{-d}{2}}_A + \underbrace{\frac{d\alpha_p}{2\sqrt{1 - \alpha_c^2 \sin^2\left(\frac{\mathbf{k}L}{2}\right)}}}_B + \underbrace{\frac{\Delta L}{4V} \frac{1}{\cos^2\left(\frac{\mathbf{k}L}{2}\right) + \frac{\Delta^2}{V^2} \sin^2\left(\frac{\mathbf{k}L}{2}\right)}}_C \\ & - \underbrace{\frac{\Delta L}{4V} \frac{\alpha_p}{\sqrt{1 - \alpha_c^2 \sin^2\left(\frac{\mathbf{k}L}{2}\right)} \left(\cos^2\left(\frac{\mathbf{k}L}{2}\right) + \frac{\Delta^2}{V^2} \sin^2\left(\frac{\mathbf{k}L}{2}\right)\right)}}_D d\mathbf{k} \end{aligned} \quad (3.23)$$

All four integrals now have analytic solutions. The first one, term A, is trivial. Integrals B and D are complete elliptic integrals of the first and third kinds, respectively. Complete elliptic integrals, however, are evaluated in terms of power series expansions and hence do not offer any further simplification. At this stage we solve Eq. 3.23 numerically. In Fig. 3.3 we show how the Berry phase, as calculated via the integral in Eq. 3.23 for small, finite Δ and $d = 0$, varies with ϵ/V . It can clearly be seen that for small ϵ the Berry phase varies linearly with ϵ and eventually, for large enough ϵ non-linear terms have a strong effect.

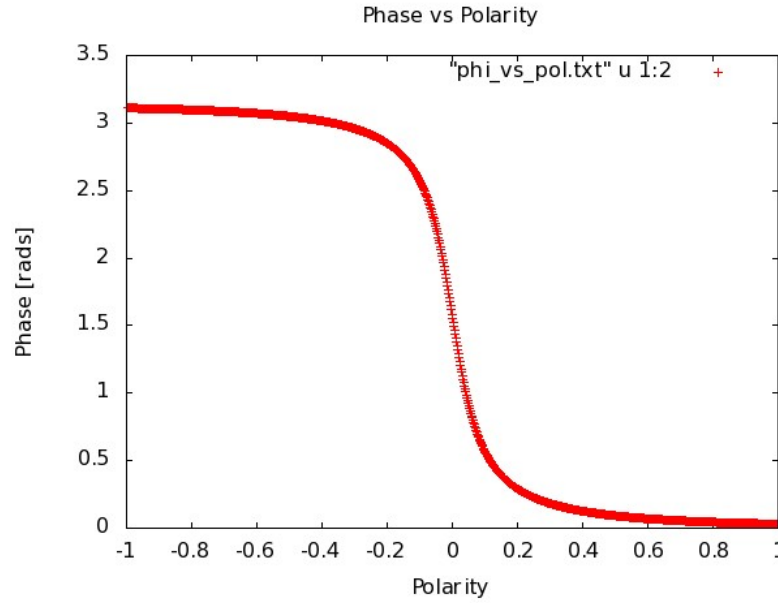


FIGURE 3.3: How Eq. 3.23 varies as a function of ϵ/V for finite Δ and $d = 0$.

The strain dependence of the Berry phase ϕ is described by a term, linear in d in both integrals A and B of Eq. 3.23. In the case of a homopolar compound, where $\alpha_p = 0$, the phase is exactly linear with strain giving an electronic contribution to the polarisation of $-ed/2L$. The ionic component, defined as the dipole moment per unit volume is also linear in d and so the two contributions, $\pm ed/2L$, cancel out giving no piezoelectric response for homopolar compounds, as expected. We see as α_p grows so does the linear strain dependence in polar materials through the contribution from integral B. As previously mentioned, ϕ increases linearly and rapidly for small values of ϵ/V but above values of ± 0.1 converges to π or zero. Thus, as this term is scaled by d in integral B, even for small strain in polar materials we see a strong piezoelectric response. Fig. 3.4 shows how the integral C in Eq. 3.23 varies with Δ . This is equivalent to the case where both $d = 0$ and $\epsilon = 0$. The dependence of ϕ on Δ is interesting in that it jumps, almost

discontinuously, to $\pm\pi/2$ for any non-zero value. This might relate to spontaneous polarisation being due to the breaking of symmetry but considering we dropped Δ from integral B in the approximation of Eq. 3.22 and also the fact that Δ and ϵ , as we have defined them, are not independent in reality, we are reluctant to draw any strong conclusions from this.

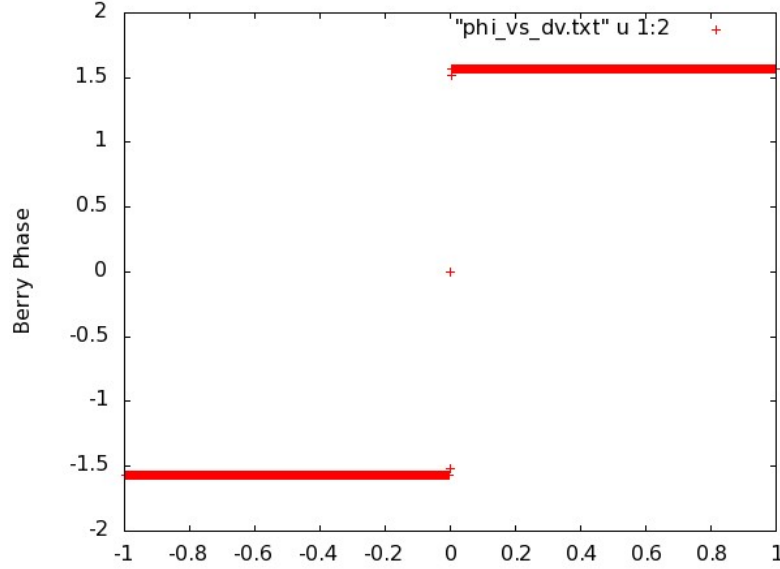


FIGURE 3.4: How Eq. 3.23 varies as a function of Δ for $d = 0$ and $\epsilon = 0$.

In summary, we note the dependence of the Berry phase on the polarity of the material, even in the absence of strain. We show why there is no piezoelectric response for homopolar compounds as well as demonstrate how polar materials have a strong piezoelectric response.

3.3 Numerical Implementation

3.3.1 Grids and Strings

In order to implement the numerical definition of the Berry phase polarisation Eq. 2.57 a discrete 3-dimensional grid must first be set up over the entire Brillouin zone. This grid has two components, first a set of uniformly distributed points, \mathbf{k}_\perp , are selected in a plane perpendicular to the direction in which the electronic polarisation is being calculated. Then, at each of these points, strings of parallel \mathbf{k}_j points are created that run from one end of the Brillouin zone to the other (from

$\mathbf{k}_0 = -\pi/\mathbf{a}$ to $\mathbf{k}_{J-1} = \pi/\mathbf{a}$, where \mathbf{a} is a lattice vector parallel to the direction of polarisation). The density of points in the entire grid is then determined by the number of points in the plane and the number of points per string. This will be shown later to be an important factor in determining the accuracy of the results. The phase change of the eigenvector $u_{n\mathbf{k}}$ along each string is then calculated by taking the overlap of the eigenvector at the first point in a string with the next point on the string and then taking the product of this element at all subsequent \mathbf{k}_j points in the string:

$$\phi_{n\mathbf{k}_\perp} = \text{Im} \ln \prod_{j=0}^{J-1} \langle u_{n,\mathbf{k}_\perp,\mathbf{k}_j} | u_{n,\mathbf{k}_\perp,\mathbf{k}_{j+1}} \rangle. \quad (3.24)$$

The number of points needed to converge to the contribution from each string was checked and it was found that $J = 100$ points was sufficient for our calculations. One careful consideration must be taken to maintain the periodic boundary conditions of the cell; the eigenvector at the final point in the string, which is a full reciprocal lattice vector \mathbf{G}_i from the first, should be replaced by the eigenvector at the first point that is phase shifted by the full lattice vector:

$$\langle u_{n,\mathbf{k}_\perp,\mathbf{k}_J} | = e^{i\mathbf{G}_i \cdot \mathbf{r}} \langle u_{n,\mathbf{k}_\perp,\mathbf{k}_0} |. \quad (3.25)$$

Once the phase of each string is obtained the total phase per band is calculated by summing over all strings. The Berry phase theory of polarisation is limited to describing the behaviour of insulating crystal materials for the simple reason that partially filled bands do not behave adiabatically. This does not affect the applicability of this theory to III-V materials, since we are looking at semiconductors in their ground state. The total phase of the crystal is then given by summing over all occupied states.

$$\Phi_{tot} = \sum_n \sum_{\mathbf{k}_\perp} \phi_{n\mathbf{k}_\perp} \quad (3.26)$$

The reader may have noticed that this is not consistent with Eq. 2.57. This is because the above formulation of the Berry phase requires the bands to be non-degenerate at all \mathbf{k} points. In order to deal with band crossings and degenerate bands a different approach is needed. Instead of summing over individual bands one must calculate the determinant of the overlap matrix \mathcal{S} ;

$$\mathcal{S}_{mn}(\mathbf{k}_j, \mathbf{k}_{j+1}) = \langle u_{m,\mathbf{k}_\perp,\mathbf{k}_j} | u_{n,\mathbf{k}_\perp,\mathbf{k}_{j+1}} \rangle. \quad (3.27)$$

To clarify, this is still done at each \mathbf{k} point along a string and the strings are still summed over. Thus the electric polarisation is calculated as

$$P_{e_i} = -\frac{fe(\Delta\mathbf{k})^2}{(2\pi)^3} \sum_{\mathbf{k}_\perp} \text{Im} \ln \prod_{j=0}^{J-1} \det \langle u_{m,\mathbf{k}_\perp,\mathbf{k}_j} | u_{n,\mathbf{k}_\perp,\mathbf{k}_{j+1}} \rangle \quad (3.28)$$

3.3.2 Choice of Unit Cells

When constructing the mesh of strings for this calculation we mentioned that they run from one end of the Brillouin zone to the other and that one must impose the periodicity of the unit cell by phase shifting the first element to replace the last. This task becomes complex when dealing with a Brillouin zone that is not prismatic. Take for example the zinc blende (ZB) structure, one that plays an important role in our calculations. The simplest unit cell that describes this face centred cubic (fcc) structure is a two atom unit cell; one atom at the origin and another at $(\mathbf{a}/4, \mathbf{a}/4, \mathbf{a}/4)$ where \mathbf{a} is the lattice constant and has the following lattice vectors:

$$(\mathbf{a}/2, \mathbf{a}/2, 0) \quad (3.29)$$

$$(\mathbf{a}/2, 0, \mathbf{a}/2) \quad (3.30)$$

$$(0, \mathbf{a}/2, \mathbf{a}/2). \quad (3.31)$$

None of these lattice vectors are orthogonal; they give a Brillouin zone that has the shape of a truncated octahedron. Then when trying to calculate the Berry phase of this structure the length of the strings varies across the Brillouin zone and hence so also do the reciprocal lattice vectors, \mathbf{G}_i . The calculation is greatly simplified if one employs a unit cell where at least one of the lattice vectors is orthogonal to the other two. This gives a prismatic Brillouin zone where the strings are all of equal length. Of course, one requires that the Brillouin be prismatic along the direction that the polarisation is being calculated.

For this reason, our first implementation of the Berry phase theory of polarisation with a TB Hamiltonian was using an 8 atom ZB unit cell that had both a cubic unit cell and Brillouin zone.

3.3.3 The Need for a Reference Structure

In section 2.3.3 we briefly stated that the Berry phase theory of polarisation can only be used to calculate polarisation differences. This is due to the closed path requirement of the formalism. We can again use the periodicity of the structure to simplify the calculation. Consider a crystal structure that is subjected to an adiabatic change that does not return to its initial state, for example a sublattice displacement in a ZB structure, and this change is denoted by λ where $\lambda = 0$ is the initial state and $\lambda = 1$ is the final state. We can construct a closed loop in the 2-dimensional phase space of λ and \mathbf{k} , as shown in Fig.3.5. The Berry phase and

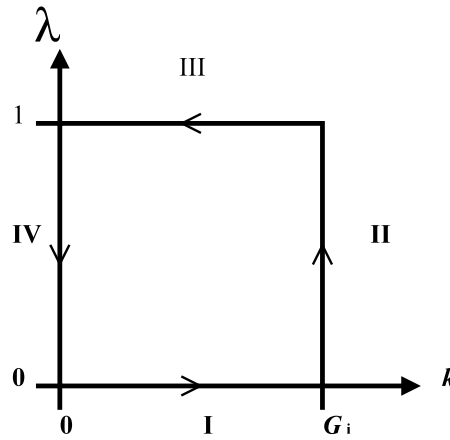


FIGURE 3.5: The closed loop in a λ - \mathbf{k} phase space along which the Berry phase is evaluated.

hence the polarisation is obtained by evaluating the following contour integral for each of the four sides of this path:

$$\Phi = -i \oint_C \langle u_{n,\mathbf{k}}^{(\lambda)} | \nabla_{\mathbf{k}} u_{n,\mathbf{k}}^{(\lambda)} \rangle. \quad (3.32)$$

Since $\mathbf{k} = 0$ and $\mathbf{k} = \mathbf{G}_i$ are equivalent \mathbf{k} points sections II and IV of the line integral are equal and opposite and do not need to be calculated. This means that the form of the adiabatic change no longer concerns us, only the end points. Thus we can use the ZB crystal structure as a reference to compare wurtzite structures against; we do not need to map the adiabatic transition between the two crystallographic phases - we just concern ourselves with the end points. What remains to be done is to calculate the contribution from sections I and III. These are the previously described integrals over \mathbf{k} space at the initial and final values of λ .

Zinc blende is important for our calculations not only as a reference structure for comparison but also as an implementation test. It is shown from group theory arguments that ZB has no spontaneous polarisation (P_{spont}) due to its symmetry [28]. This was the first validation test for our codes; to show that ZB has no spontaneous polarisation using Eq. 3.28. Using the aforementioned cubic 8 atom unit cell the value for the P_{spont} obtained was of the order of 10^{-15}Cm^{-2} which is effectively zero. This showed us that, so far, the results of our model were consistent with what should be expected. We then started using this as a reference structure against which to compare wurtzite. However, when we used [111] oriented ZB cells, which has an equivalent orientation to that of the wurtzite 4 atom cell, the P_{spont} of these ZB cells was no longer zero. The initial values obtained were of the order of 10^{-4}Cm^{-2} which is still small but cannot be explained by differences in the input parameters or the computational process. This, we believed, was due to our implementation of the model. This could not be ignored as it was the cornerstone of our comparisons. Work which we describe in the next section showed that this was a convergence issue - the graph of $\sum_n \phi_{n\mathbf{k}_\perp}$ has a very sharp peak near to $\mathbf{k}_\perp = 0$: a very fine integration mesh is required in order for Φ_{tot} to approach zero, although a coarser grid is sufficient to calculate *changes* in Φ_{tot} due to the introduction of atomic displacements in the unit cell.

3.4 Phase surfaces and Convergence

3.4.1 Homopolar Test

One test for the full calculations that was derived from the linear chain model was to calculate P_{spont} for a homopolar material. In the linear chain model this is equivalent to setting the bond polarity α_p to zero. In the absence of macroscopic strain ($d = 0$) for this case, the linear chain then has a vanishing Berry phase. As a test for our calculations, we set the on-site energies in the TB Hamiltonian equal for anions and cations and also set $V_{p_a s_c \sigma} = V_{p_c s_a \sigma}$. This is analogous to a homopolar material such as silicon, germanium or diamond. As predicted by the linear chain model, P_{spont} with this set up is almost exactly zero for any unit cell regardless of the orientation. At this point, again to gain insight into the model, the phase associated with each string over the grid of strings that spans the base of the Brillouin zone was plotted.

3.4.2 Phase surfaces

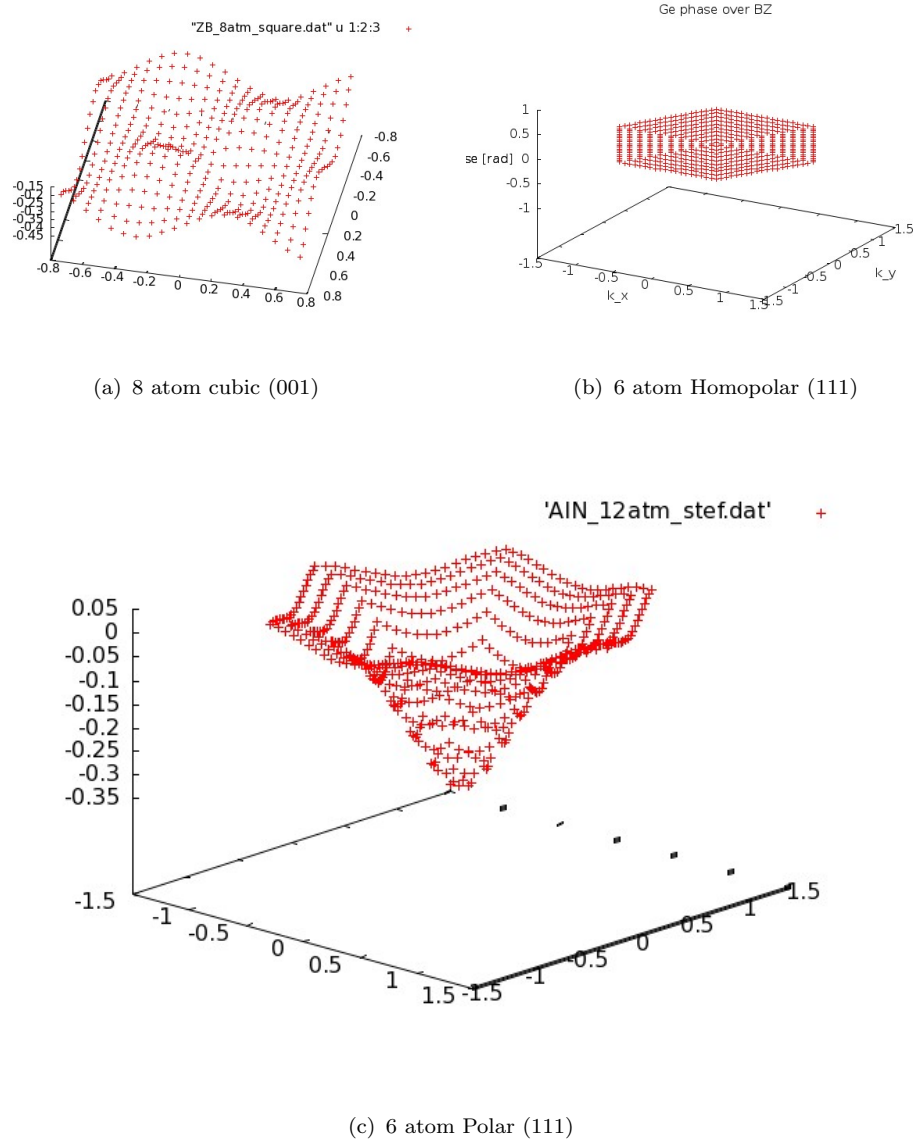


FIGURE 3.6: The phase surfaces of three different unit cells.

Fig. 3.6 shows the calculated variation in the value of the phase of each individual string across the Brillouin zone for three of the different structures considered. Integrating over these surfaces then gives the total phase for one of the line integrals in Fig. 3.5. To reiterate, the difference between this and another similar calculation of the system after an adiabatic change then gives the Berry phase. The unit cells represented in Fig. 3.6 all have a ZB structure which means the integral over each of these surfaces should be zero. The integrals of the first two surfaces, Fig. 3.6(a) (an 8 atom [001] oriented GaAs cell) and Fig. 3.6(b) (a homopolar [111] oriented cell) are identically zero. This is clear from a symmetry analysis in the case of

Fig. 3.6(a). Here the values of the strings are distributed in a pattern similar to a square lattice of sinusoidal waves that is symmetric about the $z = 0$ plane and hence cancel almost exactly. In Fig. 3.6(b), for a homopolar structure, each of the individual strings has zero phase and hence so also does their sum. The final surface (calculated from a 6 atom, [111] oriented, GaAs cell) gives a total phase of the order of 10^{-4} . We attribute this calculated value to the shape of the surface. While this ‘phase surface’ does have a sixfold rotational symmetry, we cannot apply a simple symmetry analysis as in Fig. 3.6(a) to deduce that the overall value of the integral must be zero. The sampling of \mathbf{k} points is crucial here. Notice that as you go towards the centre of this phase surface its curvature changes rapidly and hence the accuracy of our mid-point rule method of numerical integration decreases. (We use a uniform grid of \mathbf{k} strings, each centred in a small area element \mathbf{k}_Δ , so hence we use the mid-point method to calculate the integral.) To investigate whether this was the source of error in these calculations either a higher density mesh or a more sophisticated one was needed.

3.4.3 Convergence of the number of strings

Before we discuss the convergence of the phase due to the number of strings used in the calculation we must first comment on some general properties of the mesh. The calculations that were showing errors are the ones using [111] oriented ZB unit cells (and also 4 atom wurtzite cells). The Brillouin zone of these unit cells takes the shape of a hexagonal prism, so the mesh of strings for these unit cells is also hexagonal, as shown in Fig. 3.7.

These hexagonal grids have a C_{6v} symmetry (they are invariant under rotations of 60°) as do the phase surfaces we integrate over, e.g. Fig. 3.6(c). This allowed us to restrict our calculations to one 60° wedge of the Brillouin zone. We further increased the speed of our calculations by noticing that each of these wedges (in the phase surface) has an axial symmetry about the line bisecting it. Hence we needed only to calculate 1/12th of the phase surface and once proper care is given to the boundary points we easily extended this to the full surface. In Table 3.1 we show the effect of increasing the number of strings used in the calculations. The first column m is the number of points into which the line in the Brillouin zone from Γ to K is discretised. M then denotes the total number of points in the aforementioned irreducible wedge of the Brillouin zone; this is a triangular number

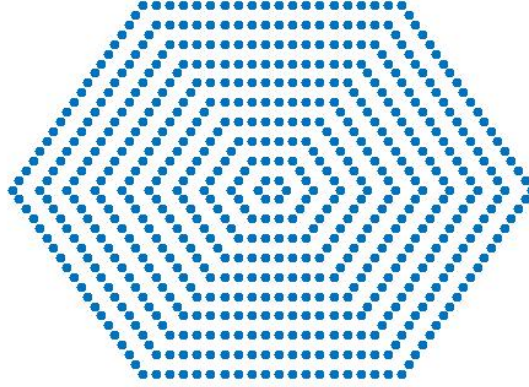


FIGURE 3.7: An example of the hexagonal mesh of strings used for [111] oriented zincblende and wurtzite unit cells. This grid contains 660 strings.

of m ($M = m(m+1)/2$). The third column is the sum over all strings- note this is not the total Berry phase. To obtain the Berry phase this number must be divided by the number of strings. The final column is the calculated electronic polarisation along the [111] direction.

m	M	$\sum_{\mathbf{k}_\perp} \phi_{\mathbf{k}_\perp}$	$P_e \text{ } Cm^{-2}$
75	2850	-8.1844×10^{-3}	-1.8030×10^{-6}
120	7260	-8.1606×10^{-3}	-7.0223×10^{-7}
200	20100	-8.1230×10^{-3}	-2.5164×10^{-7}

TABLE 3.1: Convergence data for ZB 6 atom, [111] oriented unit cell.

Notice in column three the sum of the phase of all the strings stays almost constant, independent of the number of strings (M) used. The fact that this number is not identically zero is due to a limitation of the model used, which will be discussed later. We can see here though, that as the number of strings increases the calculated polarisation goes to zero. It converges slowly to zero at a rate of $1/M$. Shown in Table 3.2 is the same data for a WZ 4 atom unit cell. Here we see how the sum of the phase of each string (column 3) grows linearly with the number of strings (column 2) and hence the polarisation converges to a non-zero value.

It must be noted here that this density of points is far above that required for calculating values to be compared with experiment. The last row in Table 3.2

m	M	$\sum_{\mathbf{k}_\perp} \phi_{\mathbf{k}_\perp}$	$P_e \text{ } Cm^{-2}$
20	210	0.0199	6.0594×10^{-5}
50	1275	0.0965	4.6948×10^{-5}
80	3240	0.2388	4.5369×10^{-5}
120	7260	0.5305	4.4807×10^{-5}
160	12880	0.9391	4.4611×10^{-5}
200	20100	1.4643	4.4520×10^{-5}
280	39340	2.8649	4.5280×10^{-5}

TABLE 3.2: Convergence data for 4-atom GaN WZ unit cell.

($m = 280$) corresponds to 1.8×10^9 points in the Brillouin zone (39340 strings per one 12th wedge with 4000 points per string). Previous studies used a Monkhorst-Pack mesh of $16 \times 16 \times 10$, which we revert back to for the remainder of this study. As mentioned, the motivation for doing this was to show that with our TB model the P_{spn} of ZB was still zero and to show that the P_{spn} of ideal WZ, although small, was non-zero.

3.5 Zinc blende and ideal wurtzite comparison

As we have shown in the previous section P_{spn} of a ZB structure is zero. It might be expected in a first nearest neighbour TB model that the P_{spn} of ideal WZ could also be zero. The tetrahedral, first NN environment in both structures is identical and hence with a NN Hamiltonian the lack of inversion symmetry in ideal WZ may not have a major influence. Hence we postulated that the non-zero P_{spn} for ideal WZ that had previously been calculated in other works [29, 30] would appear in our results when second and third NN interactions were introduced in our Hamiltonian. As seen in Table 3.2, the P_{spn} of GaN with a first NN Hamiltonian was found to be $4.5280 \times 10^{-5} Cm^{-2}$, which is very small but not zero. The small difference between this and ZB can be seen in Fig. 3.8, where line scans through the phase surface of the two materials are shown. The lines scans run through the high symmetry points of the Brillouin zone (from M to Γ through K and back to M and K again), and the small difference between the two structures can be seen in the section between M and K . This region lies at the fringe of the Brillouin zone.

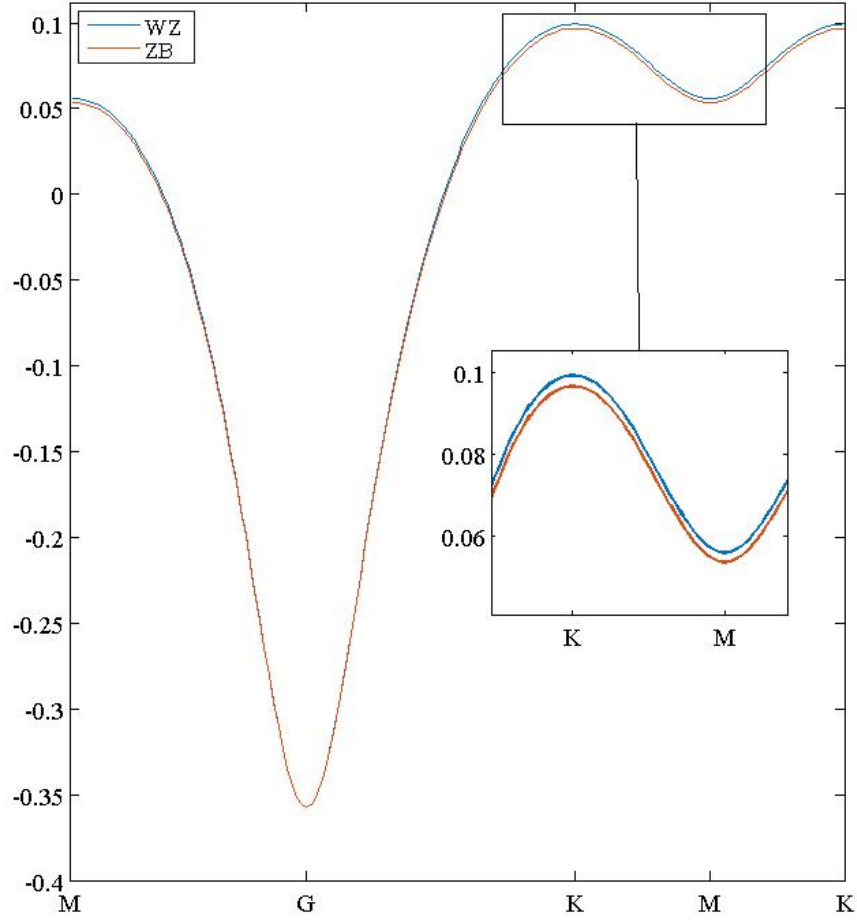


FIGURE 3.8: A line scan through the phase surface of ZB GaN and ideal WZ GaN.

This shows that with a first NN Hamiltonian, ZB and ideal WZ are almost equivalent in terms of P_{spn} . We now introduce second and selected third NN interactions.

3.5.1 Third Nearest Neighbors

WZ, and also ZB, has 12 second NN atoms. They can be separated into two sets of six, a co-planar set in the same xy plane as the atom at the origin and another set of six comprised of two groups of three directly above and below the atom at the origin, in the direction of the c axis. These two groups of six were both found to give a small contribution to the P_{spn} but the contributions were equal and opposite and cancel each other out. This is consistent with the first NN

results, since second NN interactions are smaller than first NN ones, and since ZB has a similar but not identical second NN environment. Consequently, we omitted second NN interactions for this reason, and also because to accurately include them one has to fit a much bigger set of TB parameters.

Any atom in a WZ lattice has 25 third NN. These are arranged in four layers in the c plane and each layer has C_{3v} symmetry (alternate layers form either a triangle or a hexagon centred about the atom at the origin). The position of these layers along the c -axis is not symmetric. The dominant contribution to this asymmetry is from one specific third NN, shown in Fig. 3.9. Here two p_z states are oriented directly towards each other and are separated by $5/3$ of an unstrained bond length, in the ideal WZ structure. As a result the two orbitals have a relatively large overlap and hence introduce a definite asymmetry into the interactions in the WZ crystal structure

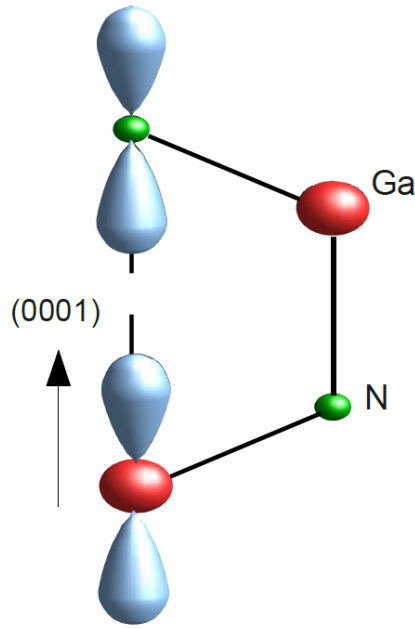


FIGURE 3.9: The specific third NN interaction investigated.

We included in our TB Hamiltonian a matrix element coupling p_z orbitals of third NNs directly aligned with each other along the c -axis. This interaction was initially modelled by scaling the pp_σ parameter by the ratio of the bond lengths squared $\left(\frac{d}{d_0}\right)^2$ (where d is the third NN distance and d_0 is the unstrained bond length) following Harrison. While this gave values for P_{spn} that were comparable to previous DFT calculations [29, 30], the crystal field splitting of the valence bands is strongly overestimated. Fitting this third NN interaction to correctly

model the crystal field splitting then gives a negligible contribution to P_{spn} . As a result we conclude that c -axis third NN interactions can contribute to P_{spn} but that it would be difficult to devise a unique parameter set to consistently describe P_{spn} and the crystal field splitting.

3.5.2 Effective charges

As a next step to modelling material response, we next used our model to calculate the Born or transverse effective charges for ZB and ideal WZ materials. This also offered the opportunity to test our implementation of the model with previously published results employing the same methods. The effective charge is a tensor that represents the change in polarisation in direction i due to a sub-lattice shift in direction j ,

$$(e_T^*)_{ij} = \Omega \frac{\partial \mathbf{P}_i^{\text{Tot}}}{\partial \mathbf{d}_j} \quad (3.33)$$

where Ω is the unit cell volume and \mathbf{d} is the sublattice shift. An important point to note here is that \mathbf{P}^{Tot} is the total polarisation, with both ionic and electronic contributions. The electronic part is, of course, calculated using our TB and Berry phase model. The ionic part is simple to calculate, given by the total dipole moment per unit volume;

$$\mathbf{P}_i^{\text{ion}} = \frac{1}{\Omega} \sum_n Z_n \mathbf{r}_{n,i}. \quad (3.34)$$

The sum n runs over the number of atoms in the unit cell n . Z_n denotes the nominal atomic charge (in our case 3 or 5) and again i is the direction of polarisation. While this is a simple calculation, care must be taken that the quantum of polarisation is removed before the ionic part is added to the electronic. Remember bulk polarisation, both ionic and electronic, is defined modulo eR_i/Ω and hence is a multi-valued vector quantity. Both the electronic and ionic polarisation take on a lattice of values, each separated by this modulus. Hence we must be careful both when combining electronic and ionic components as well as comparing initial and final polarisation states, that the values we take are all in the same ‘branch’ of this lattice. We always work with the first branch, since the electronic component is typically an order of magnitude smaller than the modulus of polarisation and

hence no correction is required and there is no ambiguity as to which branch the ‘proper’ polarisation value lies in.

Another important consideration is the choice of origin. The same origin must obviously be chosen for both the ionic and electronic calculations. Shifting the origin is equivalent to a change of gauge which introduces a phase shift in the eigenvectors and hence in our polarisation calculations. As long as this phase shift is consistent, by using the same origin, throughout our calculation it will cancel out in the difference between initial and final states.

With these issues given due consideration, we were first able to compare our implementation of the model with that of Ref. [27] by calculating ZB effective charges.

Compound	Expt.	Ref. [27]	Our calc.
GaAs	2.16	1.49	1.48
GaSb	2.15	1.10	1.10
InP	2.55	2.16	2.16
AlSb	1.93	1.17	1.10

TABLE 3.3: Comparison of e_T^* calculations, using the same parameters sets, with each other and with experiment.

Table 3.3 shows our attempt to replicate the results of Ref. [27] for the effective charges of four ZB compounds. The sp^3s^* TB parameters (both the interaction parameters and the bond length scaling exponents), used in this calculation were given in Ref. [31]. This was the only set of results published where the full parameter set was available. Our results match those of Ref. [27] very closely for GaAs, GaSb and InP. The small differences can be attributed to the use of a slightly different mesh. We suspect the difference in AlSb comes from a misprint in the parameters in Ref. [31]. When compared to experimental results, however, a consistent underestimation of e_T^* can be seen in table 3.3. This trend had already been previously reported [25]. This may be due to the fact that the minimal basis used in the TB model cannot accurately describe the full Brillouin zone and instead the parameters are fitted to the band structure at high symmetry points, such as Γ , X and L in ZB. Hence with a TB model there are areas of the Brillouin zone that have flat bands. The Berry phase calculation, which needs to sample the entire Brillouin zone, then includes these areas of flat bands which do not contribute to the phase. This leads to an underestimation of the electronic component of the polarisation and hence the effective charge. The main focus of Ref. [27] was that

these calculations are very sensitive to small changes in the parameters and this underestimation could be improved using a set of bond length scaling exponents that are material and bond type dependent.

Table 3.4 shows the comparison between ideal WZ and ZB structures in terms of effective charges. As a result of the similar first NN environment of the two structures they have an almost equivalent response to sub-lattice displacements. These calculations were carried out using WZ parameters derived by Stefan Schulz by fitting the TB band structures to Heyd-Scuseria-Ernzerhof (HSE) screened exchange hybrid functional density functional theory (DFT) band structures [30, 32]. The same interaction parameters and on-site energies are used for the ZB calculations so that the similarity of the structures would not be masked by possible differences in the fitting procedure.¹ It must be acknowledged however that the NN TB Hamiltonian has longer range effects folded in, and because of the different environment at 2NN and beyond WZ may not fit ZB perfectly and vice versa. The results again confirm the similarity of the two structures within our first NN TB model.

Compound	ZB	Ideal WZ
GaN	2.42	2.43
InN	2.72	2.71
AlN	2.84	2.84

TABLE 3.4: Comparing e_T^* calculations of ZB and ideal WZ

3.5.3 Piezoelectric Coefficients

We next turn our attention to calculating the piezoelectric (PZ) coefficients for ZB and ideal WZ structures. Piezoelectricity is the name given to the phenomenon of strain-induced polarisation [33]. It is described, in tensor notation, usually, by two sets of coefficients e_{ijk} (to first order) and B_{ijklm} (to second order).

$$P_{pz,i} = \sum_{jk} e_{ijk} \epsilon_{jk} + \frac{1}{2} \sum_{jklm} B_{ijklm} \epsilon_{jk} \epsilon_{lm} + \dots \quad (3.35)$$

We first consider just the linear regime e_{ijk} . In matrix or Voigt notation the linear response is given by

¹A number of different TB parameter sets can give the same, or very similar, band structures.

$$\begin{pmatrix} P_{pz,x} \\ P_{pz,y} \\ P_{pz,z} \end{pmatrix} = \begin{pmatrix} e_{11} & e_{12} & e_{13} & e_{14} & e_{15} & e_{16} \\ e_{21} & e_{22} & e_{23} & e_{24} & e_{25} & e_{26} \\ e_{31} & e_{32} & e_{33} & e_{34} & e_{35} & e_{36} \end{pmatrix} \begin{pmatrix} \epsilon_{11} \\ \epsilon_{22} \\ \epsilon_{33} \\ 2\epsilon_{23} \\ 2\epsilon_{13} \\ 2\epsilon_{12} \end{pmatrix} \quad (3.36)$$

where ϵ_{jk} are the components of the strain tensor. The PZ tensor in (001) oriented ZB has, due to its symmetry, only three nonzero coefficients and they are all equal $e_{14} = e_{25} = e_{36}$. When the strain and PZ tensors are then rotated to the (111) direction the polarisation vector \mathbf{P}_{pz} takes the form [34]

$$\mathbf{P}_{pz}^{(111)} = \begin{pmatrix} 2e'_{15}\epsilon'_{13} \\ 2e'_{15}\epsilon'_{23} \\ e'_{31}(\epsilon'_{11} + \epsilon'_{22}) + e'_{33}\epsilon'_{33} \end{pmatrix} + \begin{pmatrix} e'_{11}(\epsilon'_{11} - \epsilon'_{22}) \\ 2e'_{12}\epsilon'_{12} \\ 0 \end{pmatrix}, \quad (3.37)$$

with $e'_{11} = -\sqrt{\frac{2}{3}}e_{14}$, $e'_{12} = \sqrt{\frac{2}{3}}e_{14}$, $e'_{15} = e'_{31} = -\frac{1}{\sqrt{3}}e_{14}$ and $e'_{33} = \frac{2}{\sqrt{3}}e_{14}$, so that $\frac{e'_{33}}{e'_{31}} = -2$. This is a ratio that is used extensively later in the chapter when studying real WZ since the ratio deviates from -2 as the structure deviates from the ideal WZ case. The first term in Eq. 3.37 has the same form as the WZ PZ vector

$$\mathbf{P}_{pz}^{WZ} = \begin{pmatrix} 2e_{15}\epsilon_{13} \\ 2e_{15}\epsilon_{23} \\ e_{31}(\epsilon_{11} + \epsilon_{22}) + e_{33}\epsilon_{33} \end{pmatrix}. \quad (3.38)$$

The macroscopic strain, given by the strain tensor ϵ_{jk} , also leads to internal displacements within the cell. These internal displacements depend on the direction of the strain with respect to the orientation of the crystal. When using (111) oriented ZB cells this internal displacement is given by;

$$\mathbf{t}_{int}^{(111)} = \frac{\zeta a_{zb}}{4\sqrt{3}} (\epsilon_{11} + \epsilon_{22} - 2\epsilon_{33}) \begin{pmatrix} 0 \\ 0 \\ 1 \end{pmatrix}, \quad (3.39)$$

where ζ is the *Kleinmann internal displacement parameter* and a_{zb} is the ZB lattice constant. This results in an internal relaxation of the z coordinates of either the cation or anion sub-lattice with strain. For WZ there are three internal displacement vectors required and five parameters [35].

$$\mathbf{t}_1^{WZ} = c_0 \left[\zeta_1 \epsilon_{13} + \zeta_5 \epsilon_{12}, \zeta_1 \epsilon_{yz} + \zeta_5 \frac{(\epsilon_{11} - \epsilon_{22})}{2}, \zeta_2 (\epsilon_{11} + \epsilon_{22}) - \zeta_3 \epsilon_{33} \right], \quad (3.40)$$

$$\mathbf{t}_2^{WZ} = a_0 \left[-\zeta_4 \epsilon_{12}, -\zeta_4 \frac{(\epsilon_{11} - \epsilon_{22})}{2}, 0 \right], \quad (3.41)$$

$$\mathbf{t}_3^{WZ} = \mathbf{t}_1^{WZ} + \mathbf{t}_2^{WZ} - 2c_0 \left[\zeta_5 \epsilon_{12}, \zeta_5 \frac{(\epsilon_{11} - \epsilon_{22})}{2}, 0 \right] \quad (3.42)$$

In this case a_0 and c_0 are the lattice constants of the 4-atom WZ unit cell. The internal displacement parameters ζ_i are determined again from HSE screened exchange hybrid DFT calculations [35]. If \mathbf{r}_0 , \mathbf{r}_1 , \mathbf{r}_2 and \mathbf{r}_3 are the atomic position vectors in a 4 atom unit cell, then the internal displacements are implemented as follows;

$$\mathbf{r}'_0 = \mathbf{r}_0 \mathbf{r}'_1 = (\mathbb{1} + \epsilon) \mathbf{r}_1 + \mathbf{t}_1^{WZ} \quad (3.43)$$

$$\mathbf{r}'_2 = (\mathbb{1} + \epsilon) \mathbf{r}_2 + \mathbf{t}_2^{WZ} \quad (3.44)$$

$$\mathbf{r}'_3 = (\mathbb{1} + \epsilon) \mathbf{r}_3 + \mathbf{t}_3^{WZ}. \quad (3.45)$$

This treatment is then extended to the 12 atom unit cells used in our calculations. We first restrict our attention to the PZ coefficients e_{31} and e_{33} since the macroscopic strains associated with them can be described maintaining the C_{3v} symmetry of the Brillouin zone. The coefficient e_{15} is related to shear strain which breaks this symmetry and hence requires a larger and an adaptive mesh of strings. In table 3.5 below the electronic contribution to the polarisation induced by biaxial P_{el}^{31} and uniaxial P_{el}^{33} strain for ZB and ideal WZ structures is shown. Both structures are again modelled using 12 atom unit cells and equivalent internal displacements are applied. Similar to table 3.4 for the effective charges, the only full set of TB parameters available for all the III-nitrides were those derived by Dr. Schulz. These parameters were also used in the ZB structures so that we could directly compare the different structures. The internal displacement parameters used were also derived for WZ structures (by Dr. Miguel Caro [35]) but were again applied to both structures.

Compound	ZB	P_{el}^{31}	P_{ion}	ZB	P_{el}^{33}	P_{ion}
		WZ			WZ	
GaN	-0.0150	-0.0164	0.0150	0.0285	0.0273	-0.0288
InN	-0.0172	-0.0194	0.0158	0.0358	0.0339	-0.0322
AlN	-0.0190	-0.0192	0.0164	0.0441	0.0440	-0.0365

TABLE 3.5: Comparing the electronic component of polarisation induced by biaxial $\epsilon_{11} = \epsilon_{22}$ and uniaxial ϵ_{33} strain for ZB and ideal WZ structures.

The PZ response, in terms of the electronic contribution, are very similar for ZB and ideal first NN WZ. This follows the same trend as the effective charges and P_{spon} for these structures. Unlike the effective charges, where there is a large difference between the electronic and ionic contributions, for the PZ calculations the electronic and ionic component are very similar in magnitude. They are obviously of opposite sign and are also large compared to the total polarisation, generally a factor of 10 bigger. Thus, the relatively small error in the electronic component of the polarisation as seen in this and previous works [25, 27] leads to a large distortion of the PZ coefficients calculated. This can clearly be seen in table 3.6, which shows the total PZ coefficients, e_{31} and e_{33} , for ZB and ideal WZ calculated using the same parameters as table 3.5. The reason for the ratio of $\frac{e_{33}}{e_{31}}$ not being exactly equal to -2 for ZB structure is that the internal displacement parameters that were used are derived for WZ structures.

Compound	ZB		WZ	
	e_{31}	e_{33}	e_{31}	e_{33}
GaN	-3.203×10^{-4}	-0.0251	-0.13	-0.14
InN	-0.14	0.36	-0.36	0.017
AlN	-0.26	0.76	-0.28	0.75

TABLE 3.6: Comparison of the total coefficients, e_{31} and e_{33} , for ZB and ideal WZ structures.

In table 3.7 we compare our TB results to recent HSE DFT calculations of the ZB coefficient e_{14} , done within our group by Miguel Caro [36]. Since we use different internal displacement parameters we cannot directly compare the electronic and ionic components of the coefficients but instead we compared their ratio $\frac{-e_{14}^{el}}{e_{14}^{ion}}$.

Compound	TB	DFT
	$\frac{-e_{14}^{el}}{e_{14}^{ion}}$	$\frac{-e_{14}^{el}}{e_{14}^{ion}}$
GaN	1.00	1.16
InN	1.09	1.25
AlN	1.16	1.24

TABLE 3.7: Comparing the ratio of $\frac{-e_{14}^{el}}{e_{14}^{ion}}$ as calculated by our TB model and using HSE DFT [36]

We see a general underestimation of the ratio $\frac{-e_{14}^{el}}{e_{14}^{ion}}$ calculated by our TB model when compared to the DFT results. This shows that the model gives a good qualitative description of the piezoelectric response for ZB and ideal WZ but as the total coefficients show, accurate quantitative results are not attainable with this model.

3.6 Real Wurtzite

We now finally turn our attention to real WZ structures. The difference between ideal and real WZ, as mentioned previously, is the c/a ratio, and the internal displacements of atoms along the c -axis, characterised by the parameter u . These internal displacements cause a change in bond angles and bond lengths so that they are no longer all equal. This asymmetry leads to a nonzero P_{spon} along the c -axis. Shown in Fig. 3.10 is how the phase surface of ZB and ideal WZ changes as a result of these internal displacements.

3.6.1 Spontaneous Polarisation

Shown in table A.3 is the P_{spon} calculated for the real WZ GaN, InN and AlN structures. The calculations were carried out with the on-site energies and interaction parameters again from Ref.[30, 32] but two different sets of scaling exponents, $d^{Harr.}$ where all the exponents are set to 2 [8] and a set, derived by Andy Lindsay [37], $d^{A.L.}$ where each individual exponent is fitted to match key band structure deformation potentials. Our results, when compared with Ref. [29], show an underestimation of 50-60% for Harrison's scaling exponents. However for GaN and

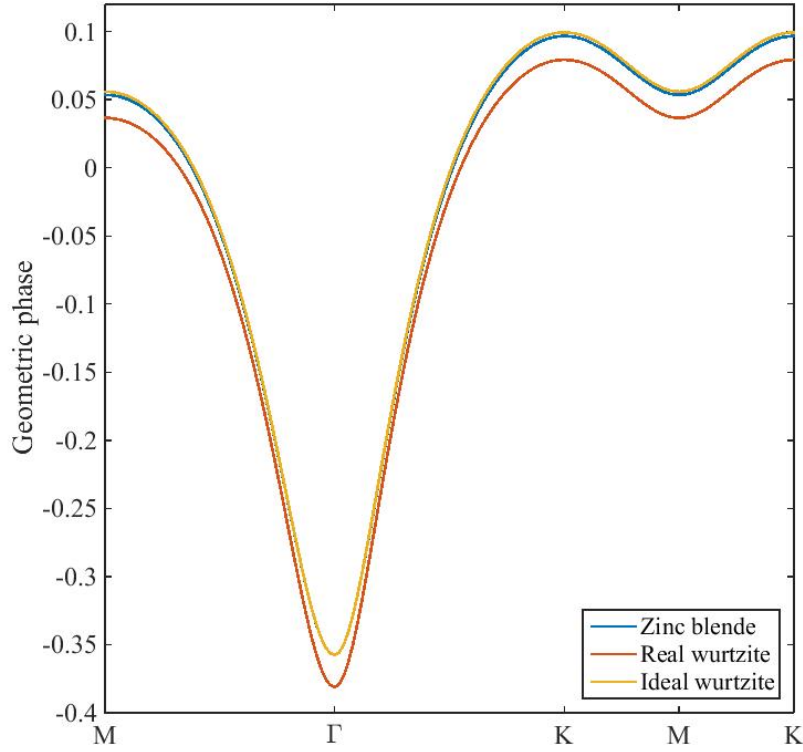


FIGURE 3.10: Line scans through the phase surface of ZB (blue), ideal WZ (orange) and real WZ (red).

InN, the set derived by Andy Lindsay give good results and show an improvement for AlN.

$P_{\text{spn}} (Cm^{-2})$	GaN	InN	AlN
$d^{A.L.}$	-0.026	-0.034	-0.066
d^{Harr}	-0.014	-0.019	-0.048
Ref. [29]	-0.029	-0.032	-0.081

TABLE 3.8: Comparison of P_{spn} calculated using different scaling parameters. The first row are calculated using the scaling parameter derived by Andy Lindsay, the second row show results using Harrison's scaling law and the last row are DFT calculations from Ref. [29].

To reiterate, the general underestimation in these results is due, we believe, to the minimal basis in the TB model. This basis, which gives the TB model its most useful features i.e. that it is fast and atomistic, cannot fit the band structure throughout the entire Brillouin zone. In the process of fitting the parameters

to describe the eigenvalues at certain high symmetry points, other areas of the Brillouin zone have to be neglected. Also, it is the change in the phase of the eigenvectors that is measured in the Berry phase model but this is not directly tested in the band structure fitting. There are a large number of parametrizations of the Hamiltonian that give a similar band structure in the TB model and in general an infinite number of basis sets that have the same projection. It is the aspect of the TB model that makes it attractive for band structure calculations that leads to its inability, in conjunction with the Berry phase model, to produce accurate quantitative results for electronic polarisation. However, as can be seen from the results presented thus far, the model does produce the correct qualitative trends; e.g. the correct sign and ratio of PZ coefficients. We also see from table A.3 that the limitations of the TB model to describe the full Brillouin zone can be overcome by using larger scaling exponents, as was seen in Ref. [27]. This, as is shown in the next section, only works however for individual strain states and the exponents have to be adjusted to fit different types of applied strain.

3.6.2 Piezoelectric Coefficients

Shown in table 3.9 are the PZ coefficients calculated for real WZ III-nitrides using $d^{Harr.}$ and $d^{A.L.}$ scaling exponents, compared with the results of HSE DFT calculations [30] that also used the Berry phase method as implemented in the VASP software package [38].

As mentioned in the previous section, the scaling exponents $d^{A.L.}$ that gave improved results for P_{spn} do not improve the results for the PZ coefficients. The small values and error in sign seen for $d^{A.L.}$ in table 3.9 are, again, due to the fact that the total polarisation is due to the cancellation of the ionic and electronic terms which are large and comparable in magnitude. In addition to this, for real WZ polarisation differences the reference structure or initial state also has an ionic and electronic component due to the internal displacements². For ZB and ideal WZ the reference structure (ZB) was centrosymmetric and hence had a zero total polarisation and zero error associated with the reference state, the error came from

²A note on implementation. Since both initial and final states have an ionic component, both ionic components must be corrected so that they are in the same branch of the polarisation vector. However since the final state is strained from the initial one the volume has changed and hence the quantum of polarisation ($e\mathbf{R}/\Omega$) has also changed. Therefore, for both states the ionic polarisation must be corrected but often by different quanta of polarisation.

P_{spn}	GaN	InN	AlN
$d^{A.L.}$			
e_{31}	0.412	0.105	0.247
e_{33}	-0.884	-0.031	0.032
$d^{Harr.}$			
e_{31}	7.81×10^{-4}	-0.128	-0.211
e_{33}	-0.053	0.316	0.681
HSE DFT			
e_{31}	-0.44	-0.58	-0.63
e_{33}	0.74	1.07	1.46

TABLE 3.9: Comparison of e_{31} and e_{33} for different bond length scaling parameters with values calculated from HSE DFT using VASP.

the final state. In real wurtzite there is a cancellation of ionic and electronic terms in both the initial and final state. Since the PZ coefficients are calculated as finite differences of these two states with respect to strain this can then add to the error in the calculated PZ coefficients in the case of real WZ. Based on the analysis presented here, we conclude that accurate quantitative piezoelectric coefficients are not attainable using the TB model. The model can reproduce trends effectively. Fig. 3.11 shows the calculated variation of the ionic and electronic component of the polarisation in AlN as a function of axial strain ϵ_{33} . It can be seen from the symmetry that the majority of both components cancel out. The small difference that determines the coefficient is then highly sensitive to small changes in the electronic polarisation such as those due to parametrization. It is for this reason that we do not attempt to calculate e_{15} or second order terms.

While this model is unable to extract accurate coefficients, it can still show qualitative trends. The ratio of $\frac{e_{33}}{e_{31}}$ is close to -2 for ZB and ideal WZ. In real WZ we have determined the ionic component of this ratio analytically for very small strain as;

$$\frac{e_{33}}{e_{31}} = \frac{-\zeta_3}{\zeta_2 + (u_{id} - u)}, \quad (3.46)$$

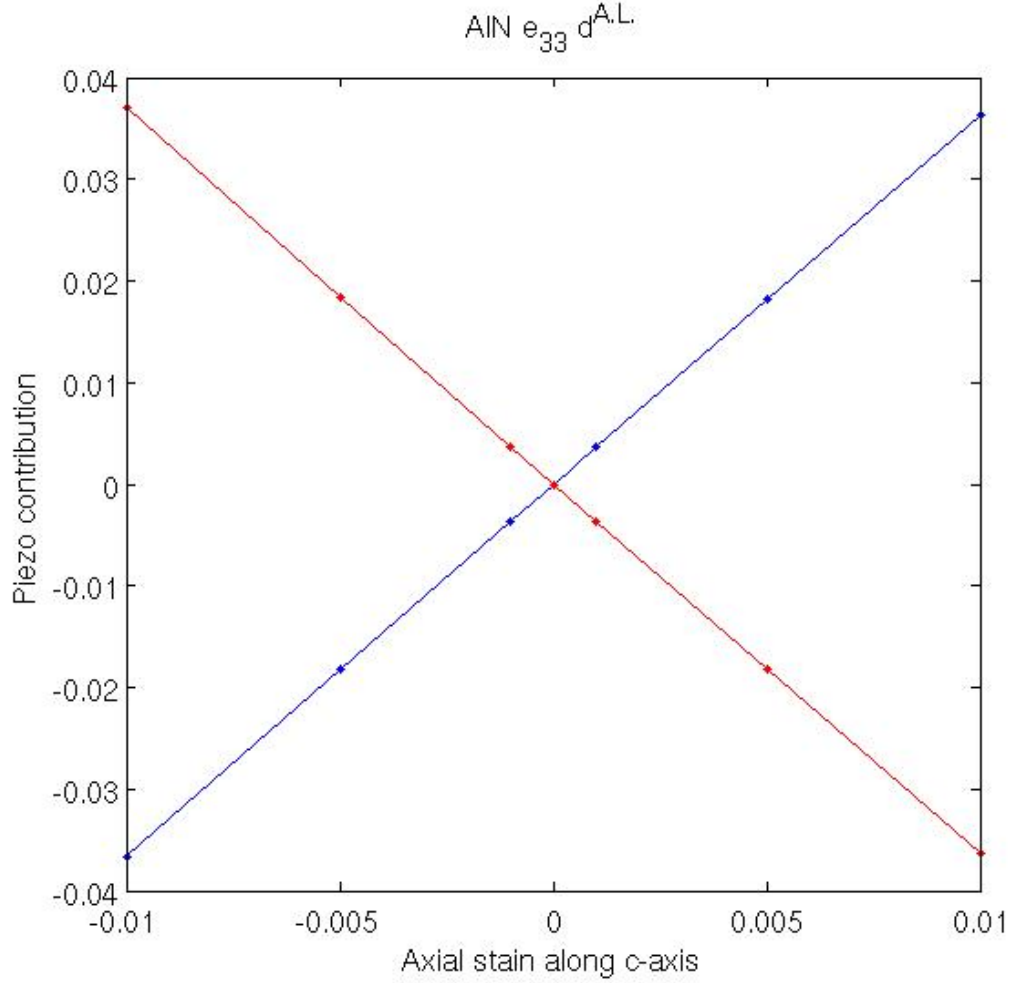


FIGURE 3.11: How the ionic (blue) and electronic (red) components of the polarisation cancel in the calculation of e_{33} .

where ζ_i are internal displacement parameters, u is the internal displacement parameter for real WZ and $u_{id} = \frac{3}{8}$. For ideal WZ and ZB $u = u_{id}$ and this ratio is dominated by the ratio of $\frac{\zeta_3}{\zeta_2}$ which is close to 2. In the III-nitrides non-ideality increases as one goes from GaN to InN to AlN, i.e. u increases from 0.375, the c/a ratio decreases from $\sqrt{8/3}$ and the ratio of $\frac{\zeta_3}{\zeta_2}$ deviates from 2. As this non-ideality increases in the structure the ratio of $\frac{e_{33}}{e_{31}}$ deviates from -2, as shown in table 3.10.

Similar to table 3.5, we can take the electronic part of the polarisation induced by the strains associated with e_{33} and e_{31} to examine the electronic part of this ratio. The error in the electronic component of the polarisation cancels out in this ratio and, in table 3.11, we see the same deviation from -2 as non-ideality increases. This shows that the Berry phase and TB model gives a good qualitative description of

	ζ_2	ζ_3	$\frac{\zeta_3}{\zeta_2}$	u	$\frac{c}{a}$	$\left(\frac{e_{33}}{e_{31}}\right)_{ionic}$
GaN	0.083	0.159	1.916	0.3772	1.626	-1.988
InN	0.107	0.218	2.037	0.3796	1.612	-2.151
AlN	0.086	0.191	2.221	0.3818	1.602	-2.437

TABLE 3.10: Deviation of the ionic part of the ratio of $\frac{e_{33}}{e_{31}}$ from -2 as non-ideality increases.

the electronic polarisation properties of III-nitride semiconductors but, as we have seen, quantitative analysis is beyond the scope of this model.

Compound	$\left(\frac{e_{33}}{e_{31}}\right)_{el}^{A.L.}$	$\left(\frac{e_{33}}{e_{31}}\right)_{el}^{d^{-2}}$
GaN	-1.942	-1.961
InN	-2.309	-2.179
AlN	-2.987	-2.530

TABLE 3.11: Deviation of the electronic part of the ratio of $\frac{e_{33}}{e_{31}}$ from -2 as non-ideality increases.

3.7 Conclusions

In this chapter we have presented a numerical and analytic analysis of the polarisation properties of III-nitride materials using the TB model in conjunction with the Berry phase theory of polarisation. With a linear chain model we show how the Berry phase varies linearly with small values of bond polarity and strain. In the numerical calculations we first compare ZB and ideal WZ structures within a first NN Hamiltonian. We show how both structures have a similar polarisation response to strain and sub-lattice displacements. Effective charges for ZB are close to ideal WZ values. The values for the electronic component of the ZB PZ coefficient e_{14} match closely the corresponding ideal WZ coefficients. We demonstrate how the values of the total polarisation, ionic and electronic, are only qualitatively described by this model. We show how this is due to two factors, an uncertainty in the electronic polarisation which is then amplified by the small magnitude of the total polarisation relative to the electronic and ionic components which cancel

to give the small total. We compare our results for both the total and just the electronic polarisation with DFT results to illustrate this. We explain how the uncertainty in the electronic component arises at least in part from a fundamental limitation of the tight-binding model; the minimal basis employed in the TB model cannot span the entire Brillouin zone and, in the Berry phase theory of polarisation, the entire Brillouin zone is sampled. We also examine the effect on P_{spn} in ideal WZ of including interactions from selected third NN atoms and show that while it effects both the P_{spn} and the crystal field splitting, these interactions cannot easily and consistently model the both the crystal field splittin and P_{spn} .

For real WZ material we show the parameter sensitivity of the model when calculating P_{spn} . We show how the bond length scaling exponents have a strong effect on the electronic component, as previously shown, and that for large exponents, that were fitted to match key deformation potentials, the results can be improved. We further show that these larger scaling exponents do not produce the correct trends for PZ coefficients, we suggest this is because they do not improve the description of the eigenstates but compenstate by amplifying other terms. We finally demonstate that also for real WZ, although the model gives a reasonable description of the electronic polarisation, accurate quantative results that depend on the total polarisation are beyond the scope of this model. We show that our model produces correct qualitative trends for the electronic part of the ratio of the PZ coefficients $\frac{\epsilon_{33}}{\epsilon_{31}}$ but reiterate that an accurate description of total polarisation values are beyond the scope of this model.

Chapter 4

Band gap bowing and optical polarisation switching in $\text{Al}_{1-x}\text{Ga}_x\text{N}$ alloys

4.1 Introduction

Nitride semiconductors InN, GaN, AlN and their respective alloys are highly attractive for a variety of different applications. Amongst other applications nitride-based systems are of interest for detectors, light-emitting diodes, and lasers operating in the UV range with applications such as power electronics, optical storage, medical diagnostics and treatment, and sterilization processes [1, 2]. More specifically the wurtzite alloy $\text{Al}_{1-x}\text{Ga}_x\text{N}$ is of particular interest for efficient emission in the UV spectral range [39]. When designing optoelectronic devices based on $\text{Al}_{1-x}\text{Ga}_x\text{N}$ systems the evolution of the band gap with composition x is of central importance. Usually the band gap evolution with composition x is described by a Végard's law type expression:

$$E_g^{\text{AlGa}\text{N}} = xE_g^{\text{Ga}\text{N}} + (1-x)E_g^{\text{Al}\text{N}} - bx(1-x) , \quad (4.1)$$

where b denotes the so-called band gap bowing parameter. Values for b reported in the literature vary from 0.7 eV to 1.3 eV [40–47]. Recently, it has been shown that random alloy fluctuations significantly affect the electronic and optical properties of InGa N and AlIn N alloys [30, 32, 42, 48–50]. This raises the question if random

alloy fluctuations also affect significantly the composition dependence of the band gap and band edge states in AlGa_N alloys. Previous theoretical results seem to indicate that these effects are less pronounced in AlGa_N systems compared for example to AlInN [40]. However, these studies are mainly performed on small supercells (16 atoms), which might overlook wave function localization effects.

In addition to the band gap value, the light polarisation characteristics of wurtzite AlGa_N-based heterostructures have a strong influence on the light extraction efficiency of AlGa_N-based devices [51–53]. It has been reported that the light output efficiency of *c*-plane based AlGa_N LED devices decreases as Al content increases [1]. This is in part due to the valence band ordering of wurtzite AlN [54] which in Al-rich AlGa_N gives rise to transverse magnetic (TM) optical emission, where the emitted light is polarised along the wurtzite *c*-axis direction. This ordering, as we discuss in detail here, switches for lower Al content in AlGa_N to give transverse electric (TE) emission (polarised in the *c*-plane) which in turn allows greater light extraction efficiency for surface-emitting LED structures. Higher Al content is desirable for UV emission but, above a certain Al composition the emission switches from TE to TM polarisation. Knowledge of the composition at which this switching occurs is crucial to device design. As highlighted in Ref. [32] alloy fluctuations lead to a surprisingly early switching of the valence band ordering in AlInN (between 15-18% InN content). This switching arises from wave function localization effects due to random alloy fluctuations. Therefore, even if alloy fluctuations are less important for the energy gap, the question remains how the wave function character of the topmost valence band is affected by random alloy fluctuations.

To capture effects arising from random alloy fluctuations, both large super-cells and an atomistic description of these super-cells are required for a proper analysis. Here we apply previously established atomistic tight-binding (TB) [32] and local polarisation [30] models to study the electronic structure of random wurtzite AlGa_N alloys.

Our analysis of the composition dependence of the energy gap in AlGa_N alloys gives a band gap bowing parameter of $b = 0.94$ eV. This value is in good agreement with recent experimental and theoretical data [40, 45–47]. In addition, we find that the band gap bowing mainly originates from the bowing of the conduction band (CB) edge, while the valence band (VB) edge shows a close to linear

composition dependence. Moreover, our study shows that the optical polarisation switching from TM to TE emission occurs in the range of a GaN content of $x \approx 0.75$. Although the VB edge energy shows a close to linear variation with GaN content, the optical polarisation switching nevertheless occurs at a significantly higher Al composition (25%) than would be expected ($\sim 10\%$) based on strict linear interpolation.

The chapter is organized as follows. In Sec. 4.2 we introduce the theoretical framework we use to study band gap bowing and optical polarisation switching in AlGaN systems. Our theoretical results are presented in Sec. 4.3. The composition dependence of the band gap in random AlGaN alloys over the full composition range is discussed in Sec. 4.3.1, while Sec. 4.3.2 focuses on the CB and VB edge behaviour with composition. Section. 4.3.3 deals with optical polarisation switching in AlGaN alloys. Finally we summarize our results in Sec. 4.4.

4.2 Method

To achieve a microscopic description of the effect of random alloy fluctuations on the composition dependence of the band gap in AlGaN systems, we employ a semi-empirical sp^3 TB model. The model includes local strain and built-in field fluctuations arising from random alloy fluctuations. The theoretical framework can be divided into several steps. Firstly, we construct super-cells with approximately 12,000 atoms in which the Al and Ga atoms are randomly distributed on the Group III sites. For homopolar tetrahedrally bonded compounds, commonly available force fields are based on the valence force field model (VFF) [55] or the Keating potential [56]. A generalisation of the two models to include electrostatic interactions explicitly was given by Martin for ZB heteropolar compounds. In Martin's model the total energy of atom i in a ZB unit cell is given by

$$\begin{aligned}
 U_i = & \frac{1}{2} \sum_{j \neq i} \frac{1}{2} k_r (r_{ij} - r_{ij}^0)^2 + \sum_{j \neq i} \sum_{k \neq i, k > j} \frac{1}{2} k_\theta^i r_{ij}^0 r_{ik}^0 (\theta_{ijk} - \theta_{ijk}^0)^2 \\
 & + k_{r\theta}^i [r_{ij}^0 (r_{ij} - r_{ij}^0) + r_{ik}^0 (r_{ik} - r_{ik}^0)] (\theta_{ijk} - \theta_{ijk}^0) + k_{rr}^i (r_{ij} - r_{ij}^0)(r_{ik} - r_{ik}^0) \\
 & + \sum_{j \neq i} \left[\frac{Z_i^* Z_j^* e^2}{4\pi\epsilon_0\epsilon_r r_{ij}} - \frac{1}{2} \sum_{j \neq i} \frac{1}{4} \alpha_M \frac{Z_i^* Z_j^* e^2}{4\pi\epsilon_0\epsilon_r r_{ij}^0{}^2} (r_{ij} - r_{ij}^0) \right].
 \end{aligned} \tag{4.2}$$

The different k_r , k_θ^i , $k_{r\theta}^i$ and k_{rr}^i denote the force constants. The angles between atoms i , j and k are given by θ_{ijk} , Z_i^* denotes the effective charge and e is the elementary charge. The permittivity of the vacuum is given by ϵ_0 while the dielectric constant of the material is denoted as ϵ_r . The Madelung constant is given by α_M , which in the case of ZB has the value $\alpha_M = 1.6381$. The last term in Eq. 4.2 is a linear repulsion term, required to keep the crystal stable [57]. It cancels out linear contributions from the power series expansion of the electrostatic part of the energy. Both summation indices, j and k , run over the first NN of atom i except in the second last sum (marked with a prime symbol) which runs over the whole crystal as it corresponds to the long-ranged Coulomb interaction. The factors of a $1/2$ are simply to prevent double counting over the atoms in the same unit cell. Martin has also given the relation between the force constants of the general VFF in Eq. 4.2 and Keating's potential. The main advantage of using Eq. 4.2 for WZ structures is that inclusion of electrostatic terms leads to the important qualitative result of a c/a ratio and internal parameter u that deviate from the ideal values ($\sqrt{8/3}$ and $3/8$ respectively). Fitting of the different force constants and the effective charges to the structural and elastic properties of the WZ materials (work that was carried out by Miguel Caro) leads to a good quantitative description of these quantities. The VFF model has been implemented using the software package **gulp** [58].

The local strain can then be determined from the relaxed atomic positions, following Ref. [59]. From the local strain the local polarisation is calculated. Here the i^{th} component of the polarisation vector field is evaluated at each atomic site according to [30]:

$$P_i = \underbrace{\sum_{j=1}^6 e_{ij}^{(0)} \epsilon_j}_{\text{macroscopic}} + \underbrace{P_i^{sp} - \frac{e}{V_0} \frac{Z_i^0}{N_{\text{coor}}^0} \left[\mu_i - \sum_{j=1}^3 (\delta_{ij} + \epsilon_{ij}) \mu_{i,0} \right]}_{\text{microscopic}}. \quad (4.3)$$

This separates the contributions to the polarisation due to macroscopic effects, given by the macroscopic strain ϵ_j (Voigt notation), the clamped-ion piezoelectric coefficient $e_{ij}^{(0)}$, and local effects, including the spontaneous polarisation P_i^{sp} and also a contribution dependent on the bond asymmetry parameter μ_i . The quantity μ_i is related to the internal strain parameters. Z_i^0 , V_0 and N_{coor}^0 represent, respectively, Born effective charge, unit cell volume and number of nearest neighbours at the given atomic site, and e is the fundamental electronic charge.

Having established the local polarisation field, we use a point dipole model to calculate the corresponding built-in potential. This approach presents a solution to the problem of solving Poisson's equation on an irregular atomistic grid. More details are given in Ref. [30].

This atomistic description of strain, polarisation and built-in potential has to be coupled to an atomistic electronic structure theory. Here we choose the TB method to achieve such a description. The required TB parameters at each atomic site are set to the bulk value for the specific atom. To account for the band offset between GaN and AlN, the on-site energies of the GaN TB parameters are energetically shifted by the valence band offset. This is a widely used ansatz [60, 61]. The on-site energies on the N sites are determined by taking a ratio of AlN and GaN parameters according to the ratio of Al and Ga nearest neighbors [37, 62]. These bulk TB parameters are obtained by fitting the TB band structures to Heyd-Scuseria-Ernzerhof (HSE) screened exchange hybrid functional density functional theory (DFT) band structures [30, 32]. Our TB model gives a very good description of the HSE-DFT band structure, as shown for example in Ref. [30], around the Γ -point. Due to its reduced number of basis states, the description of e.g. the CB at the M - and L -valleys is less good. However, from our HSE-DFT band structure calculations we find that the energetic separation $\Delta_{\Gamma-M}$ between the CB minimum at the Γ -point and the M -point in GaN is $\Delta_{\Gamma-M}^{\text{GaN}} = 3.14$ eV and in AlN it is $\Delta_{\Gamma-M}^{\text{AlN}} = 1.67$ eV. For the splitting between Γ -point and L -point we find $\Delta_{\Gamma-L}^{\text{GaN}} = 2.58$ eV and $\Delta_{\Gamma-L}^{\text{AlN}} = 1.18$ eV. Since in both systems the energetic separation between the CB minimum at the Γ -point and the L - and M -valleys, respectively, is at least 1 eV, it is justified to assume that the evolution of the energy gap in AlGa N alloys is dominated by the band structure around $\mathbf{k} = \mathbf{0}$, especially for higher GaN contents. Thus, the TB model used here should be sufficient to describe the band gap evolution in AlGa N alloys.

In the TB Hamiltonian the local strain tensor $\epsilon_{ij}(r)$ and the built-in potential $\phi(r)$ has to be included in order to accurately describe the electronic properties of the AlGa N alloy. Several authors have shown that strain effects can be introduced by on-site corrections to the TB matrix elements [6, 7]. Here we include the strain dependence of the TB matrix elements via the Pikus-Bir Hamiltonian [63, 64] as a site diagonal correction [30]. With this approach, the relevant deformation potentials for the highest valence band and lowest conduction band states at the Γ -point are included directly without any fitting procedure. The deformation potentials

for AlN and GaN are taken from HSE DFT calculations [65]. Again on the same footing as the case of the on-site energies for the nitrogen atoms, we use weighted averages to obtain the strain dependent on-site corrections for the N atoms in $\text{Al}_{1-x}\text{Ga}_x\text{N}$. Our approach is similar to that used for the strain dependence of an 8-band $\mathbf{k} \cdot \mathbf{p}$ model [63], but has the advantage that the TB Hamiltonian is sensitive to the local distribution of Al and Ga atoms. The final part of our TB model for the description of the electronic structure of $\text{Al}_{1-x}\text{Ga}_x\text{N}$ alloys is the local built-in potential $\phi(\mathbf{r})$ arising from the piezoelectric and spontaneous polarisation contributions. The built-in potential $\phi(\mathbf{r})$ is similarly included as a site diagonal contribution in the TB Hamiltonian [66–69].

Following recent experimental analysis for InGaN [70, 71] we also treat $\text{Al}_{1-x}\text{Ga}_x\text{N}$ as a random alloy. For each composition x , the band gap calculations have been repeated five times to realize different random microscopic configurations. The band gap was evaluated as the average over the different configurations for a given GaN content x according to:

$$E_g(x) = \frac{1}{N} \sum_{i=1}^N [E_{\text{CB}}^i(x) - E_{\text{VB}}^i(x)] . \quad (4.4)$$

Here N is the number of configurations, five in this case, and i denotes the microscopic configuration. E_{CB}^i and E_{VB}^i are the CB and VB edge energies.

4.3 Results

Having established the theoretical framework, we turn now to present the results of our analysis. In Sec. 4.3.1 we discuss the band gap bowing of AlGa_xN over the full composition range. Our theoretical results are compared with recent experimental data, showing good agreement. The analysis of the composition dependence of the band gap is followed by the analysis of the evolution of the band edges with GaN composition x . In the final step we focus on the optical polarisation switching and compare our results with the results from a linear interpolation of the crystal field splitting and with experimental data.

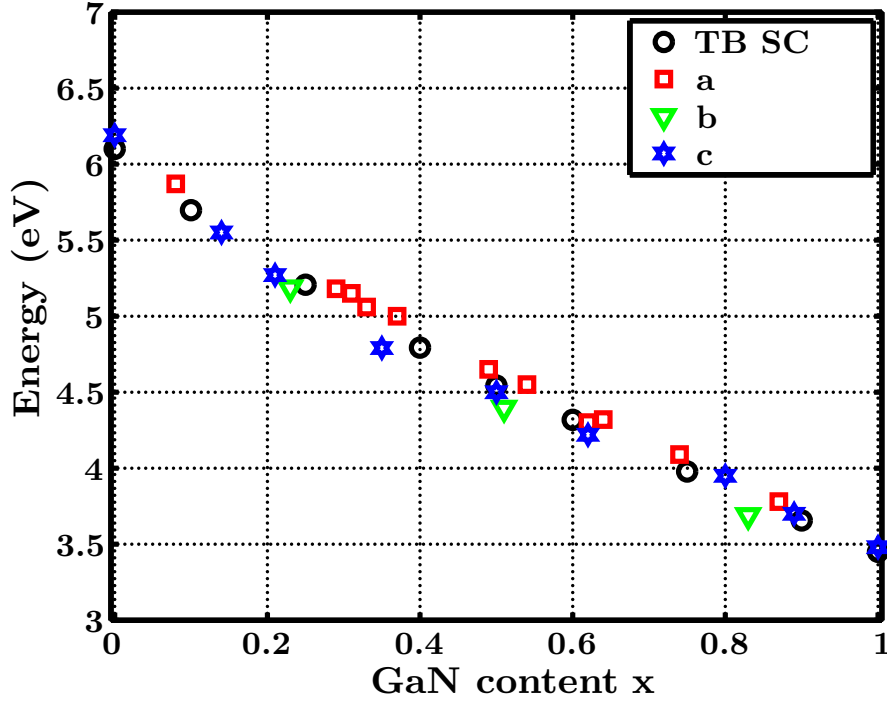


FIGURE 4.1: Evolution of the band gap energy of $\text{Al}_{1-x}\text{Ga}_x\text{N}$ with GaN content (x). The black circles represent TB supercell calculations, for which a bowing parameter of $b = 0.94$ eV can be extracted. The other data sets (a,b and c) are experimental measurements [72–74], showing good agreement between theory and experiment.

4.3.1 AlGaN band gap

The calculated band gap energy of $\text{Al}_{1-x}\text{Ga}_x\text{N}$ as a function of the GaN content x is depicted in Fig. 4.1. Additionally, Fig. 4.1 also shows recent experimental data from Refs. [72–74]. Good agreement is found between theory and experiment over the full composition range. Using Eq. (4.1) we find a band gap bowing parameter b of 0.94 eV. This lies well within the range of the reported literature values of 0.7 to 1.3 eV [40–47]. More recent data suggest a value close to 0.9 eV [40, 45–47].

The impact of random alloy fluctuations on the results can be assessed by comparing the variations in the energy gaps of the different microscopic configurations compared to the average energy gap for a given composition x . Here we find that the difference between the individual microscopic configurations and the average value of the band gap is less than 8 meV across the full composition range. This suggests that the strong localization effects associated with the InN-containing alloys, InGaIn and AlInN [30, 75], are not as prevalent in $\text{Al}_{1-x}\text{Ga}_x\text{N}$.

We note here that for device design not only the composition dependence of the energy gap is important but that it is also useful to know how the bowing in the band gap is distributed between CB and VB edges.

4.3.2 Composition dependence of the band edge energies

Figure 4.2 shows the calculated CB and VB edge energies as a function of the GaN content x in $Al_{1-x}Ga_xN$ systems. From Fig. 4.2 it can be seen that most of the band gap bowing arises from bowing of the CB edge; the VB edge energy varies almost linearly with x . More specifically, we find band edge bowing parameters of $b^{CB} = 0.78$ eV and $b^{VB} = -0.16$ eV for the CB and VB edges, respectively. These bowing parameters were obtained by fitting to:

$$\begin{aligned} E_{CB}^{AlGaN} &= x (E_g^{GaN} + \Delta E_{VB}) + (1-x) E_g^{AlN} - b^{CB}x(1-x) , \\ E_{VB}^{AlGaN} &= x\Delta E_{VB} - b^{VB}x(1-x) . \end{aligned} \quad (4.5)$$

with the AlN VB edge taken as the zero of energy. Here b^{CB} and b^{VB} denote the bowing parameters for the CB and VB edges, respectively. For the VB offset ΔE_{VB} between GaN and AlN, we assume a value of $\Delta E_{VB} = 0.9$ eV. This is within the range of reported literature values $[\Delta E_{VB}^{GaN/AlN} = 0.15 - 1.4\text{eV}]$ [50, 76–78].

Given the near linear variation of the VB edge energy it might be expected that the crystal field splitting also varies linearly in AlGa_xN. The variation of the crystal field splitting and its effect on optical polarisation switching in AlGa_xN is studied in the next section.

4.3.3 Optical polarisation switching

When looking at the bulk band structure of the two binaries GaN and AlN, the VB ordering is different in these two systems. While in GaN the topmost VB is of Γ_9 symmetry, it is of Γ_{7+} symmetry in AlN [79]. This difference in symmetry leads to a difference in polarisation properties of the light emitted from GaN or AlN [79]. The origin of the difference in the VB ordering is attributed to the difference in the sign of the crystal field splitting energies in GaN and AlN, where the crystal field splitting is defined as the difference in energy Δ_{CF} between the two

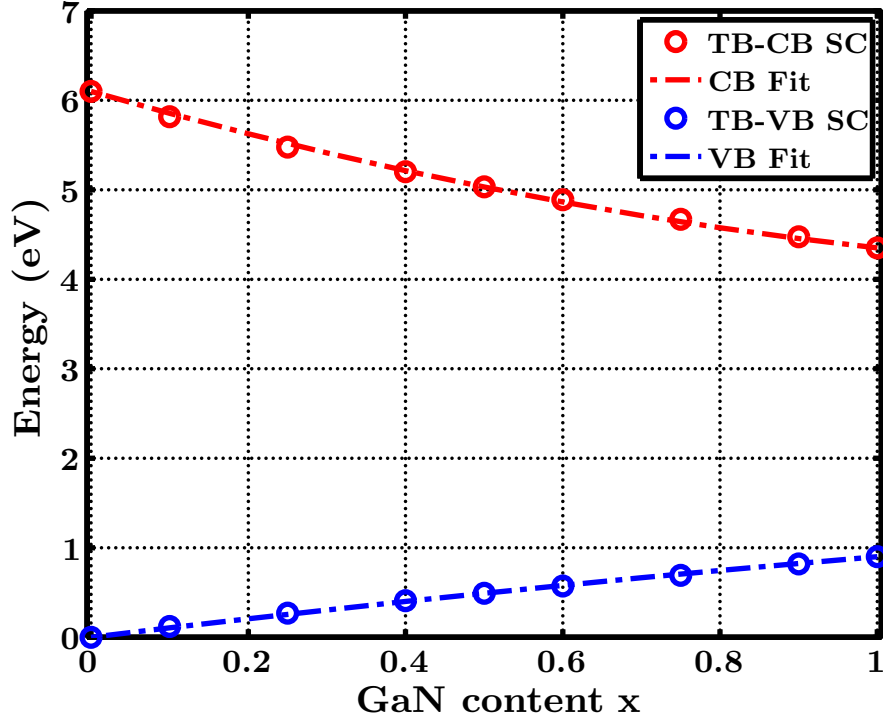


FIGURE 4.2: Calculated evolution of the CB and VB edge energies of $\text{Al}_{1-x}\text{Ga}_x\text{N}$ with GaN content x . The results for the CB edge (TB-CB SC) and VB edge (TB-VB SC) from the TB supercell calculations are given by the open circles. The fit to the TB data, using Eq. 4.5, is given by the dashed dotted lines. Most of the calculated bowing is in the CB with a bowing parameter of $b^{\text{CB}} = 0.78$ eV, whereas the variation of the VB edge is nearly linear ($b^{\text{VB}} = -0.16$ eV).

topmost VB states at $\mathbf{k} = \mathbf{0}$, when the spin-orbit interaction is ignored. Therefore the question arises at which composition x does the character of the VB edge change? A widely used approximation is to assume that Δ_{CF} changes linearly with composition x . However, this assumption is used mainly due to the lack of more detailed information on the variation of the crystal field splitting. Here we now use our microscopic TB model to study this question.

Values reported for Δ_{CF} in GaN lie in the range of 9-38 meV, while for AlN values between -169 meV and -295 meV can be found [41, 80]. As discussed above, the difference in the sign of Δ_{CF} reflects the difference in the VB ordering of bulk GaN and AlN. Neglecting the weak spin-orbit coupling, the topmost valence band in AlN mainly has p_z character (the band is a superposition of atomic p_z basis states pointing along the c -axis), giving rise to TM polarised emission. By contrast, the topmost valence band in GaN is a mixture of p_x and p_y states, giving TE polarised emission. Hence, when one alloys the two binary compounds, the optical polarisation of the emitted photons will switch at a certain composition.

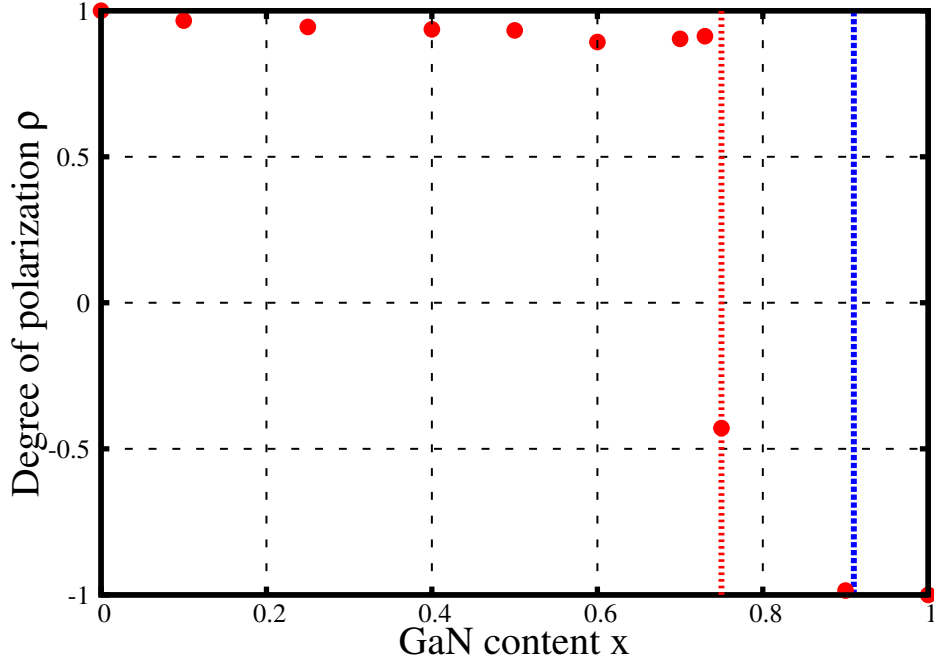


FIGURE 4.3: Calculated degree of polarisation ρ of the topmost VB state in $Al_{1-x}Ga_xN$ as a function of GaN content x . Our data (filled circles) shows a change in the optical polarisation direction at close to $x = 0.75$ (red dashed line). The line at $x = 0.91$ (blue dashed line) represents the crossing point expected from a linear variation of Δ_{CF} .

A linear interpolation of the values from our DFT calculations for Δ_{CF} ($\Delta_{CF}^{GaN} = 23$ meV, $\Delta_{CF}^{AlN} = -240$ meV) gives the optical polarisation switching at $x = 0.91$. Given that the VB edge energy changes almost linearly with GaN content, it might be presumed that a linear interpolation is a reasonable assumption for Δ_{CF} in AlGaIn alloys. To analyze the optical polarisation switching and the change in Δ_{CF} in more detail, we define, similar to [53], the degree of optical polarisation (ρ) as:

$$\rho = \frac{I_z - I_{x+y}}{I_z + I_{x+y}}. \quad (4.6)$$

The fraction of p_z -like character in the topmost valence state is denoted by I_z , while I_{x+y} denotes the combined fraction of p_x - and p_y -like character. This approach, by taking the orbital character of the valence band, is similar to the approach used in Ref. [81] to address the optical polarisation characteristics of nitride-based systems. In Fig. 4.3 the parameter ρ varies between 1 when the valence band edge is entirely made up of p_z -like orbitals and -1 when the $p_{x,y}$ orbitals form the basis of the topmost valence band. From Fig. 4.3 we estimate the switching point to be around $x = 0.75$. This is at a significantly lower composition than would be

expected from a linear interpolation. It should be noted that we have neglected spin-orbit coupling effects in the calculations. However, similarly to crystal field splitting energies, there is also a large degree of uncertainties in the values of the spin-orbit coupling energies. Values ranging from 5 to 22 meV can be found in the literature for GaN. Therefore, the effects of the state mixing introduced by the inclusion of the spin-orbit coupling in the calculations are probably still smaller than the uncertainties in the spin-orbit coupling and crystal field splitting energies. Furthermore, since the difference in the valence band structure between GaN and AlN is mainly introduced by the large difference in the crystal field splitting energy, our theory should include the main contribution that affects the optical polarisation switching. Experimentally, Neuschl *et al.* [47] found, based on polarisation dependent photoluminescence spectroscopy, the optical polarisation to switch in the range $x = 0.68 - 0.85$. Netzel *et al.* [82] report an optical polarisation switching range of $x = 0.79 - 0.94$ while Nam *et al.* [53] estimate the transition at $x = 0.75$. However, these reported values are affected by the presence of strain effects due to the underlying substrate. Compressive strain causes a shift to lower x values while tensile strain shifts the polarisation switching to higher Ga compositions. Neuschl *et al.* [47] used $\mathbf{k.p}$ theory to correct for the effect of strain originating from the underlying substrate. In doing so they find an adjusted range of $x = 0.86 - 0.96$. Given the difficulties in experimentally determining the degree of optical polarisation, as discussed in detail in [47], plus the uncertainties in AlGa_N material parameters, our value is close to the reported experimental data.

Our calculations show that the optical polarisation switches at a much higher Al composition than would be predicted using a linear interpolation, thus allowing access to a significantly larger range of TE emitting Al-containing alloys than might be expected.

To quantify the deviation from a linear interpolation we apply a Végard's law like expression to Δ_{CF} , similar to Eq. (4.1):

$$\Delta_{CF}^{AlGaN} = x\Delta_{CF}^{GaN} + (1-x)\Delta_{CF}^{AlN} - b^{CF}x(1-x). \quad (4.7)$$

Here, b^{CF} denotes the bowing parameter of Δ_{CF} . Using our previous result that the optical polarisation switches (and hence $\Delta_{CF} \approx 0$) at $x \approx 0.75$ along with the values of -240 meV and 23 meV for Δ_{CF}^{AlN} and Δ_{CF}^{GaN} , respectively, we find a

bowing parameter of $b^{\text{CF}} \approx -0.23$ eV for Δ_{CF} . It should be noted that a similar behaviour was recently reported in Ref. [47]. The authors also report deviations from a linear variation of Δ_{CF} with composition x in $\text{Al}_{1-x}\text{Ga}_x\text{N}$ systems. The extracted bowing parameter in Ref. [47] for Δ_{CF} is $b^{\text{CF}} = -0.12_{+0.12}^{-0.06}$ eV. Therefore, our finding of a bowing in the crystal field splitting energy is consistent with the experimental data in Ref. [47].

4.4 Conclusions

In summary, we employed an atomistic TB model that includes local alloy and polarisation effects in order to study the band gap bowing and optical polarisation switching of wurtzite $\text{Al}_{1-x}\text{Ga}_x\text{N}$ as a function of Ga content x . Our calculation of the band gap energy is in good agreement with experiment across the full composition range. We extracted a bowing parameter for the band gap of $b = 0.94$ eV, which is also in good agreement with experiment. We further analysed the origin of this bowing in the CB and VB edges and fitted bowing parameters to both; $b^{\text{CB}} = 0.78$ eV and $b^{\text{VB}} = -0.16$ eV. Finally, we calculated the composition at which the band edge optical emission switches between the TE and TM polarisation directions. We found the switchover to be in the region $x \approx 0.75$ which is at a much higher Al composition (25%) than would have been expected (9%) assuming a linear variation of the crystal field splitting in our calculations. This observed non-linear behaviour of the crystal field splitting is consistent with recent experimental observations.

Chapter 5

Electron and hole localization in $\text{In}_x\text{Ga}_{1-x}\text{N}$ quantum wells

5.1 Introduction

We have just seen how the band gap of $\text{Al}_{1-x}\text{Ga}_x\text{N}$ alloys spans 6.2 to 3.45 eV, the upper part of the band gap range spanned by the III-nitrides. We now look at $\text{In}_x\text{Ga}_{1-x}\text{N}$ alloys, which have a band gap range of 3.45 to 0.78 eV. This corresponds to emission wavelengths from 380 to 1800 nm, from the visible to near-infrared range of the spectrum. Blue light emitting diodes based on $\text{In}_x\text{Ga}_{1-x}\text{N}/\text{GaN}$ quantum wells (QWs) form the basis for white LEDs, by pumping a phosphor they also emit in the yellow to amber range. They are also commonly used in Blu-ray DVD lasers. Despite being widely used, these structures are not very well understood at a microscopic level. They have very high defect densities but still exhibit high quantum efficiencies [3, 4]. This is commonly explained in terms of carriers being spatially localised due to local alloy fluctuations, which therefore prevent them from diffusing to defects [3, 4, 48, 83]. InN has very different physical properties from AlN and GaN. One example is the band gap 0.7 eV in InN and 6.2 in AlN. Furthermore there is a very large lattice mismatch of about 10% for InN/GaN and 11% for InN/AlN. Thus, the inclusion of Indium causes a much larger perturbation of the local atomic structure and band structure in GaN than Al. The lattice mismatch is much smaller in AlN/GaN systems. Both of these factors result in InGaN systems having interesting localisation effects. A local atomistic description of the QW is thus required to analyse these localisation

effects. Although the importance of alloy fluctuations has previously been reported in experimental studies [84, 85], these atomistic effects have not been previously modelled in QW structures. Atomistic studies, to date, have focused on bulk ZB [86–88] or WZ [40, 50, 89, 90] InGa_N alloys. InGa_N QWs of realistic dimensions are generally studied using continuum-based theoretical methods [91–93], but these models inherently overlook alloy or built-in field fluctuations on a microscopic level. In WZ InGa_N systems these local fluctuations are much more severe compared to, for example, ZB InGaAs alloys. The large lattice mismatch and difference in band gap contribute to this as well as the strong electrostatic built-in fields due to strain dependent piezoelectric response, as well as spontaneous polarisation. Thus the electronic structure of InGa_N/Ga_N QWs is strongly affected by local alloy fluctuations and an atomistic description of the structure is required.

We implement here the same model as in chapter 4, to investigate the effect of local alloy fluctuations on the localisation of electron and hole states in $\text{In}_x\text{Ga}_{1-x}\text{N}/\text{Ga}_\text{N}$ QW structures. Special consideration must be given to the built-in potential to make sure it is continuous at the boundaries while also correctly accounting for the contribution from the clamped ion term in the polarisation potential. We used supercells containing just over 80,000 atoms with approximately the following dimensions; 10nm x 9nm x 10nm. Two compositions were examined, $\text{In}_{0.25}\text{Ga}_{0.75}\text{N}$ and $\text{In}_{0.10}\text{Ga}_{0.90}\text{N}$. We used the participation ratio (as defined in Sec. 5.2.2) as a metric for comparing the localisation of states and show how features and trends seen in the participation ratio affect the overlap between states. We further analyse the effect of well width fluctuations (WWFs) on the electron states for both compositions. These WWFs have been found in experimental studies to be located at the upper QW interface [94–97]. The diameter of these well width fluctuations is found to be $\approx 5\text{-}10$ nm, while their height is between one and two monolayers. To treat such fluctuations, we assume disk-like WWFs with a diameter of 5nm and a height of two monolayers residing on the upper QW interface. Following experimental evidence we treat InGa_N as a random alloy [94–96, 98–100] and we show how these random fluctuations strongly localise the hole states in the *c*-plane and how this in turn effects the overlap. In other recent DFT studies of local alloy fluctuations, the method of special quasi-random structures is introduced [101]. In DFT quasi-random structures are needed because one has to deal with small supercells. Quasi-random structures allow you to look at approximately 200 atoms in a cell, which is sufficient for conventional alloys. However, localised cluster states

have an extent substantially larger than 200 atoms. As a result, we need large supercells to investigate effects of these statistically rare clusters.

Our primary motivation for modeling these structures is not to directly improve the current technology, although of course this is also an ancillary objective, but to validate our model so it could be implemented within the DEEPEN research project. The aim of DEEPEN is to develop a multi-scale simulation environment for the modeling of devices using an atoms to systems approach. The acronym stands for ‘from atom-to-Device Explicit simulation Environment for Photonics and Electronics Nanostructures’. Within this project, the role of this work was to validate our capability of providing an atomistic description of gallium-nitride-based nanostructured materials by comparing our results to experimental data provided by Paul-Drude-Institute in Berlin, another DEEPEN partner.

The work in this chapter was carried out in collaboration with Dr. Stefan Schulz, also in the Photonics Theory Group here in Tyndall. Using codes developed previously by Dr. Miguel Caro, Dr. Schulz generated supercells which I then relaxed using `gulp` [58]. With the relaxed atomic positions, Dr. Schulz constructed the Hamiltonian which included the on-site corrections for the local strain and built-in fields. I then calculated the eigenstates and analysed the localisation properties of these states and how this localisation affected the overlap between carriers. Presented in the rest of this chapter are the results of this analysis for four different structures, namely the two different compositions with and without WWFs. For each case a number of different configurations were calculated to probe the variation in the characteristics observed, but for the sake of brevity we present one configuration for each case that is indicative of the features found and show the others in Appendix B.

5.2 $\text{In}_{0.25}\text{Ga}_{0.75}\text{N}$ flat quantum wells

In this section we present our analysis of the localisation properties of $\text{In}_{0.25}\text{Ga}_{0.75}\text{N}$ flat QWs. We begin by discussing the metrics used to measure the localisation throughout.

5.2.1 Localisation metrics used

Once the Hamiltonian was correctly constructed and then diagonalised we looked at how the eigenstates were spatially distributed throughout the cell. The most commonly used measure or metric of this property of the wavefunctions is called the localisation length. It is defined as;

$$l_{loc} = \sum_i (\bar{\mathbf{r}} - \mathbf{r}_i |\psi_i|^2)^2, \quad (5.1)$$

where $|\psi_i|^2$ is the total probability density on site i and $\bar{\mathbf{r}}$ is defined as the centre of localisation;

$$\bar{\mathbf{r}} = \sum_i \mathbf{r} |\psi_i|^2. \quad (5.2)$$

The centre of localisation, analogous to the centre of mass, defines a point in the supercell about which the probability density is balanced. The localisation length is thus a certain radius about this centre of localisation inside which the majority of the probability density is contained. This metric, however, turned out to be not easily applied to the wavefunctions calculated in this work. It works best when describing states that are localised in one lobe or peak. As can be seen later in Fig. 5.6 some of the hole states are strongly localised in two or three lobes. The centre of localisation would then, by definition, be located at a point precisely between these lobes and thus giving a much larger localisation length than is actually the case. For this reason, we initially tested but then did not implement the localisation length to measure the distribution of probability density throughout the supercell.

5.2.2 Participation Ratio

The participation ratio (PR) is a much simpler but perhaps less intuitive way to measure the localisation of a wavefunction. It is defined as:

$$P_r = \sum_{i,\alpha} |\psi_{i,\alpha}|^4, \quad (5.3)$$

where the index i runs over the sites and α denotes the orbitals on each site. A perfectly localised state that would have all its amplitude on one orbital of one

site would give a PR of 1. Similarly, a perfectly delocalised state that would have its amplitude spread evenly over all orbitals and all sites would give a PR equal to $1/MN$, where N is the number of atoms in the supercell ($\approx 80,000$) and M is the number of orbitals per atom (4). Thus, presuming of course that our states are normalised to 1 as they are, the PR is a measure of localisation that varies here from $\approx 10^{-5}$ to 1. For the purpose of introducing the quantities we use to measure localisation and overlap, we will use the case of flat $\text{In}_{0.25}\text{Ga}_{0.75}\text{N}$ QWs to present them. Shown below in Fig. 5.1 are the participation ratios for the first 75 electron (Fig. 5.1(a)) and hole states (Fig. 5.1(b)) for one of the configurations of the flat QWs with 25% indium content.

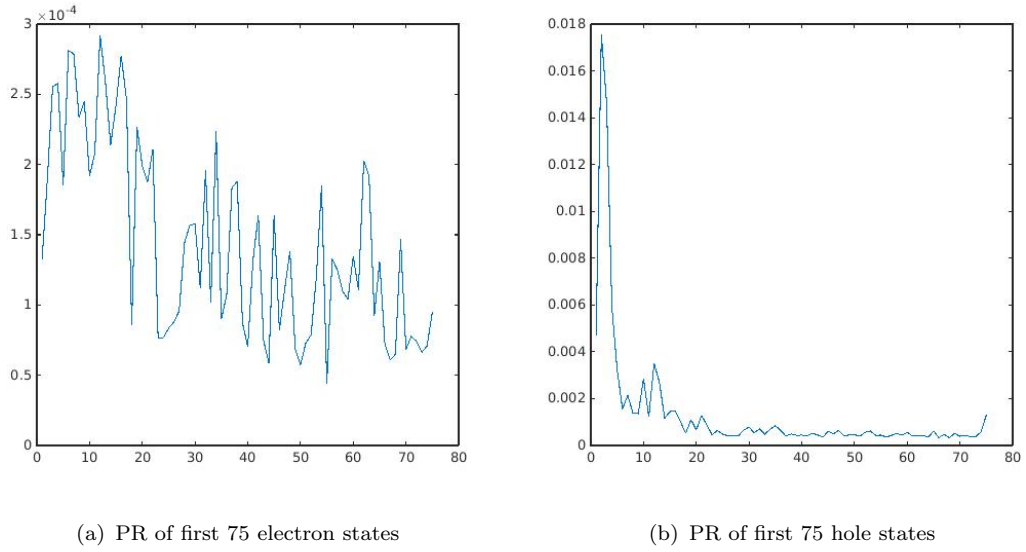


FIGURE 5.1: Participation ratio of first 75 electron and hole states.

Note how the holes are strongly localised for the first 5 or so states, are still relatively localised up 25 states and then beyond this they become more delocalised. In the case of the electrons it can be seen how roughly the first 20 states are more localised relative to the higher states, but there is still a large variation in the PR of higher states. Notice also the difference in scale in the two figures, the holes are much more strongly localised than the electrons. This is to be expected from a basic analysis of the effective masses of the electron and hole states. A simple linear interpolation of the published experimental values for the electron and hole effective masses of InN [102, 103] and GaN [104, 105] give much larger values for the effective mass of the holes ($1.457 m_0$) than that of the electrons ($0.177 m_0$) in $\text{In}_{0.25}\text{Ga}_{0.75}\text{N}$. This order of magnitude difference is more clearly seen in Fig. 5.2 where the PR for all states, both holes and electrons, is normalised to the PR of

the first hole state. Note also the axes represent the difference in energy from the top of the conduction band for the electrons and from the top of the valence band for the holes.

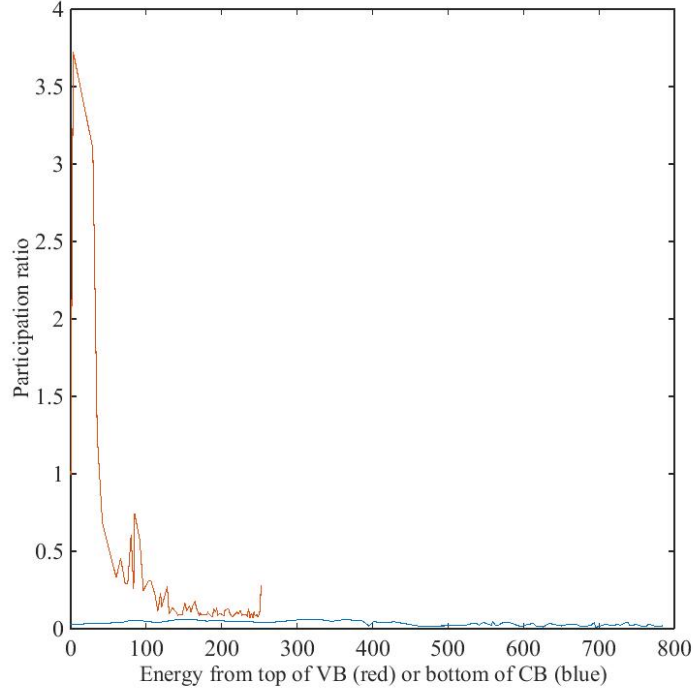


FIGURE 5.2: The PR for electron and hole states, normalised to the first hole state and plotted on the same energy scale.

The delocalisation of the electron states relative to the hole states can clearly be seen in Fig. 5.2. It also shows how the first 75 electron states cover a much larger energy range than the first 75 holes. The energy separation between the individual states, starting from the ground state up to the 90th state for both electrons (blue) and holes (red) is plotted in Fig. 5.3.

5.2.3 Charge density overlap

In order to quantify and compare the overlap of different pairs of states we define the 3-dimensional charge density overlap, following [106], as;

$$\mathcal{O} = \sum_{\mathbf{r}_1} \sum_{\mathbf{r}_2} \sum_{\mathbf{r}_3} \rho_e(\mathbf{r}_1, \mathbf{r}_2, \mathbf{r}_3) \rho_h(\mathbf{r}_1, \mathbf{r}_2, \mathbf{r}_3), \quad (5.4)$$

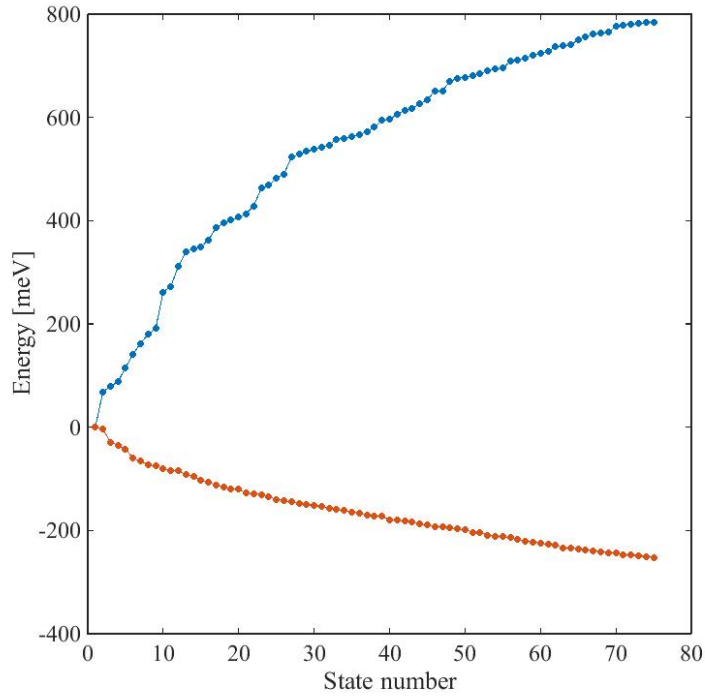


FIGURE 5.3: How the energy separation of the individual states varies for electrons (blue) and holes (red).

where ρ is the charge density for either the electrons or holes at a given site denoted by the cartesian coordinates $\mathbf{r}_1, \mathbf{r}_2$ and \mathbf{r}_3 . Shown in Fig. 5.4 is the charge density overlap for the first 75 electron and hole states for the same configuration as the previous figures. Again the axes show the energy separation between the states, similar to Fig. 5.3. The main feature we want to note here is the ‘shelf’ in this overlap surface, there is a lower overlap between the first 17 electron states and all the hole states. After this there are some electron states that have a consistently higher overlap with all hole states. Looking again at the PR of the electrons in Fig. 5.1(a) we can see that it is the first 17 electron states that have a slightly larger PR. This increased localisation in the electron states gives rise to poor overlap with all the highly localised hole states. Further analysis in the next section shows that the increased overlap arises from electrons that are in higher subbands, with reduced localisation along the c-axis direction. The spikes in the PR for the higher electron states correspond to electron states that have low overlap in Fig. 5.4. We see that there is a direct correlation between the electron PR and the charge density overlap. There is no similar threshold for the hole states that we could find. This calculation, in other configurations, was run for 200 hole states, which reached 375 meV into the valence band, and no discernible change

in the overlap was found. The first few hole states are strongly localised in the c -plane; all hole states studied were strongly localised along the c -axis direction, and any increase in overlap is due to delocalised electron states.

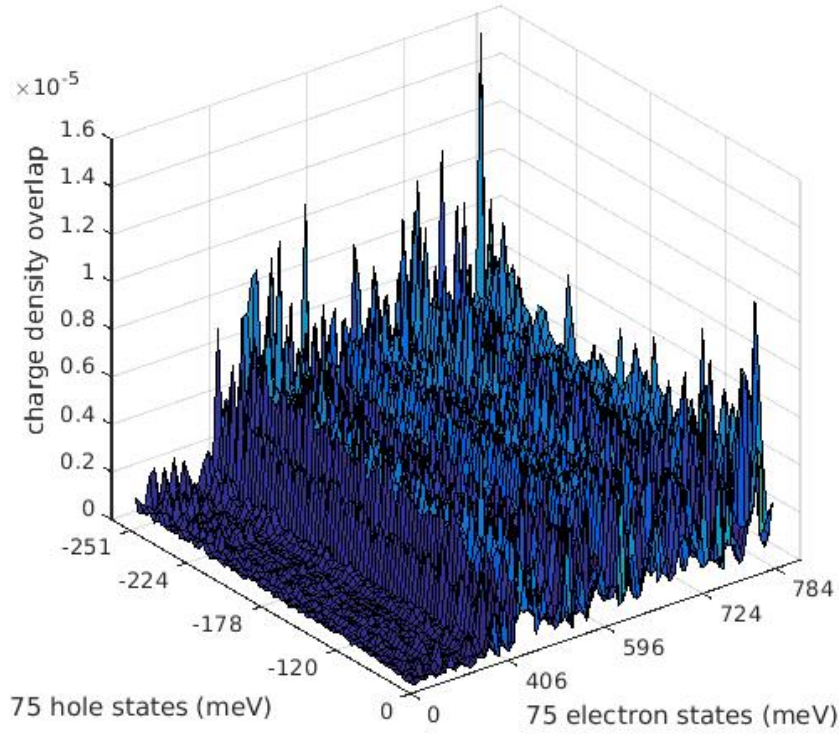
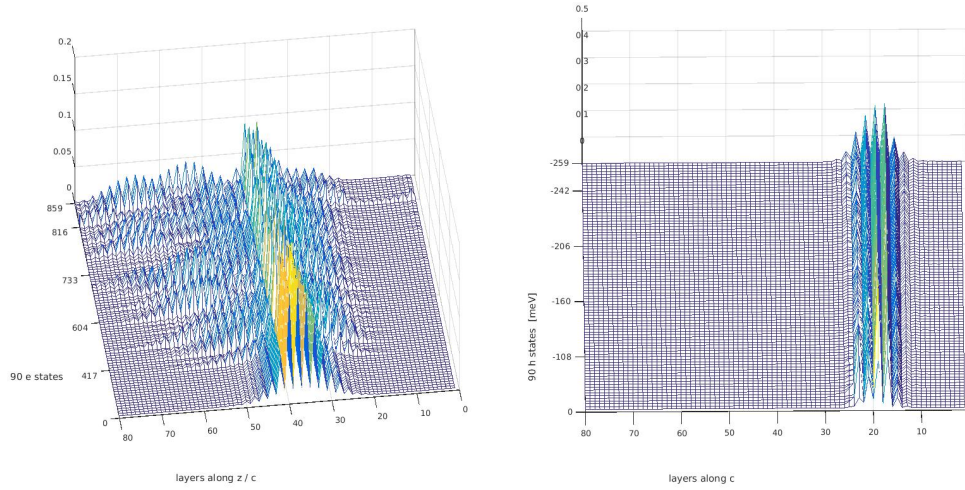


FIGURE 5.4: Charge density overlap for the first 75 electron and hole states. ($E_g = 2.03\text{eV}$)

5.2.4 Probability density in a layer

So as to better examine the nature of the localisation of the states we sum over the amplitude of all the sites in a single layer and plot the probability density contained in each layer for all states in Fig. 5.5. The QW is located between layers 18 and 38. We can see, due to the built-in polarisation potential, that the holes are strongly localised along the c -axis (z -direction) and pinned to the lower interface of the QW. The lowest electron states are then confined to the upper interface of the QW, again due to the built-in potential. The probability density of the electron states is more spread out along the c -axis. The first 17 electron states in Fig. 5.5(a) are much more strongly localised along the c -axis direction than the higher states. These correspond to the first confined electron band for

different values of \mathbf{k} . They are also the same states that have a higher PR and low charge density overlap with the hole states. After these states we see the emergence of the second confined band. Notice how some of its probability density leaks into the barrier but also deeper into the QW towards the hole states, hence increasing the overlap.



(a) Probability density of electron states in each monolayer. (b) Probability density of hole states in each monolayer.

FIGURE 5.5: Probability density of (a) electron and (b) hole states in each of the 80 monolayers of the supercell.

5.2.5 Hole localisation

As can be seen from the PR in Fig. 5.2 and also from plotting the probability density in each layer (Fig. 5.5(b)) the holes are much more strongly localised than the electrons. We can see that the holes are localised along the c -direction due to the built-in potential from Fig. 5.5(b). There still remains a question of whether the holes are localised in the c -plane. To investigate this we plot the hole probability densities in the c -plane as isosurfaces that contain 10% or more of the maximum probability density. Figure 5.6 shows how the first five hole states are strongly localised in the c -plane due to the local alloy fluctuations. The local environment of the sites with the highest probability density for the hole states was found to have a high indium content locally on both first and second nearest neighbours. By comparison, the first electron state (Fig. 5.6(f)) is delocalised throughout the cell.

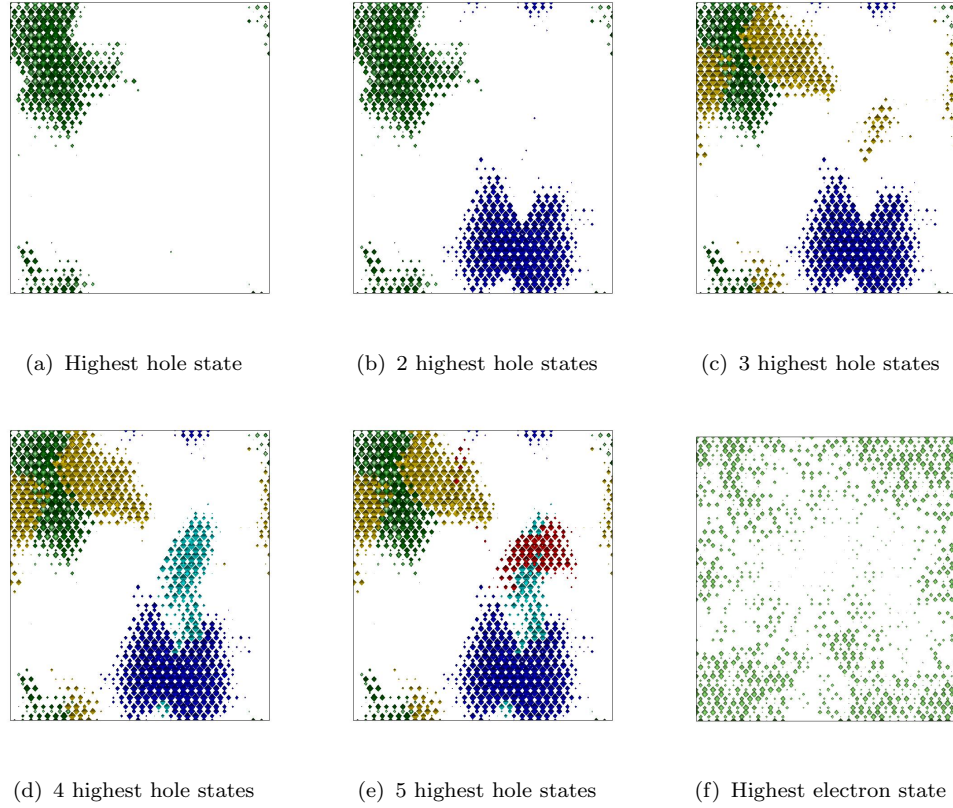


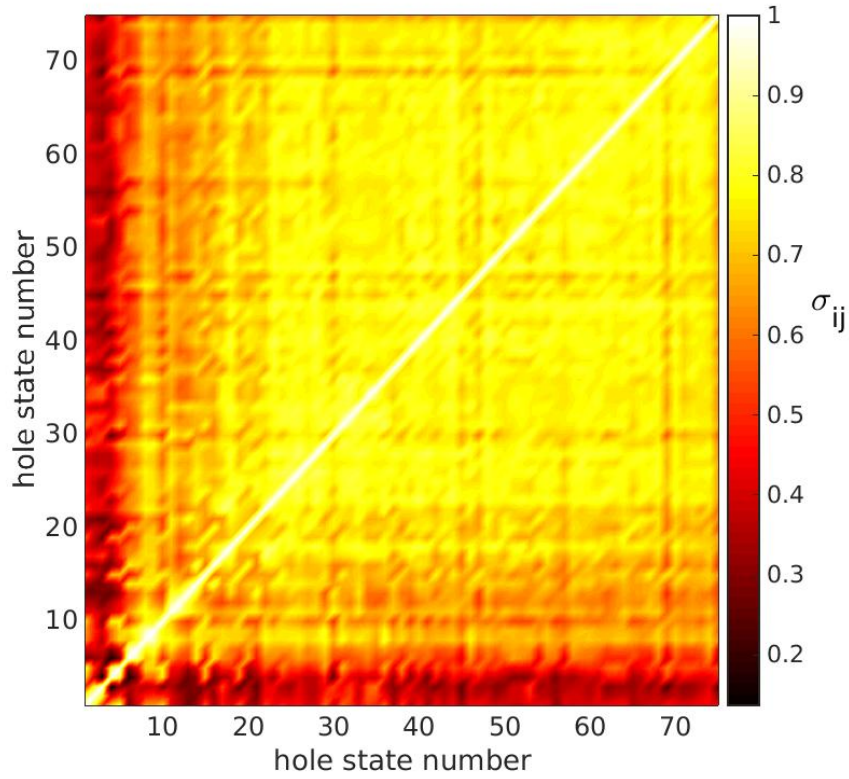
FIGURE 5.6: Localisation of the first five holes and first electron state projected onto the c plane.

5.2.6 Hole overlap

When examining Fig. 5.6 we note that although strongly localised, some of the first few hole states can have a significant overlap with each other. Take for example the first and third hole state in Fig. 5.6(c), where the first (green) and third (yellow) state occupy the same region of the cell. We know from Fig. 5.5(b) that both these states are localised along z at the same interface between the barrier and QW. A similar behaviour can be seen between states four (light blue) and five (red). Hence, in order to measure the overlap between hole states, we define σ as;

$$\sigma_{mn} = \sum_i |\psi_{m,i}| |\psi_{n,i}|, \quad (5.5)$$

where $|\psi_{m,i}| = \sqrt{\rho_{m,i}}$ with $\rho_{m,i}$ being the hole charge density at site i for state m . The quantity σ , which varies between zero and one, then measures the relative overlap of the hole states by summing over the overlap at each site. Shown in Fig. 5.7 is σ_{mn} for the 75 highest hole states of this configuration.

FIGURE 5.7: σ for the first 75 hole states.

Notice how in general the first six states have very poor overlap with higher states. This is again due to strong in-plane localisation and correlates with the very high PR of the first 6 states in Fig. 5.1(b). Some of these states do have good overlap with each other; bright yellow spots can be seen between states one and three as well as four and five in Fig. 5.7. A general increase in overlap is seen between states 8 and 20; this is due to increasing delocalisation of states in this region. This is again reflected in the PR in Fig. 5.1(b). After 20 states there is generally good overlap between the holes. The states are relatively delocalised in the c -plane and once again this corresponds to the region after 20 states with lower PR in Fig. 5.1(b). In an infinite solid, the transition between localised and delocalised states takes place at a well-defined mobility edge, with the hole states above the mobility edge being localised and while those below this edge are delocalised. It is not possible to define an exact mobility edge in the finite-size supercells considered here. It is likely however to be in the region between 10 and 20 hole states, beyond carriers can propagate from one delocalised state to another. The red lines through this region in Fig. 5.7 represent states further away from the band edge that are localised in the c -plane. An example of such a state is the 69th hole state, it has

poor overlap with most states except for ones that are similarly localised in the c -plane like the 15th state. The projection in the c -plane of the probability density of these two states is plotted in Fig. 5.8. The high peak of the probability density for both states is situated in the same region, hence they have good overlap with each other but poor overlap with the other hole states.

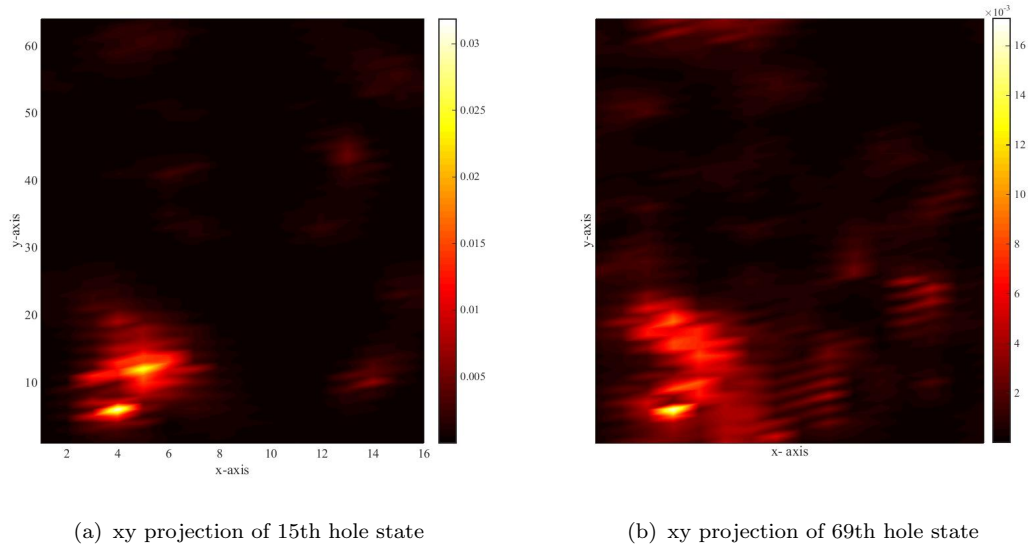


FIGURE 5.8: Comparison of the localisation in the c -plane of two states that have poor overlap with the other hole states but have a strong overlap with each other.

5.2.7 Summary of $\text{In}_{0.25}\text{Ga}_{0.75}\text{N}$ flat QWs.

In these structures the high InN content gives rise to a strong built-in polarisation potential which confines the electrons and holes to opposite sides of the active layer in the QW. It is only when the second band of electron states is reached due to these higher electron states being more delocalised in the c -axis direction, that there is an increase in overlap between electrons and holes. The high InN content also gives rise to strong in-plane localisation for the highest hole states. Local alloy fluctuations and In clustering give rise to deep local potentials in which the highest hole states are trapped. This further deteriorates the overlap between electron and hole states. Overall, the calculated electron states remain delocalised in the c -plane, but the highest hole states are localised, with the mobility edge between localised and delocalised hole states estimated to occur between the 10th and 20th hole state, about 80 to 120 meV below the highest valence state.

5.3 $\text{In}_{0.25}\text{Ga}_{0.75}\text{N}$ quantum wells with well width fluctuations

We next analyse the effect of well width fluctuations on the localisation properties of the electrons. Experimental studies [94–97] show that WWFs with a diameter of $\approx 5 - 10\text{nm}$ and a height of one to two monolayers develop during the growth of $\text{In}_{0.25}\text{Ga}_{0.75}\text{N}/\text{GaN}$ QWs. We model these WWFs with a disk of 5nm diameter and a height of two monolayers placed at the upper interface of the QW.

The main effect of WWFs on these QWs is that they localise the first electrons in the c -plane. The holes are largely unaffected by the WWFs since they are localised at the opposite interface of the QW. The lower electron states are localised within the disk of the WWFs as shown in Fig. 5.9. All other properties of the electrons and holes follow closely the behaviour of the flat $\text{In}_{0.25}\text{Ga}_{0.75}\text{N}$ QWs. The PR for the electrons have the same features as in the flat case; the first 20 or so states belonging to the first confined band have a slightly larger PR than the higher states. The probability density in each monolayer (Fig. 5.5) is also largely unchanged for both electrons and holes.¹

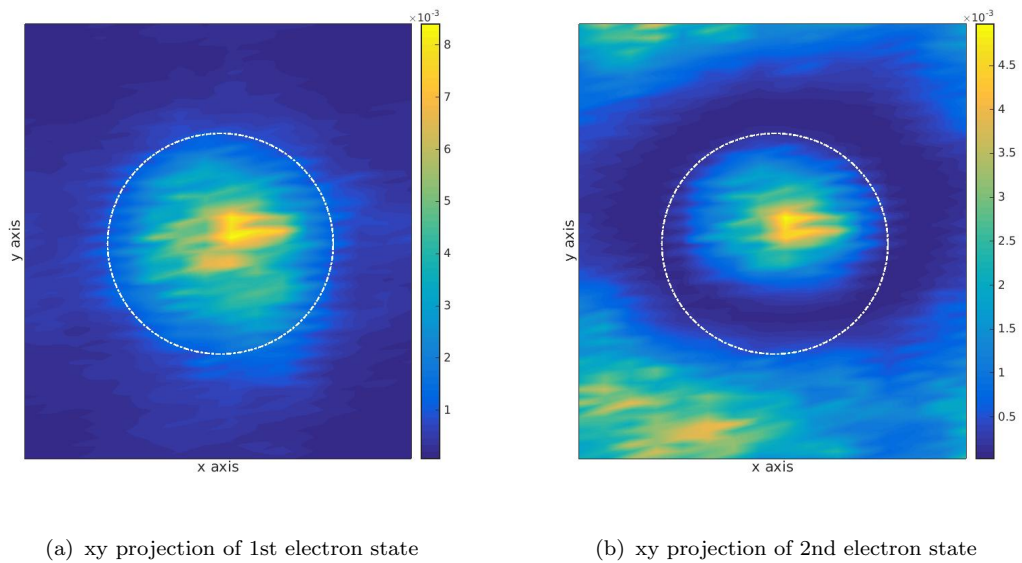


FIGURE 5.9: The first electron state is strongly localised in the c -plane by the WWF (marked by the white circle), while the second electron state is partly localised by the WWF.

¹The corresponding figures are not included here to avoid repetition and can be found in Appendix B.

This in-plane localisation of the electrons within the WWFs has the effect of reducing their overlap with the hole states that are already strongly localised in the c -plane. This is shown in Fig 5.10. The charge density overlap for these QWs with WWFs has all the same features as the flat case except for the scale. The magnitude of the overlap is reduced by an order of a factor of 2 compared to the flat case. This is, perhaps, due to the fact that due to the WWFS the QW is, on average, wider than the flat case and as a result the carriers have a greater spatial separation, but we are not certain of this.

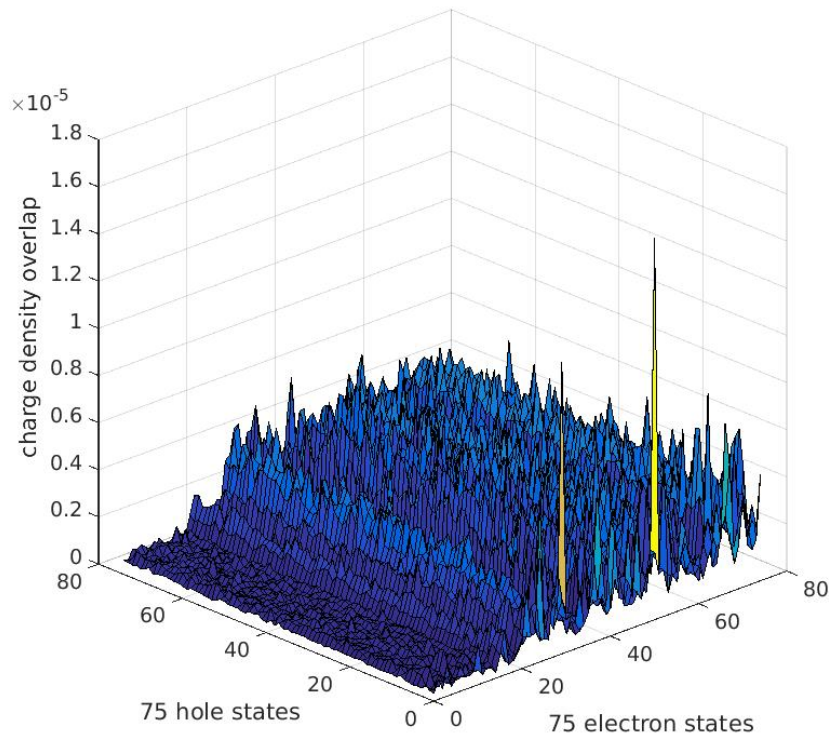


FIGURE 5.10: Charge density overlap for the first 75 electron and hole states in an $\text{In}_{0.25}\text{Ga}_{0.75}\text{N}$ including a WWF.

Optical recombination is most likely to involve the lowest electron state due to the large energy separation between it and higher electron states. Shown in Fig. 5.11 is the charge density overlap between the first electron state and the 20 highest hole states for the flat QW (red) and the WWF case (blue). In QW with WWFs we see a general poor overlap in contrast to the flat QW, due to the electron ground state being localised within the WWF. The improvement in overlap with hole states 3 and 9 is as a result of these states being localised in the same region of the c -plane as the first electron state, as shown in Fig. 5.12(a) and Fig. 5.12(b).

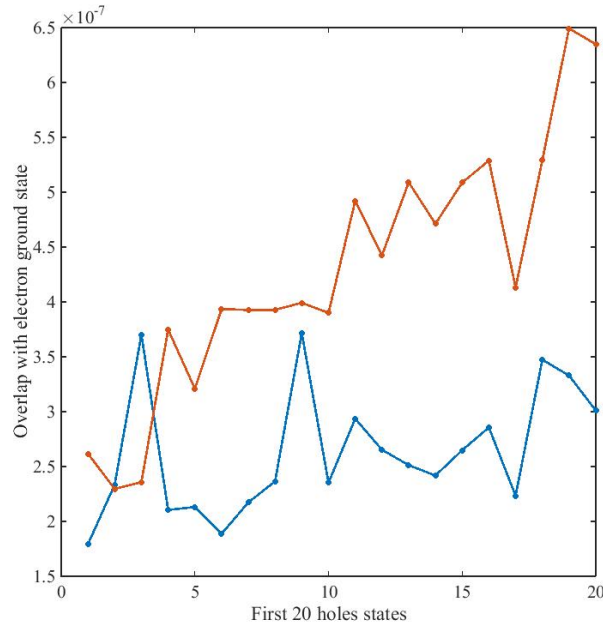
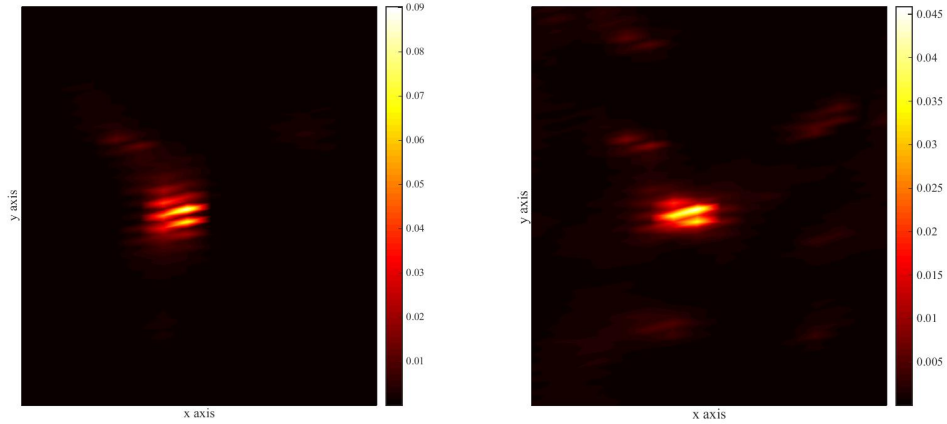


FIGURE 5.11: Charge density overlap between the electron ground state and the first 20 hole states for flat QWs (red) and QWs with WWFs (blue).



(a) xy projection of 3rd hole state

(b) xy projection of 9th hole state

FIGURE 5.12: The hole states that give an improved overlap with the ground state electron, as shown in Fig. 5.11, are both localised in the centre of the QW.

In summary the WWFs cause the electrons to localise in the c -plane which further deteriorates the overlap with the hole states.

5.4 $\text{In}_{0.10}\text{Ga}_{0.90}\text{N}$ flat quantum wells

We now turn our attention to the lower composition $\text{In}_{0.10}\text{Ga}_{0.90}\text{N}$ flat QWs. Again, we begin by looking at the participation ratio.

5.4.1 Participation Ratio

A similar behaviour to that of the structures with 25% InN content in terms of the PR is observed, with the holes are still strongly localised relative to the electrons. In contrast to the structures with higher InN content the hole states eventually reach the same scale of PR values as the electrons for the range of states studied, as shown in Fig. 5.14. This is mainly due to delocalisation along the c -axis direction, which becomes possible because of the reduced built-in polarisation potential compared to the structures containing 25% InN. Note also how the first electron state has a lower PR than the second state. This is seen consistently across all configurations and results from band folding effects due to periodicity in the c -plane. The lowest electron state has no contribution from folded bands and is relatively delocalised in the c -plane. By contrast, the second state has, due to the 2-d periodicity of the supercell, contributions from at least 4 \mathbf{k} -states. This superposition creates states with a cosine like distribution of probability density and hence, due to the increased number of lobes, these states are more localised and have a higher PR.

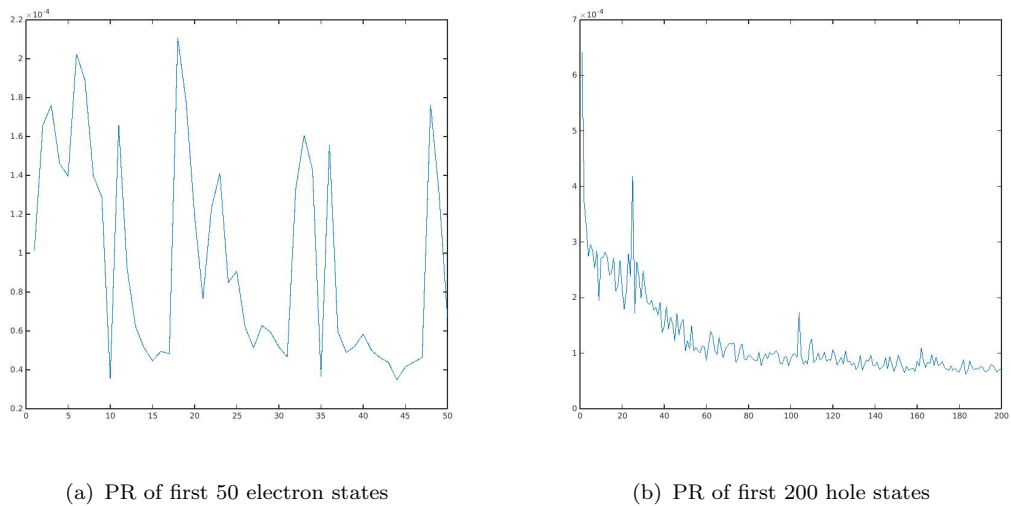


FIGURE 5.13: Participation ratio of first 50 electron and first 200 hole states.

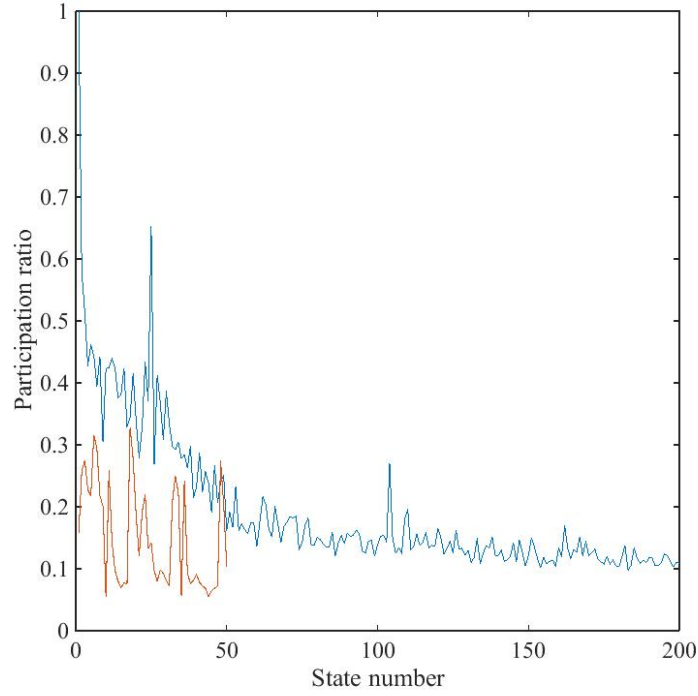
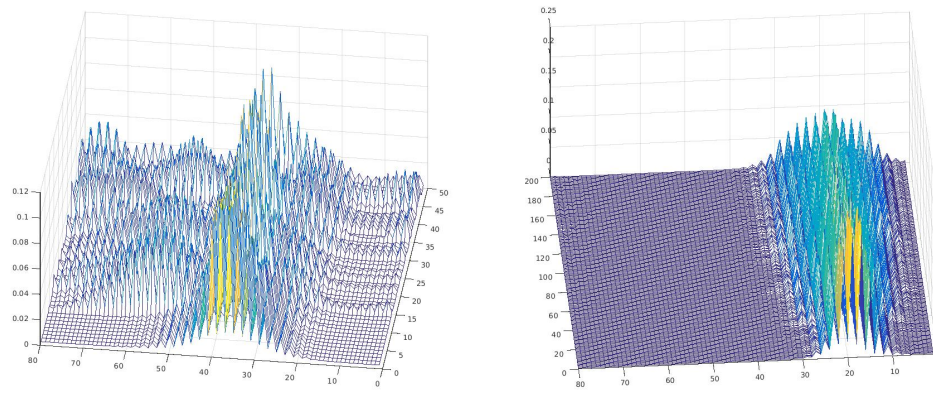


FIGURE 5.14: The PR for electron and hole states, normalised to the first hole state.

5.4.2 Probability density in a layer

When we examine the probability density of each state in each layer of the structure we see the effects of the weaker built-in polarisation potential on the localisation of the states. For the electrons the first 10 states are localised at the barrier interface but after these states we can clearly see the emergence of higher bands. These higher bands, noticeable in Fig. 5.15(a) by the increased number of nodes in the c -direction, are at energies above the GaN conduction band edge. They therefore leak heavily into the barrier and also spread across the full QW. For the hole states we notice something similar; after 40 states the holes begin to spread both across the QW and into the barrier. These first 40 states belong to the first confined band and further states with contributions from higher bands are then more delocalised along the c -axis direction. Because of the built-in potential, the electrons tend to first spread into the barrier on the left hand side while the holes leak into the right hand barrier.



(a) Electron probability density per monolayer. (b) Hole probability density per monolayer.

FIGURE 5.15: Probability density of electron and hole states in each of the 80 monolayers of the supercell.

5.4.3 Energy separation of states

We saw with the QWs with 25% InN that the first 75 electron states extended much deeper into the conduction band than the first 75 hole states extend into the valence band, as was shown in Fig. 5.3. As stated already, with these 10% wells, after ten states the GaN conduction band edge is reached. In order to examine how far into the valence band the hole states reach we calculate the first 200 hole states. The hole states again have a much smaller separation in terms of energy than the electrons and all 200 states calculated are confined in the QW. The lowest hole state calculated is still 50 meV above the GaN valence band edge.

5.4.4 Charge density overlap

The localisation properties of the states that belong to the first confined band for both electrons and holes have a noticeable effect on the charge density overlap between the states, as shown in Fig. 5.17. The ‘shelf’ seen after 10 electron states is again present but less pronounced than for the 25% case. This is due to the reduced built-in field which allows all electron and hole states to spread further into the QW than compared to the 25% QWs. This shelf is a result of the difference in the confinement along the c -axis direction of states belonging to different subbands, as seen in Fig. 5.15. A smaller but similar change is seen after 40 hole states where the states are, again, more delocalised along the c -axis direction and as a result a general increase in the charge density overlap is seen at this point. The overlap

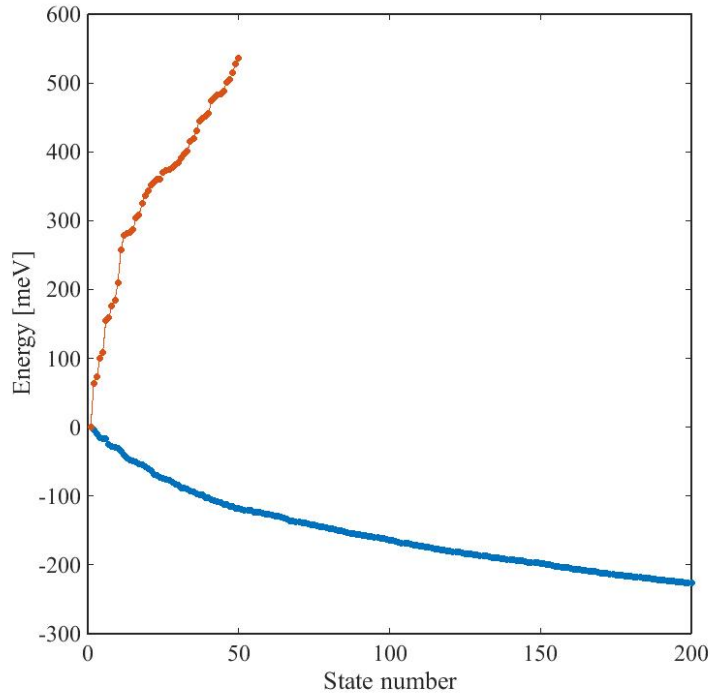


FIGURE 5.16: How the energy separation of the individual states varies for electrons (red) and holes (blue).

between the lowest 10 electron states and the hole states is larger than the 25% QWs, almost an order of magnitude bigger on average (the overlap between these states is of the order of $\approx 10^{-7}$ for the 25% QWs). This is again a result of the reduced confinement along the c -axis direction due to the weaker built-in field. A steady increase in overlap can be seen as we go to higher hole states corresponding with the increase in delocalisation along the c -axis for higher hole states seen in Fig. 5.15.

5.4.5 Hole localisation

We see in Fig. 5.18 that although there is a reduced InN content compared to the $\text{In}_{0.25}\text{Ga}_{0.75}\text{N}$ QWs, and hence less In clusters and local alloy fluctuations, the first 5 hole states are still strongly localised in the c -plane. This is to be expected as there is still a significant In content in the QWs causing local alloy fluctuations. These states fill up quickly however, and after the 10th hole state we begin to see more delocalised behaviour, as shown in Fig. 5.19. The electron states are, again, largely unaffected by the local alloy fluctuations and remain delocalised.

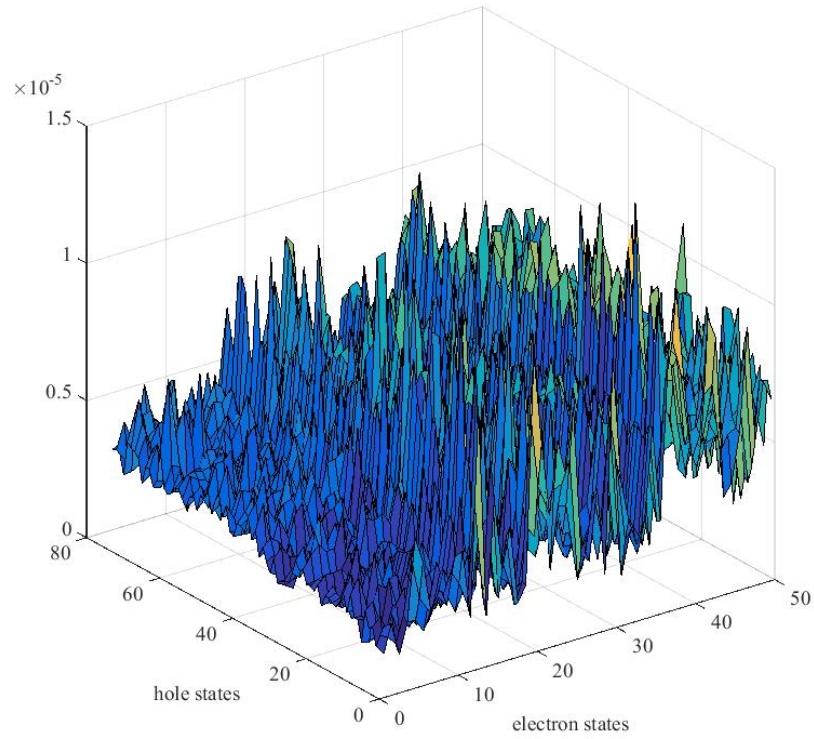
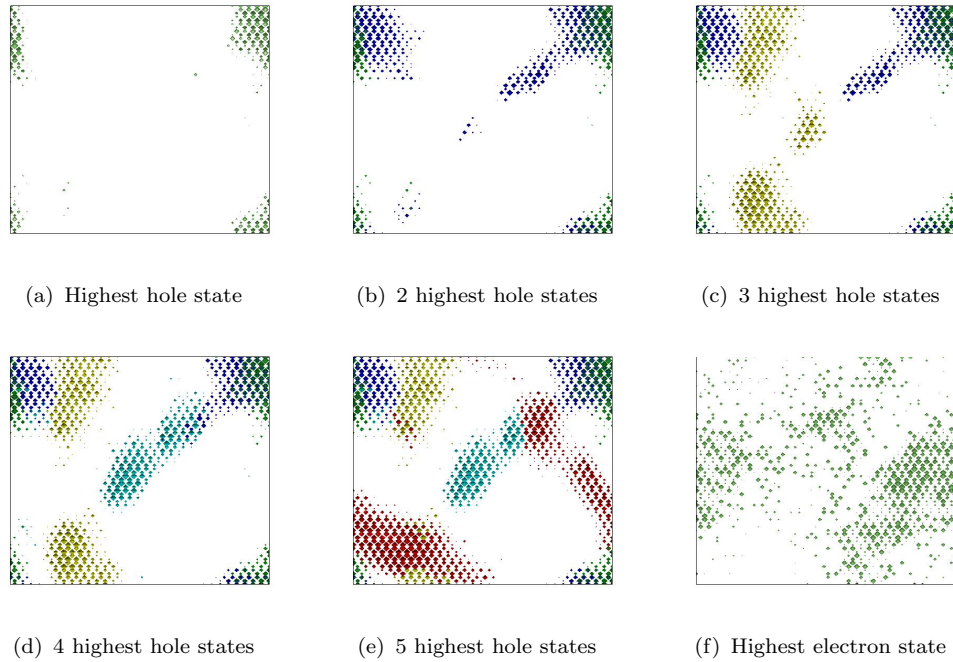
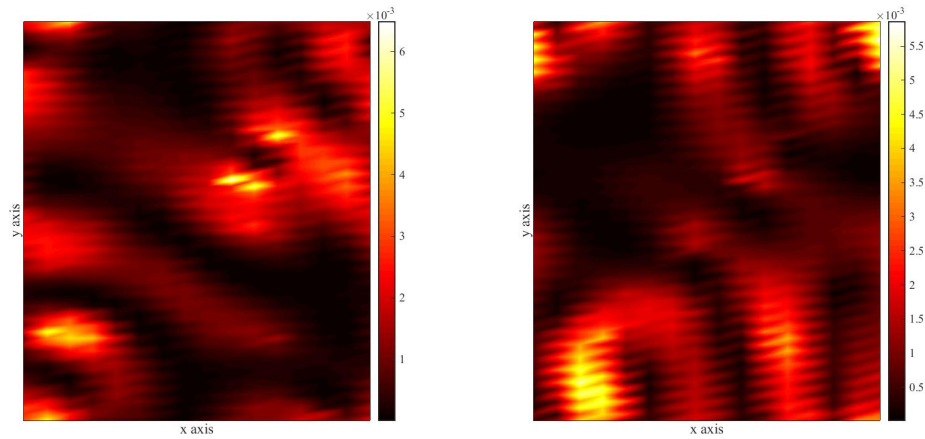


FIGURE 5.17: Charge density overlap for the first 50 electron and 75 hole states.

FIGURE 5.18: Localisation of the first five holes and first electron state projected onto the c plane.

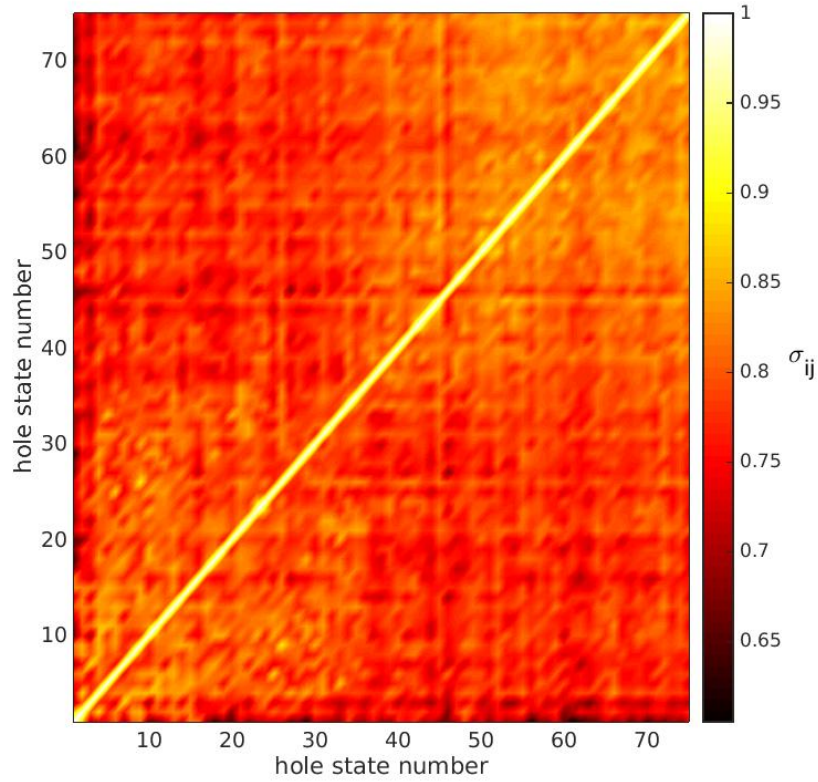
(a) c -plane projection of the 14th hole state.(b) c -plane projection of the 15th hole state.FIGURE 5.19: The c -plane projection of the 14th and 15th hole states which are delocalised.

5.4.6 Hole overlap

Shown in Fig. 5.20 is the overlap between hole states, calculated as we did in Sec. 5.2.6. The first difference between this and the 25% case is the scale, notice the colorbar goes from 0 to 1 in Fig. 5.7 whereas it starts just above 0.6 in Fig. 5.20. This shows that there is in general a much higher overlap between the hole states for the lower composition wells. This is due to reduced local alloys fluctuations as a consequence of the lower InN concentration. Whereas in the 25% case we saw a mobility edge between localised and delocalised states to occur between the 10th and 20th hole state we see a similar transition to occur after only 4 or 5 hole states in these 10% QWs. These states are 15 meV below the ground hole state compared to the range of 80 to 120 meV for the 25% case. We see two areas of higher overlap within this region, both correspond to different subbands. As we showed in Fig. 5.15, the different subbands have different localisation characteristics along the c -axis and as a result states in the same subband will have slightly higher overlap than those from different subbands.

5.4.7 Summary of $\text{In}_{0.10}\text{Ga}_{0.90}\text{N}$ flat QWs.

The decrease in InN content in these QWs has a strong influence on the localization properties of these structures. Both the electron and hole states are spread much deeper into the QW due to the decreased built-in potential. The highest hole

FIGURE 5.20: σ for the first 200 hole states.

states are still localised in the c -plane, but the effect is weaker than in the 25% structures and lower hole states are delocalised throughout the c -plane. This is a result of less alloy fluctuation and clustering effects due to the reduced InN content.

5.5 $\text{In}_{0.10}\text{Ga}_{0.90}\text{N}$ quantum wells with well width fluctuations

The final set of QWs we examined were $\text{In}_{0.1}\text{Ga}_{0.9}\text{N}$ with WWFs. Similar to the comparison between flat QWs and the ones with WWFs for 25% InN content, the QWs with WWFs mirror the behaviour of the flat ones for this composition too. In contrast to the 25% case however, the WWFs do not localise the first few electrons as strongly in the c -plane in the case of these lower composition QWs. Again the PR and probability density in each monolayer are nearly identical to the flat QWs while the charge density overlap has similar features to the flat case but the scale is

slightly reduced. Shown in Fig. 5.21 is the projection of the probability density on the c -plane for the first two electron states. We see how they are weakly localised within the WWFs compared to the 25% case, this can be seen by comparing the scales of Fig. 5.21 and Fig. 5.9. This is again due to the weaker built-in potential. The electrons are not as tightly bound in each monolayer near the interface and hence they are not pulled into the WWFs as they are in the QWs with 25% InN content.

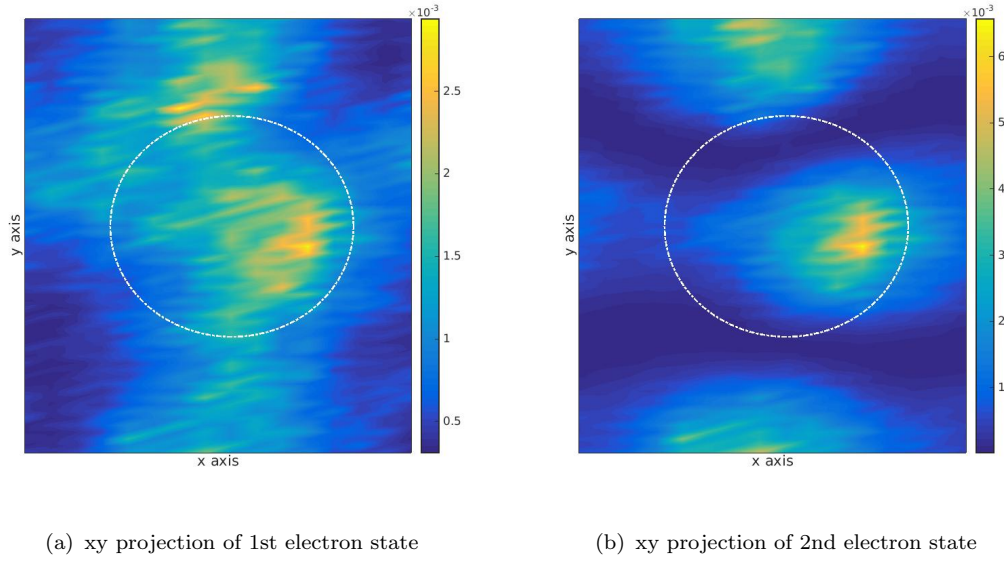


FIGURE 5.21: The first two electron states are weakly localised in the c -plane by the WWF (marked by the white circle).

The c -plane localisation of the electron states, again, reduces the charge density overlap between the electrons and holes. The same features are present in Fig. 5.22 as Fig. 5.17 (for the flat QWs); the increase in overlap after 40 hole states and the larger jump after 10 electron states. The scale, however, is reduced roughly by a factor of 20%.

We again compare the overlap between the electron ground state and the first 20 hole states for both the flat QWs and those with WWFs, as shown in Fig. 5.23. We see how the WWFs slightly reduce the overlap between these states but to a lesser extent than in the 25% QWs (Fig. 5.11).

In summary the WWFs weakly localise the electrons in the c -plane and this causes a reduction in the charge density overlap between the electrons and holes but due to the reduced built-in potential the effect of this localisation is not as strong as in the QWs with 25% InN.

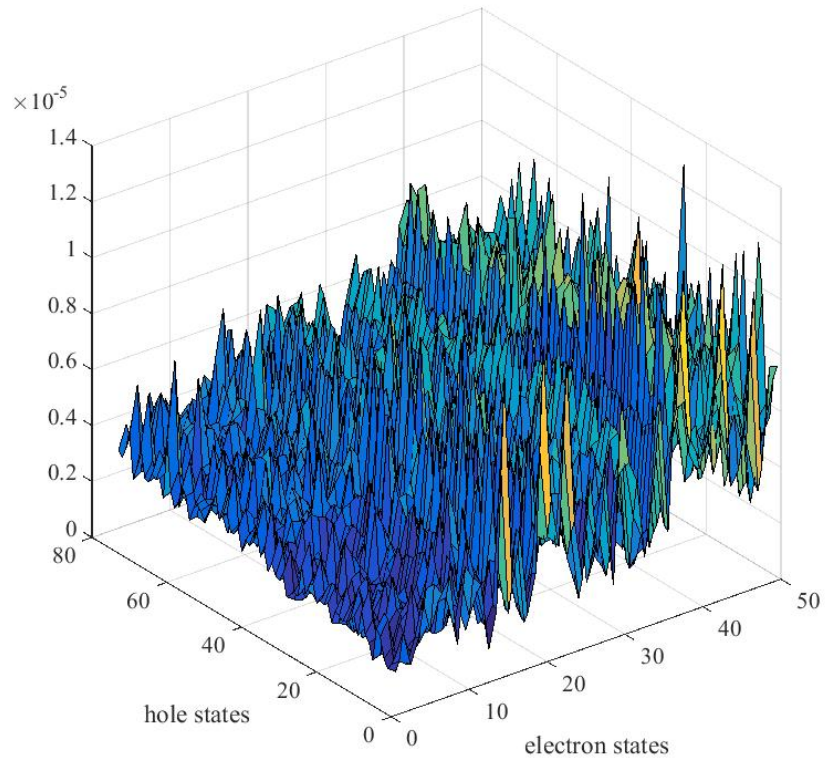


FIGURE 5.22: Charge density overlap for the first 50 electron and 75 hole states.

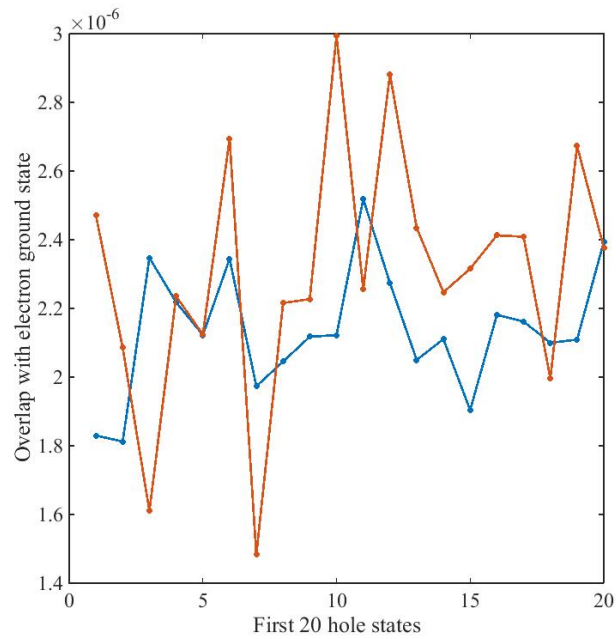


FIGURE 5.23: Charge density overlap between the electron ground state and the first 20 hole states for flat QWs (red) and QWs with WWFs (blue).

5.6 Conclusions

We examined QWs with two different compositions, $\text{In}_{0.25}\text{Ga}_{0.75}\text{N}$ and $\text{In}_{0.10}\text{Ga}_{0.90}\text{N}$, for structures with and without WWFs. The higher composition QWs with 25% InN content show strongly localised electrons and holes. The highest hole states are confined within the c -plane due to local alloy fluctuations that give rise to local strain and fluctuations in the built-in potential. The electrons are largely delocalised in the c -plane but the built-in potential confines the electrons to the upper interface of the QW. The PR of the electrons show that the first 20 electron states are strongly localised in the c -direction and higher states begin to spread into the QW. This behaviour is reflected in the charge density overlap where there is poor overlap between holes and electrons that are localised along the c -direction and improved overlap with more delocalised states. These first 20 electron states belong to the first confined band.

In the lower composition QWs, $\text{In}_{0.10}\text{Ga}_{0.90}\text{N}$, the electron and hole states are more delocalised along the c -direction due to the reduced built-in field. Then after the first confined band for both the electrons and holes the states spread more into the QW. This leads to increased overlap for these excited states but for the lower states similar behaviour to the 25% QWs is seen. The higher holes states are localised in the c -plane and the main improvement in the charge density overlap is still due to excited electron states spreading further into the QW.

The effect of the WWFs, that we modelled with 5 nm wide disk at the top of QW, was to confine the electrons in the c -plane. For the QWs with 25% InN content the built-in potential strongly localised the electrons in the monolayers near the interface and thus the first two electron states were confined within the disk. This in plane localisation further reduces the overlap with the hole states that are also strongly localised in the c -plane. A similar behaviour is seen for the $\text{In}_{0.1}\text{Ga}_{0.9}\text{N}$ QWs. The first two electron states are weakly confined by the WWFs but the lower InN content means the built-in potential is weaker and hence the electrons are not as strongly confined within the disk as they are in the case of the 25% QWs. The confinement of the electrons also decreases the overlap with the hole states but to a lesser extent than the 25% QWs.

Chapter 6

Summary, conclusions and outlook

In this thesis we have presented an atomistic description, through the tight-binding (TB) model, of the electronic properties of III-nitride semiconductor materials. As outlined in the introduction, this thesis can be divided into two distinct parts, but both are built on the foundation of the TB model. In Sec. 6.1 we give a brief summary of the thesis and present our conclusions and in Sec. 6.2 we outline possible future investigations.

6.1 Summary and Conclusions

After a general introduction and outline in chapter 1, we presented the foundations of the TB model in chapter 2. We began with a discussion of periodic crystal lattices and how we can exploit their symmetry to simplify our calculations. Then, after introducing the idea of Bloch sums we developed the TB model and showed how the Hamiltonian is constructed. The foundations of the modern theory of polarisation were presented in the second half of this chapter where we introduce the concept of the Berry Phase.

Chapter 3 dealt with our implementation of the TB model in conjunction with the modern theory of polarisation to investigate, on a microscopic scale, the piezoelectric effect and spontaneous polarisation in III-nitride semiconductors. We first presented an analytic implementation of this theory by studying a linear chain of

atoms. With a minimal basis of one s -orbital per site we showed how the Berry phase varies linearly with strain and also linearly for small values of the bond polarity α_p . This simple model helped us to build an understanding of how to implement and benchmark the numerical calculations for the full 3-dimensional structure.

With the numerical calculations we first compared ZB and ideal WZ structures. After testing the convergence of the number of \mathbf{k} points needed in the Brillouin zone we showed how the P_{spon} for ZB structures is identically zero and that for ideal WZ P_{spon} is very small but non-zero. We explained that this is due to the similarity of the first NN environment of the two crystallographic phases. We further emphasised this similarity by comparing the effective charge and PZ coefficients for the two structures and concluded that they both have a similar response to strain and sublattice displacement within our first NN TB description. We showed how the calculated values for the effective charge are consistently smaller than the experimental values published. We suggested this is due to a fundamental limitation of the TB model, in that the minimal basis set used cannot describe the full Brillouin zone, all of which is sampled in the Berry phase model. In light of this we explained why the calculated PZ coefficients for ZB do not give quantitative agreement with published values. The total polarisation, from which the PZ coefficients are calculated, is given by the difference between the electronic and ionic contributions. Both of these are large relative to their difference and so a small proportional error in the electronic component leads to a large variation in the results that depend on the total polarisation. We showed that our implementation of the TB model with the Berry phase polarisation gives a reasonable description of the electronic contribution by comparing it directly with values calculated with DFT but when combined with the ionic component we see how the model fails.

In calculating the P_{spon} for real WZ structures we demonstrated the parameter sensitivity of the model. The values calculated underestimate those published but the agreement is shown to be improved by implementing a set of larger bond length scaling exponents, fitted to match key deformation potentials. These scaling exponents were shown however to not improve the PZ coefficients, with the calculated coefficients having the wrong sign. Thus we concluded that the closer agreement to published values in terms of P_{spon} is attained not by an improved description of the eigenstates but by amplifying other factors to compensate. We again reiterate that an accurate quantitative description of the PZ coefficients is not attainable

with this model, for the same reasons of a small proportional error in the electronic polarisation being amplified by the relative size of the total polarisation. We further showed that the error in calculating PZ coefficients is even larger in the case of real WZ, partly due to the fact that the initial state in these structures is non-centrosymmetric. We showed how the electronic component as calculated with our TB model gives a good qualitative description of the ratio of the PZ coefficients $\frac{e_{33}}{e_{31}}$ by comparing it to experimental data, thus reiterating that, while this model provides a qualitative description of polarisation trends in III-nitride materials, accurate quantitative results are beyond the scope of the model.

We then employed our atomistic TB model to analyse band gap bowing and optical polarisation switching in $\text{Al}_{1-x}\text{Ga}_x\text{N}$ alloys over the full composition range. Our model included local atomistic effects from random alloy fluctuations such as local strain and built-in potential variation. We extracted a bowing parameter for the band gap of $b = 0.94$ eV, which is in good agreement with experiment. We further analysed the origin of this bowing in the conduction band (CB) and valence band (VB) edges and fitted bowing parameters to both; $b^{\text{CB}} = 0.78$ eV and $b^{\text{VB}} = -0.16$ eV. We calculated the composition at which the band edge optical emission switches between the TE and TM polarisation directions. We found the switchover to be in the region $x \approx 0.75$ which is at a much higher Al composition (25%) than would have been expected (9%) assuming a linear variation of the crystal field splitting in our calculations. This observed non-linear behavior of the crystal field splitting is consistent with recent experimental observations.

Finally, we implemented our TB model to study electron and hole localization in $\text{In}_x\text{Ga}_{1-x}\text{N}$ quantum wells (QWs). We examined two different compositions; $\text{In}_{0.10}\text{Ga}_{0.90}\text{N}$ and $\text{In}_{0.25}\text{Ga}_{0.75}\text{N}$ for structures both with and without well width fluctuations (WWFs). The QWs with the higher InN composition of 25% were found to have a strong built-in potential which confined the carriers to opposite sides of the QW. In addition to this the local alloy variations which gave rise to local strain and polarisation potential fluctuations were found to strongly localise the hole states in the c -plane. This was shown to affect the charge density overlap with the electrons, which were found to be delocalised in the c -plane. We showed that any improvement in overlap between the electrons and hole came from higher electron states that were delocalised along the c -axis direction. A mobility edge between localised and delocalised hole states was estimated to occur between the 10th and 20th hole state, at an energy in the range of 80 to 120 meV below the

hole ground state. The WWF were found to strongly localise the first two electron states while having no effect on the hole states. The charge density overlap was reduced compared to the flat QWs as a result of the WWFs.

The $\text{In}_{0.10}\text{Ga}_{0.90}\text{N}$ QWs, as a result of their lower InN composition, had a lower built-in field. This reduced built-in field allowed both the electron and hole states to extend further into the QW resulting in increased charge density overlap in general. Similar trends to the 25% case are seen in the charge density overlap where improvements in overlap are due to states, more delocalised along the c -axis, that belong to higher subbands. The first 5 to 10 hole states are, again, strongly localised in the c -plane due to local alloy fluctuations but above this the holes begin to delocalise in the c -plane. This is reflected in a mobility edge occurring near the 5th hole state for the 10% QWs, 15 meV below the hole ground state for the structures considered. The WWFs again localised the first two electron states but since the built-in field is weaker so too is the effect of this localisation.

6.2 Outlook and future work

In the case of using tight-binding wavefunctions within the Berry phase theory of modern polarisation I do not recommend any further investigations. We tried exhaustively over the first three years of my research to improve the model or extract any useful results. These attempts, most of which are not described in this thesis, included various 3-d analytic models, different Hamiltonians (in terms of size of basis, composition of basis, and orientation) and many different parameterisations both in terms of TB parameters and fitting to the phase surfaces. None of these proved fruitful. All the previously published implementations of this model had attempted to improve the model, whether through an extended basis set, using an off-diagonal position operator or exploiting the parameter sensitivity; they all failed to extract useful results on anything other than the effective charge. It is my opinion that to correctly describe the polarisation properties of III-nitride materials one needs to include not just second nearest neighbours but also third nearest neighbours to give an accurate description of the valence bands throughout the Brillouin zone. The number of parameters required coupled with the parameter sensitivity of the model make this a dangerous approach to follow however.

The obvious next step for the work outlined in chapter 4, on the band gap bowing and optical polarisation switching in $\text{Al}_{1-x}\text{Ga}_x\text{N}$ alloys is to investigate the quaternary alloy, $\text{Al}_{1-x-y}\text{Ga}_x\text{In}_y\text{N}$. In order to investigate the influence of local atomistic variations on the band gap evolution with composition of $\text{Al}_{1-x-y}\text{Ga}_x\text{In}_y\text{N}$, one must first calculate the bowing parameters of the three ternary alloys. All of these have been investigated with the same models within our group, $\text{Al}_{1-x}\text{Ga}_x\text{N}$ was the last one left, and we are now in a good position to investigate how local alloy fluctuations affect the electronic properties of $\text{Al}_{1-x-y}\text{Ga}_x\text{In}_y\text{N}$.

Finally, in the case of the $\text{In}_x\text{Ga}_{1-x}\text{N}$ quantum wells there remains more work to be done. The intermediate composition of 15% InN is the next obvious candidate to examine the evolution of the effect of InN composition on the built-in field and local alloy fluctuations, and how these affect the localisation of the carriers, particularly the hole states. The important factors to investigate would be how many of the highest hole states are localised in the c -plane and how localised are both the electron and hole states along the c -axis direction due to the built-in field. Lower compositions below 10% would also be of interest, possibly 5% or 8% InN content, to see at what composition do the first five hole states become delocalised in the c -plane. Further work would also be of interest to investigate carrier localisation effects in non-polar (and semipolar) QW structures, where there are no (or reduced) built-in fields, but where local alloy fluctuations would still be expected to have a strong influence on hole localisation near the valence band maximum of the the QW structures.

Appendix A

Material parameters

In this appendix we present the material parameters for the III-nitrides that we implemented throughout this thesis.

A.1 Material parameters used in tight-binding calculations

A.1.1 Tight-binding paramaters

	GaN	InN	AlN
$\epsilon(s,a)$	-10.6158	-11.9173	-10.2006
$\epsilon(p,a)$	0.8183	0.4886	0.6637
$\epsilon(s,c)$	0.9122	0.4837	2.2474
$\epsilon(p,c)$	6.6788	6.5322	11.0763
$V_{ss\sigma}$	-1.4937	-0.4031	-2.0285
$V_{s(a)p(c)\sigma}$	1.7714	0.8192	1.3182
$V_{s(c)p(a)\sigma}$	3.7523	2.6567	4.4648
$V_{pp\sigma}$	3.3194	2.8635	3.6159
$V_{pp\pi}$	-0.7829	-0.7619	-0.6085

TABLE A.1: The tight-binding parameters implement for the III-nitrides.

A.1.2 Internal displacement parameters

	GaN	InN	AlN
ζ_1	0.156	0.193	0.138
ζ_2	0.083	0.107	0.086
ζ_3	0.159	0.218	0.191
ζ_4	0.201	0.337	0.199
ζ_5	0.141	0.107	0.143

TABLE A.2: The internal displacement parameters implement for the III-nitrides in chapter 3.

A.1.3 Bond length scaling parameters

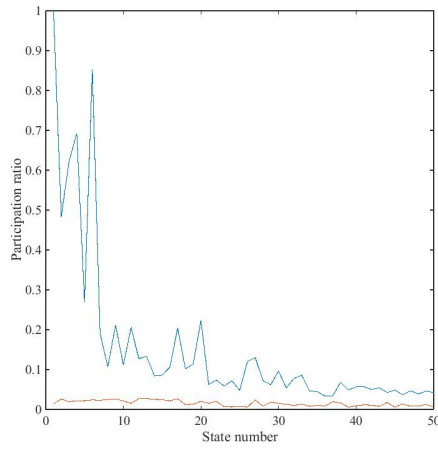
$\eta_{\alpha\beta}$	GaN	InN	AlN
ss_σ	3.6	3.4	4.5
$s(a)p(c)_\sigma$	8.7	8.7	8.7
$s(c)p(a)_\sigma$	8.7	8.7	8.7
pp_σ	0.94	0.94	0.94
pp_π	3.25	4.74	5.72

TABLE A.3: The bond length scaling parameters derived by Andy Lindsay and implemented for the III-nitrides in chapter 3.

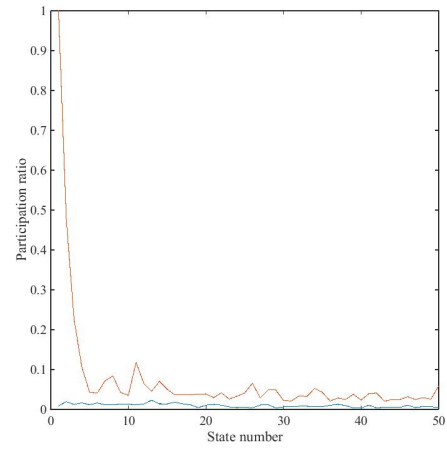
Appendix B

InGaN quantum wells, additional configurations.

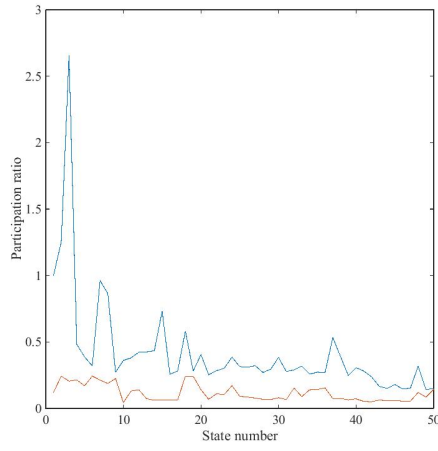
Here we present some of the additional configurations of the $\text{In}_x\text{Ga}_{1-x}\text{N}$ quantum wells examined in chapter 5. For six different configurations we present the participation ratio, charge density overlap, energy separation of states, hole state overlap as well as the probability density in each monolayer for both electrons and holes. Configurations A and B are 25% flat QWs, configurations C and D are 10% flat QWs and configurations E and F are 10% QWs with well width fluctuations.



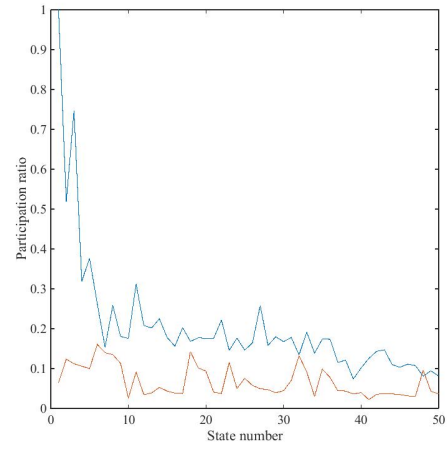
(a) Config. A



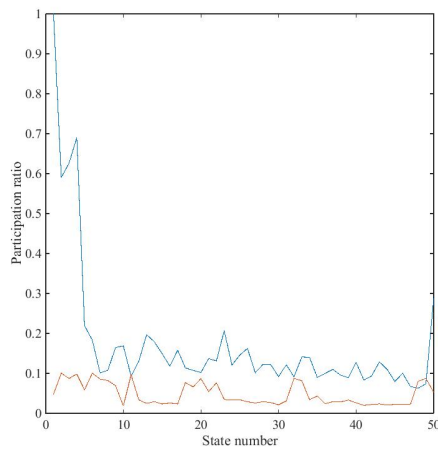
(b) Config. B



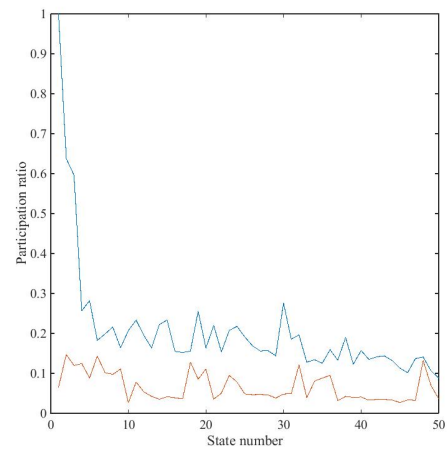
(c) Config. C



(d) Config. D

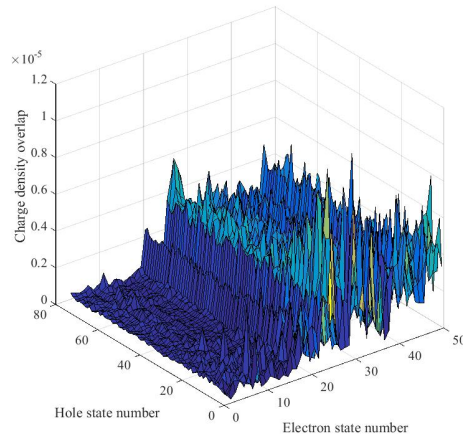


(e) Config. E

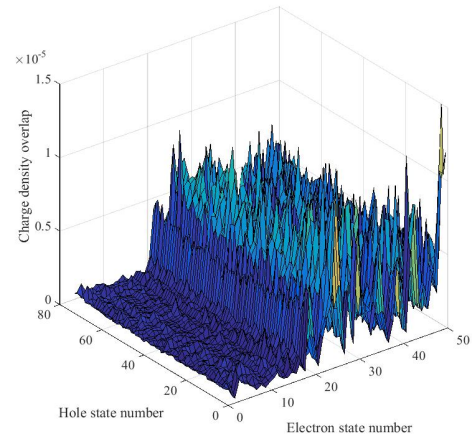


(f) Config. F

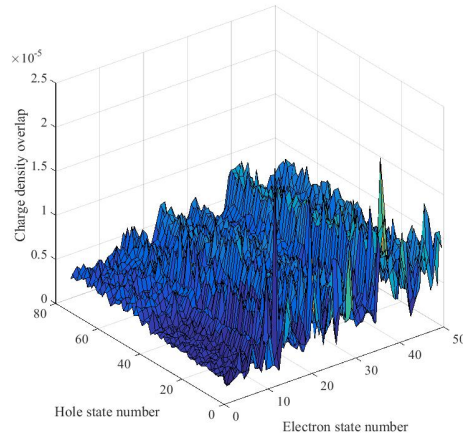
FIGURE B.1: The Participation ratio, normalised to the first hole state.



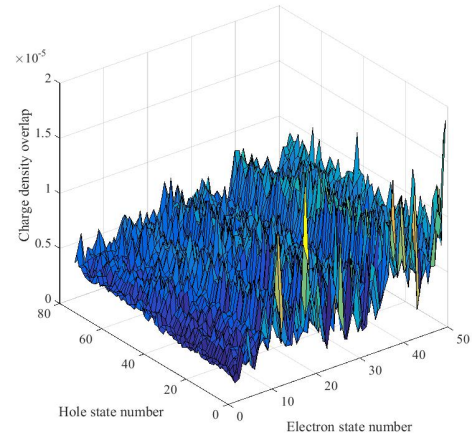
(a) Config. A



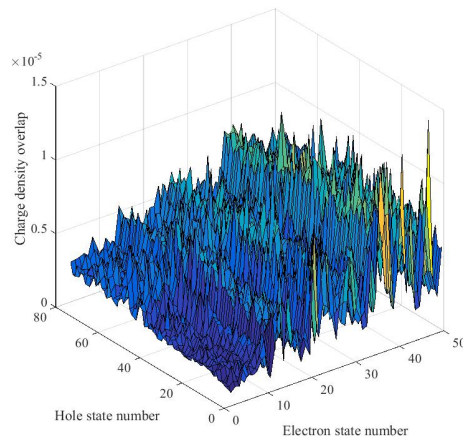
(b) Config. B



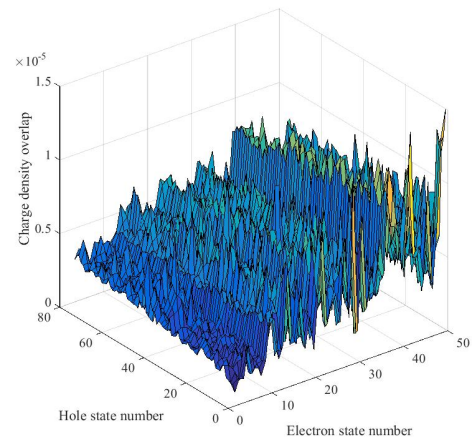
(c) Config. C



(d) Config. D

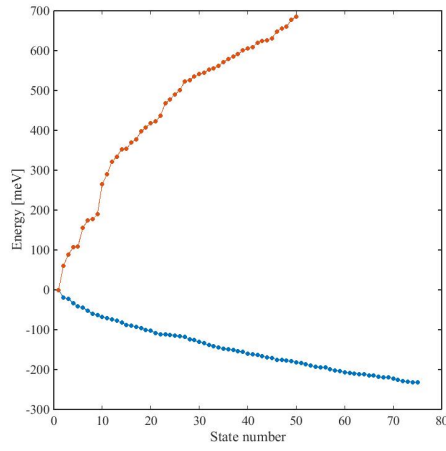


(e) Config. E

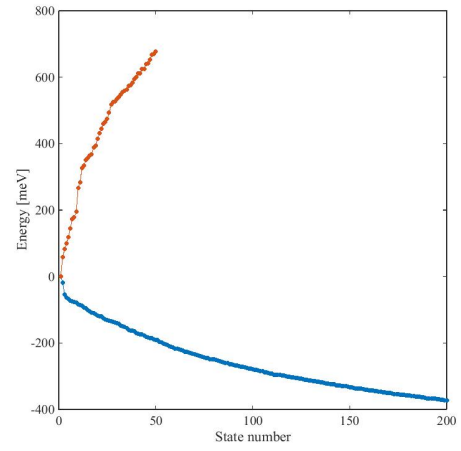


(f) Config. F

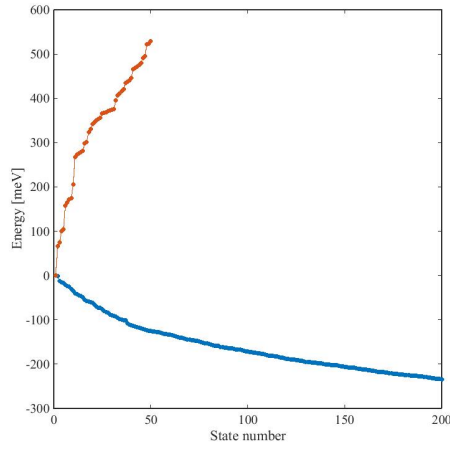
FIGURE B.2: The charge density overlap.



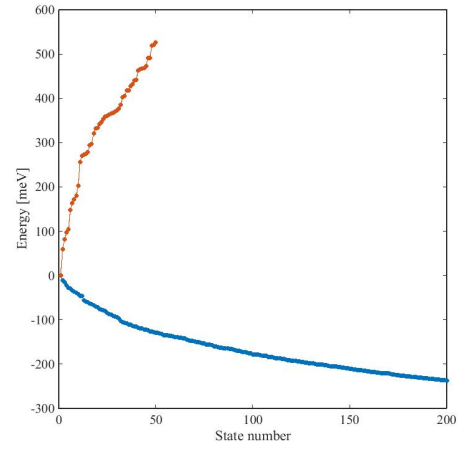
(a) Config. A



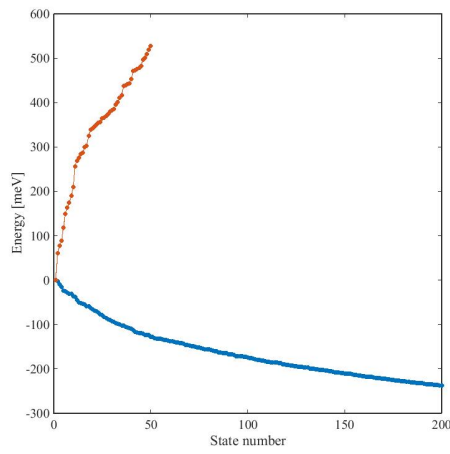
(b) Config. B



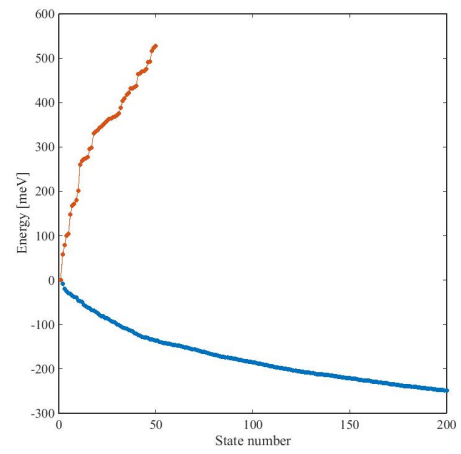
(c) Config. C



(d) Config. D



(e) Config. E



(f) Config. F

FIGURE B.3: The energy separation between the states.

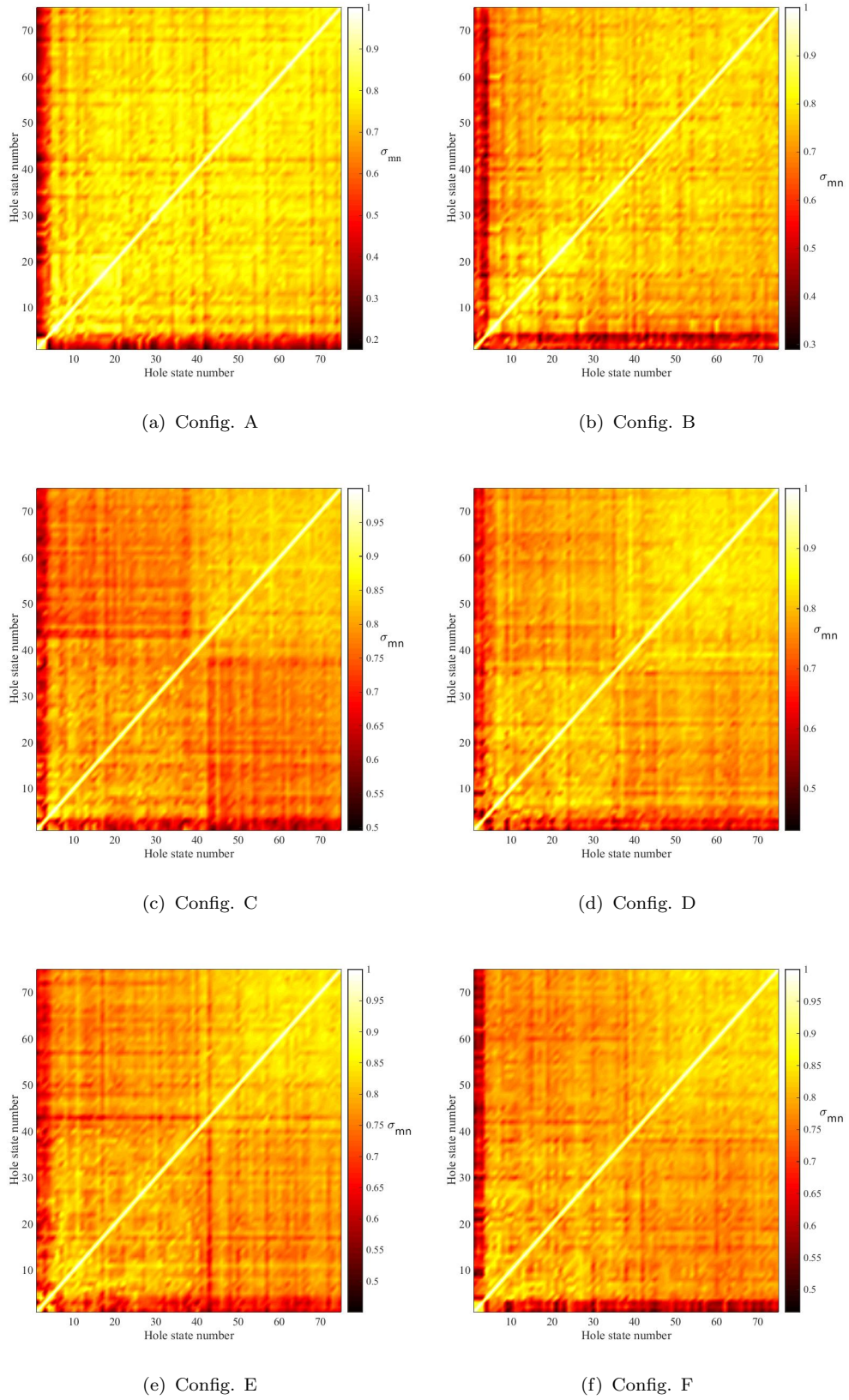


FIGURE B.4: The overlap between the hole states.

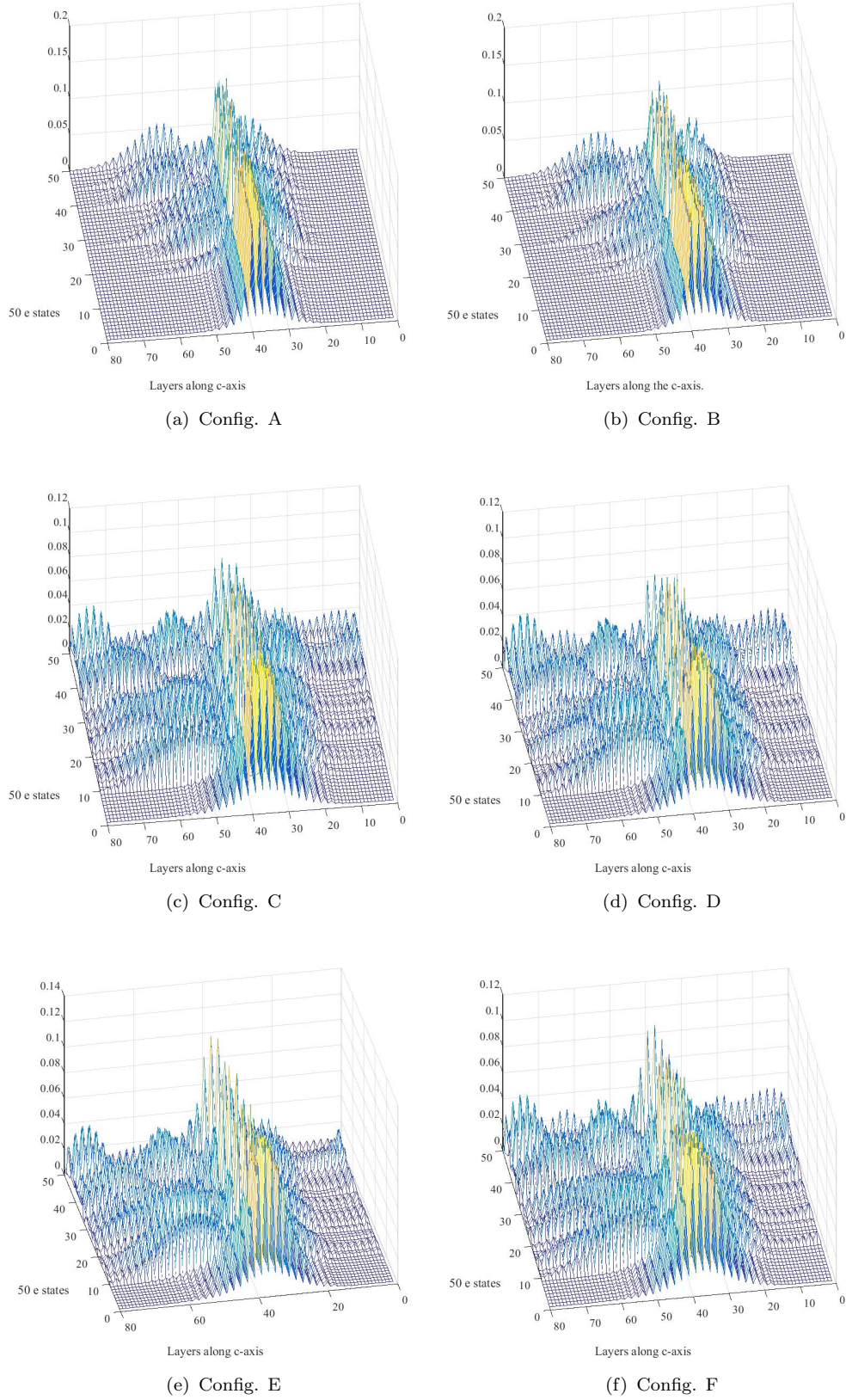


FIGURE B.5: The electron probability density in each monolayer.

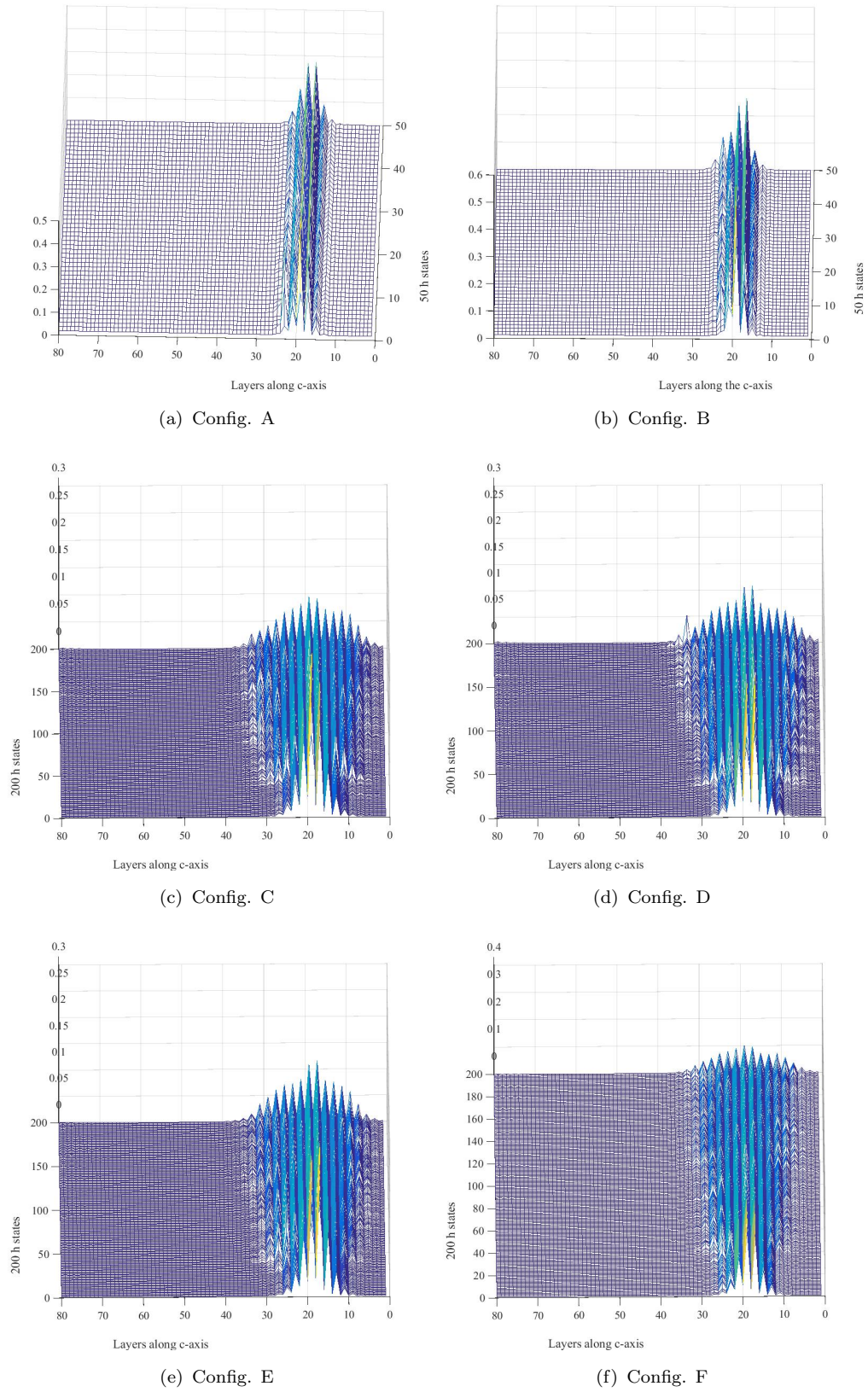


FIGURE B.6: The electron probability density in each monolayer.

Bibliography

- [1] M. A. Khan, M. Shatalov, H. Maruska, H. Wang, and E. Kuokstis, “Iii–nitride uv devices,” *Japanese journal of applied physics* **44**, 7191 (2005).
- [2] Y. Taniyasu, M. Kasu, and T. Makimoto, “An aluminium nitride light-emitting diode with a wavelength of 210 nanometres,” *Nature* **441**, 325 (2006).
- [3] S. Nakamura, “The roles of structural imperfections in ingan-based blue light-emitting diodes and laser diodes,” *Science* **281**, 956 (1998).
- [4] R. Oliver, S. Bennett, T. Zhu, D. Beesley, M. Kappers, D. Saxey, A. Cerezo, and C. Humphreys, “Microstructural origins of localization in ingan quantum wells,” *Journal of Physics D: Applied Physics* **43**, 354003 (2010).
- [5] J. C. Slater and G. F. Koster, “Simplified lcao method for the periodic potential problem,” *Physical Review* **94**, 1498 (1954).
- [6] J.-M. Jancu, R. Scholz, F. Beltram, and F. Bassani, “Empirical spds* tight-binding calculation for cubic semiconductors: General method and material parameters,” *Physical Review B* **57**, 6493 (1998).
- [7] T. B. Boykin, G. Klimeck, R. C. Bowen, and F. Oyafuso, “Diagonal parameter shifts due to nearest-neighbor displacements in empirical tight-binding theory,” *Physical Review B* **66**, 125207 (2002).
- [8] W. A. Harrison, “Electronic structure and the properties of solids: the physics of the chemical bond” (Courier Dover Publications, 2012).
- [9] M. Born and V. Fock, “Beweis des adiabatenatzes,” *Zeitschrift für Physik* **51**, 165 (1928).
- [10] D. J. Griffiths, “Introduction to quantum mechanics” (Pearson Education India, 2005).

- [11] A. A. Pinto, M. Nemes, J. P. de Faria, and M. Thomaz, “Comment on the adiabatic condition,” *American Journal of Physics* **68**, 955 (2000).
- [12] S. Pancharatnam, in “Proceedings of the Indian Academy of Sciences, Section A” (Indian Academy of Sciences, 1956), vol. 44, pp. 247–262.
- [13] M. V. Berry, “Quantal phase factors accompanying adiabatic changes,” *Proceedings of the Royal Society of London. A. Mathematical and Physical Sciences* **392**, 45 (1984).
- [14] R. W. Batterman, “Falling cats, parallel parking, and polarized light,” *Studies in History and Philosophy of Science Part B: Studies in History and Philosophy of Modern Physics* **34**, 527 (2003).
- [15] J. Hannay, “Angle variable holonomy in adiabatic excursion of an integrable hamiltonian,” *Journal of Physics A: Mathematical and General* **18**, 221 (1985).
- [16] C. A. Mead and D. G. Truhlar, “On the determination of born–oppenheimer nuclear motion wave functions including complications due to conical intersections and identical nuclei,” *The Journal of Chemical Physics* **70**, 2284 (1979).
- [17] R. Simon and N. Mukunda, “Bargmann invariant and the geometry of the güoy effect,” *Phys. Rev. Lett.* **70**, 880 (1993), URL <http://link.aps.org/doi/10.1103/PhysRevLett.70.880>.
- [18] Y. Aharonov and D. Bohm, “Significance of electromagnetic potentials in the quantum theory,” *Physical Review* **115**, 485 (1959).
- [19] R. Englman, “The Jahn-Teller effect in molecules and crystals” (Wiley-Interscience New York, 1972).
- [20] Y. Zhang, Y.-W. Tan, H. L. Stormer, and P. Kim, “Experimental observation of the quantum hall effect and berry’s phase in graphene,” *Nature* **438**, 201 (2005).
- [21] F. Wilczek and A. Zee, “Appearance of gauge structure in simple dynamical systems,” *Physical Review Letters* **52**, 2111 (1984).
- [22] J. Zak, “Berrys phase for energy bands in solids,” *Physical review letters* **62**, 2747 (1989).

- [23] R. Resta, “Macroscopic polarization in crystalline dielectrics: the geometric phase approach,” *Rev. Mod. Phys.* **66**, 899 (1994), URL <http://link.aps.org/doi/10.1103/RevModPhys.66.899>.
- [24] R. King-Smith and D. Vanderbilt, “Theory of polarization of crystalline solids,” *Physical Review B* **47**, 1651 (1993).
- [25] J. Bennetto and D. Vanderbilt, “Semiconductor effective charges from tight-binding theory,” *Physical Review B* **53**, 15417 (1996).
- [26] M. Di Ventra and P. Fernández, “Semiconductor effective charges and dielectric constants in the tight-binding approach,” *Physical Review B* **56**, R12698 (1997).
- [27] U. Iessi, C. Parisi, M. Bernasconi, and L. Miglio, “Role of tight-binding parameters and scaling laws on effective charges in semiconductors,” *Physical Review B* **61**, 4667 (2000).
- [28] J. Nye, “Physical properties of crystals: their representation by tensors and matrices.” (Oxford: Oxford University Press, 1985).
- [29] F. Bernardini, V. Fiorentini, and D. Vanderbilt, “Spontaneous polarization and piezoelectric constants of iii-v nitrides,” *Phys. Rev. B* **56**, R10024 (1997), URL <http://link.aps.org/doi/10.1103/PhysRevB.56.R10024>.
- [30] M. A. Caro, S. Schulz, and E. P. O'Reilly, “Theory of local electric polarization and its relation to internal strain: Impact on polarization potential and electronic properties of group-iii nitrides,” *Physical Review B* **88**, 214103 (2013).
- [31] C. Priester, G. Allan, and M. Lannoo, “Band-edge deformation potentials in a tight-binding framework,” *Physical Review B* **37**, 8519 (1988).
- [32] S. Schulz, M. A. Caro, L.-T. Tan, P. J. Parbrook, R. W. Martin, and E. P. O'Reilly, “Composition-dependent band gap and band-edge bowing in alinn: A combined theoretical and experimental study,” *Applied Physics Express* **6**, 121001 (2013).
- [33] W. G. Cady, “Piezoelectricity” (McGraw-Hill, 1946).

- [34] S. Schulz, M. Caro, E. O'Reilly, and O. Marquardt, "Symmetry-adapted calculations of strain and polarization fields in (111)-oriented zinc-blende quantum dots," *Physical Review B* **84**, 125312 (2011).
- [35] M. Caro, S. Schulz, and E. O'Reilly, "Hybrid functional study of the elastic and structural properties of wurtzite and zinc-blende group-iii nitrides," *Phys. Rev. B* **86**, 014117 (2012), URL <http://link.aps.org/doi/10.1103/PhysRevB.86.014117>.
- [36] M. A. Caro, S. Schulz, and E. P. O'Reilly, "Origin of non-linear piezoelectricity in III-V semiconductors: internal strain and bond ionicity from hybrid-functional density functional theory," Submitted to *Physical Review B* -, (2014).
- [37] E. O'Reilly, A. Lindsay, S. Tomić, and M. Kamal-Saadi, "Tight-binding and $k \cdot p$ models for the electronic structure of Ga(In)N and related alloys," *Semiconductor Science and Technology* **17**, 870 (2002).
- [38] G. Kresse, "Software vasp, vienna, 1999; g. kresse, j. furthmüller," *Phys. Rev. B* **54** (1996).
- [39] C. J. Humphreys, "Solid-state lighting," *MRS Bulletin* **33**, 459 (2008), ISSN 1938-1425, URL http://journals.cambridge.org/article_S0883769400005030.
- [40] R. R. Pelá, C. Caetano, M. Marques, L. G. Ferreira, J. Furthmüller, and L. K. Teles, "Accurate band gaps of AlGaIn, InGaIn, and AlInN alloys calculations based on LDA-1/2 approach," *Applied Physics Letters* **98**, 151907 (2011), URL <http://scitation.aip.org/content/aip/journal/apl/98/15/10.1063/1.3576570>.
- [41] I. Vurgaftman and J. R. Meyer, "Band parameters for nitrogen-containing semiconductors," *Journal of Applied Physics* **94**, 3675 (2003), URL <http://scitation.aip.org/content/aip/journal/jap/94/6/10.1063/1.1600519>.
- [42] I. Gorczyca, T. Suski, N. E. Christensen, and A. Svane, "Band gap bowing in quaternary nitride semiconducting alloys," *Applied Physics Letters* **98**, 241905 (2011), URL <http://scitation.aip.org/content/aip/journal/apl/98/24/10.1063/1.3597795>.

- [43] Y. Oussaifi, A. Said, A. B. Fredj, L. Debbichi, D. Ceresoli, and M. Said, “Effect of pressure on the energy band gaps of wurtzite gan and aln and electronic properties of their ternary alloys alxga1xn,” *Physica B: Condensed Matter* **407**, 3604 (2012), ISSN 0921-4526, URL <http://www.sciencedirect.com/science/article/pii/S0921452612004991>.
- [44] Z. Dridi, B. Bouhafs, and P. Ruterana, “First-principles investigation of lattice constants and bowing parameters in wurtzite alxga1-xn, inxga1-xn and inxal1-xn alloys,” *Semiconductor Science and Technology* **18**, 850 (2003).
- [45] V. N. Jmerik, E. V. Lutsenko, and S. V. Ivanov, “Plasma-assisted molecular beam epitaxy of algan heterostructures for deep-ultraviolet optically pumped lasers,” *physica status solidi (a)* **210**, 439 (2013), ISSN 1862-6319, URL <http://dx.doi.org/10.1002/pssa.201300006>.
- [46] C. Buchheim, R. Goldhahn, M. Rakel, C. Cobet, N. Esser, U. Rossow, D. Fuhrmann, and A. Hangleiter, “Dielectric function and critical points of the band structure for algan alloys,” *physica status solidi (b)* **242**, 2610 (2005), ISSN 1521-3951, URL <http://dx.doi.org/10.1002/pssb.200541265>.
- [47] B. Neuschl, J. Helbing, M. Knab, H. Lauer, M. Madel, K. Thonke, T. Meisch, K. Forghani, F. Scholz, and M. Feneberg, “Composition dependent valence band order in c-oriented wurtzite algan layers,” *Journal of Applied Physics* **116**, 113506 (2014).
- [48] S. F. Chichibu, A. Uedono, T. Onuma, B. A. Haskell, A. Chakraborty, T. Koyama, P. T. Fini, S. Keller, S. P. DenBaars, J. S. Speck, et al., “Origin of defect-insensitive emission probability in in-containing (al, in, ga) n alloy semiconductors,” *Nature materials* **5**, 810 (2006).
- [49] K. Wang, R. W. Martin, D. Amabile, P. R. Edwards, S. Hernandez, E. Nogales, K. P. ODonnell, K. Lorenz, E. Alves, V. Matias, et al., “Optical energies of alinn epilayers,” *Journal of Applied Physics* **103**, 073510 (2008), URL <http://scitation.aip.org/content/aip/journal/jap/103/7/10.1063/1.2898533>.

- [50] P. G. Moses, M. Miao, Q. Yan, and C. G. Van de Walle, “Hybrid functional investigations of band gaps and band alignments for aln, gan, inn, and ingan,” *The Journal of chemical physics* **134**, 084703 (2011).
- [51] H. Kawanishi, M. Senuma, M. Yamamoto, E. Niikura, and T. Nukui, “Extremely weak surface emission from (0001) c-plane algan multiple quantum well structure in deep-ultraviolet spectral region,” *Applied Physics Letters* **89**, 081121 (2006).
- [52] A. Atsushi Yamaguchi, “Valence band engineering for remarkable enhancement of surface emission in algan deep-ultraviolet light emitting diodes,” *physica status solidi (c)* **5**, 2364 (2008).
- [53] K. Nam, J. Li, M. Nakarmi, J. Lin, and H. Jiang, “Unique optical properties of algan alloys and related ultraviolet emitters,” *Applied physics letters* **84**, 5264 (2004).
- [54] Y. Taniyasu, M. Kasu, and T. Makimoto, “Radiation and polarization properties of free-exciton emission from aln (0001) surface,” *Applied physics letters* **90**, 261911 (2007).
- [55] M. Musgrave and J. Pople, “A general valence force field for diamond,” *Proceedings of the Royal Society of London. Series A. Mathematical and Physical Sciences* **268**, 474 (1962).
- [56] P. Keating, “Effect of invariance requirements on the elastic strain energy of crystals with application to the diamond structure,” *Physical Review* **145**, 637 (1966).
- [57] R. M. Martin, “Elastic properties of zns structure semiconductors,” *Physical Review B* **1**, 4005 (1970).
- [58] J. D. Gale and A. L. Rohl, “The general utility lattice program (gulp),” *Molecular Simulation* **29**, 291 (2003).
- [59] C. Pryor, J. Kim, L. Wang, A. Williamson, and A. Zunger, “Comparison of two methods for describing the strain profiles in quantum dots,” *Journal of Applied Physics* **83**, 2548 (1998).
- [60] R. Santoprete, B. Koiller, R. B. Capaz, P. Kratzer, Q. K. K. Liu, and M. Scheffler, “Tight-binding study of the influence of the strain on the

- electronic properties of inas/gaas quantum dots,” *Phys. Rev. B* **68**, 235311 (2003), URL <http://link.aps.org/doi/10.1103/PhysRevB.68.235311>.
- [61] M. Zieliński, “Valence band offset, strain and shape effects on confined states in self-assembled inas/inp and inas/gaas quantum dots,” *Journal of Physics: Condensed Matter* **25**, 465301 (2013).
- [62] T. B. Boykin, N. Kharche, G. Klimeck, and M. Korkusinski, “Approximate bandstructures of semiconductor alloys from tight-binding supercell calculations,” *Journal of Physics: Condensed Matter* **19**, 036203 (2007).
- [63] M. Winkelnkemper, A. Schliwa, and D. Bimberg, “Interrelation of structural and electronic properties in $\text{in}_x\text{ga}_{1-x}\text{NGaN}$ quantum dots using an eight-band **kp** model,” *Phys. Rev. B* **74**, 155322 (2006), URL <http://link.aps.org/doi/10.1103/PhysRevB.74.155322>.
- [64] S. Schulz, T. J. Badcock, M. A. Moram, P. Dawson, M. J. Kappers, C. J. Humphreys, and E. P. O’Reilly, “Electronic and optical properties of non-polar *a*-plane gan quantum wells,” *Phys. Rev. B* **82**, 125318 (2010), URL <http://link.aps.org/doi/10.1103/PhysRevB.82.125318>.
- [65] Q. Yan, P. Rinke, M. Scheffler, and C. G. Van de Walle, “Strain effects in group-iii nitrides: Deformation potentials for aln, gan, and inn,” *Applied Physics Letters* **95**, 121111 (2009), URL <http://scitation.aip.org/content/aip/journal/apl/95/12/10.1063/1.3236533>.
- [66] V. Ranjan, G. Allan, C. Priester, and C. Delerue, “Self-consistent calculations of the optical properties of gan quantum dots,” *Physical Review B* **68**, 115305 (2003).
- [67] T. Saito and Y. Arakawa, “Electronic structure of piezoelectric $\text{in}_{0.2}\text{ga}_{0.8}\text{n}$ quantum dots in gan calculated using a tight-binding method,” *Physica E: Low-dimensional Systems and Nanostructures* **15**, 169 (2002), ISSN 1386-9477, URL <http://www.sciencedirect.com/science/article/pii/S1386947702005155>.
- [68] M. Zielinski, W. Jaskólski, J. Aizpurua, and G. W. Bryant, “Strain and spin-orbit effects in self-assembled quantum dots,” *ACTA PHYSICA POLONICA SERIES A* **108**, 929 (2006).

- [69] K. Schuh, S. Barthel, O. Marquardt, T. Hickel, J. Neugebauer, G. Czycholl, and F. Jahnke, “Strong dipole coupling in nonpolar nitride quantum dots due to coulomb effects,” *Applied Physics Letters* **100**, 092103 (2012), URL <http://scitation.aip.org/content/aip/journal/apl/100/9/10.1063/1.3688900>.
- [70] C. J. Humphreys, “Does in form in-rich clusters in ingan quantum wells?,” *Philosophical Magazine* **87**, 1971 (2007).
- [71] M. J. Galtrey, R. A. Oliver, M. J. Kappers, C. J. Humphreys, D. J. Stokes, P. H. Clifton, and A. Cerezo, “Three-dimensional atom probe studies of an $\text{In}_{0.5}\text{Ga}_{0.5}\text{In}_{0.5}\text{Ga}_{0.5}$ multiple quantum well structure: Assessment of possible indium clustering,” *Applied Physics Letters* **90**, 061903 (2007), URL <http://scitation.aip.org/content/aip/journal/apl/90/6/10.1063/1.2431573>.
- [72] F. Yun, M. A. Reshchikov, L. He, T. King, H. Morkoç, S. W. Novak, and L. Wei, “Energy band bowing parameter in $\text{Al}_{0.5}\text{Ga}_{0.5}\text{In}_{0.5}\text{Ga}_{0.5}$ alloys,” *Journal of applied physics* **92**, 4837 (2002).
- [73] A. Rizzi, M. Kocan, J. Malindretos, A. Schildknecht, N. Teofilov, K. Thonke, and R. Sauer, “Surface and interface electronic properties of $\text{Al}_{0.5}\text{Ga}_{0.5}\text{In}_{0.5}\text{Ga}_{0.5}$ epitaxial layers,” *Applied Physics A* **87**, 505 (2007).
- [74] D. Brunner, H. Angerer, E. Bustarret, F. Freudenberger, R. Hopler, R. Dimitrov, O. Ambacher, and M. Stutzmann, “Optical constants of epitaxial $\text{Al}_{0.5}\text{Ga}_{0.5}\text{In}_{0.5}\text{Ga}_{0.5}$ films and their temperature dependence,” *Journal of applied physics* **82**, 5090 (1997).
- [75] S. Schulz, M. A. Caro, and E. P. O’Reilly, “Impact of cation-based localized electronic states on the conduction and valence band structure of $\text{Al}_{0.5}\text{In}_{0.5}\text{In}_{0.5}\text{In}_{0.5}$ alloys,” *Applied Physics Letters* **104**, 172102 (2014), URL <http://scitation.aip.org/content/aip/journal/apl/104/17/10.1063/1.4872317>.
- [76] N. Binggeli, P. Ferrara, and A. Baldereschi, “Band-offset trends in nitride heterojunctions,” *Phys. Rev. B* **63**, 245306 (2001), URL <http://link.aps.org/doi/10.1103/PhysRevB.63.245306>.

- [77] G. Martin, A. Botchkarev, A. Rockett, and H. Morkoc, “Valence-band discontinuities of wurtzite gan, aln, and inn heterojunctions measured by x-ray photoemission spectroscopy,” *Applied Physics Letters* **68**, 2541 (1996).
- [78] W. Mönch, “Empirical tightbinding calculation of the branchpoint energy of the continuum of interfaceinduced gap states,” *Journal of Applied Physics* **80**, 5076 (1996), URL <http://scitation.aip.org/content/aip/journal/jap/80/9/10.1063/1.363486>.
- [79] E. Sakalauskas, B. Reuters, L. R. Khoshroo, H. Kalisch, M. Heuken, A. Vescan, M. Röppischer, C. Cobet, G. Gobsch, and R. Goldhahn, “Dielectric function and optical properties of quaternary alingan alloys,” *Journal of Applied Physics* **110**, 013102 (2011).
- [80] Q. Yan, P. Rinke, M. Winkelnkemper, A. Qteish, D. Bimberg, M. Scheffler, and C. G. Van de Walle, “Band parameters and strain effects in zno and group-iii nitrides,” *Semiconductor Science and Technology* **26**, 014037 (2011).
- [81] S.-W. Feng, Y.-Y. Chen, C.-M. Lai, L.-W. Tu, and J. Han, “Anisotropic strain relaxation and the resulting degree of polarization by one- and two-step growth in nonpolar a-plane gan grown on r-sapphire substrate,” *Journal of Applied Physics* **114**, 233103 (2013), URL <http://scitation.aip.org/content/aip/journal/jap/114/23/10.1063/1.4851755>.
- [82] C. Netzel, A. Knauer, and M. Weyers, “Impact of light polarization on photoluminescence intensity and quantum efficiency in algan and alingan layers,” *Applied Physics Letters* **101**, 242102 (2012).
- [83] H. Schömig, S. Halm, A. Forchel, G. Bacher, J. Off, and F. Scholz, “Probing individual localization centers in an InGaN/GaN quantum well,” *Phys. Rev. Lett.* **92**, 106802 (2004), URL <http://link.aps.org/doi/10.1103/PhysRevLett.92.106802>.
- [84] H. Wang, Z. Ji, S. Qu, G. Wang, Y. Jiang, B. Liu, X. Xu, and H. Mino, “Influence of excitation power and temperature on photoluminescence in ingan/gan multiple quantum wells,” *Opt. Express* **20**, 3932 (2012), URL <http://www.opticsexpress.org/abstract.cfm?URI=oe-20-4-3932>.
- [85] S. Hammersley, D. Watson-Parris, P. Dawson, M. Godfrey, T. Badcock, M. Kappers, C. McAleese, R. Oliver, and C. Humphreys, “The consequences

- of high injected carrier densities on carrier localization and efficiency droop in ingan/gan quantum well structures,” *Journal of Applied Physics* **111**, 083512 (2012).
- [86] B. Lee and L. W. Wang, “Band gap bowing and electron localization of $\text{Ga}_{1-x}\text{In}_x\text{N}$,” *Journal of Applied Physics* **100**, 093717 (2006), URL <http://scitation.aip.org/content/aip/journal/jap/100/9/10.1063/1.2364450>.
- [87] X. Wu, E. J. Walter, A. M. Rappe, R. Car, and A. Selloni, “Hybrid density functional calculations of the band gap of $\text{Ga}_{1-x}\text{In}_x\text{N}$,” *Physical Review B* **80**, 115201 (2009).
- [88] J. Chan, J. Liu, and A. Zunger, “Bridging the gap between atomic microstructure and electronic properties of alloys: The case of $(\text{In}, \text{Ga})\text{N}$,” *Physical Review B* **82**, 045112 (2010).
- [89] I. Gorczyca, S. Lepkowski, T. Suski, N. E. Christensen, and A. Svane, “Influence of indium clustering on the band structure of semiconducting ternary and quaternary nitride alloys,” *Physical Review B* **80**, 075202 (2009).
- [90] Q. Liu, J. Lu, Z. Gao, L. Lai, R. Qin, H. Li, J. Zhou, and G. Li, “Electron localization and emission mechanism in wurtzite $(\text{Al}, \text{In}, \text{Ga})\text{N}$ alloys,” *physica status solidi (b)* **247**, 109 (2010), ISSN 1521-3951, URL <http://dx.doi.org/10.1002/pssb.200945258>.
- [91] M. Funato and Y. Kawakami, “Excitonic properties of polar, semipolar, and nonpolar ingangan strained quantum wells with potential fluctuations,” *Journal of Applied Physics* **103**, 093501 (2008), URL <http://scitation.aip.org/content/aip/journal/jap/103/9/10.1063/1.2903592>.
- [92] D. Watson-Parris, M. Godfrey, P. Dawson, R. Oliver, M. Galtrey, M. Kappers, and C. Humphreys, “Carrier localization mechanisms in $\text{In}_x\text{Ga}_{1-x}\text{N}/\text{GaInN}$ quantum wells,” *Physical Review B* **83**, 115321 (2011).
- [93] T.-J. Yang, R. Shivaraman, J. S. Speck, and Y.-R. Wu, “The influence of random indium alloy fluctuations in indium gallium nitride quantum wells on the device behavior,” *Journal of Applied Physics* **116**, 113104 (2014).

- [94] M. Galtrey, R. Oliver, M. Kappers, C. Humphreys, P. Clifton, D. Larson, D. Saxey, and A. Cerezo, "Three-dimensional atom probe analysis of green- and blue-emitting $\text{In}_x\text{Ga}_{1-x}\text{N}/\text{GaN}$ multiple quantum well structures," *Journal of Applied Physics* **104**, 013524 (2008).
- [95] S. E. Bennett, D. W. Saxey, M. J. Kappers, J. S. Barnard, C. J. Humphreys, G. D. Smith, and R. A. Oliver, "Atom probe tomography assessment of the impact of electron beam exposure on $\text{In}_x\text{Ga}_{1-x}\text{N}/\text{GaN}$ quantum wells," *Applied Physics Letters* **99**, 021906 (2011).
- [96] K. H. Baloch, A. C. Johnston-Peck, K. Kisslinger, E. A. Stach, and S. Gradečak, "Revisiting the in-clustering question in InGaN through the use of aberration-corrected electron microscopy below the knock-on threshold," *Applied Physics Letters* **102**, 191910 (2013).
- [97] M. Moram and M. Vickers, "X-ray diffraction of III-nitrides," *Reports on Progress in Physics* **72**, 036502 (2009).
- [98] B. Monemar, P. Paskov, J. Bergman, G. Pozina, V. Darakchieva, M. Iwaya, S. Kamiyama, H. Amano, and I. Akasaki, "Photoluminescence in n-doped $\text{In}_{0.1}\text{Ga}_{0.9}\text{N}/\text{In}_{0.01}\text{Ga}_{0.99}\text{N}$ multiple quantum wells," *MRS Internet journal of nitride semiconductor research* **7**, 1 (2002).
- [99] T. Smeeton, M. Kappers, J. Barnard, M. Vickers, and C. Humphreys, "Electron-beam-induced strain within InGaN quantum wells: False indium cluster detection in the transmission electron microscope," *Applied physics letters* **83**, 5419 (2003).
- [100] M. J. Galtrey, R. A. Oliver, M. J. Kappers, C. J. Humphreys, D. J. Stokes, P. H. Clifton, and A. Cerezo, "Three-dimensional atom probe studies of an $\text{In}_x\text{Ga}_{1-x}\text{N}/\text{GaN}$ multiple quantum well structure: Assessment of possible indium clustering," *Applied physics letters* **90**, 061903 (2007).
- [101] A. Zunger, S.-H. Wei, L. Ferreira, and J. E. Bernard, "Special quasirandom structures," *Physical Review Letters* **65**, 353 (1990).
- [102] W. R. L. Lambrecht and B. Segall, "Anomalous band-gap behavior and phase stability of c - BN diamond alloys," *Phys. Rev. B* **47**, 9289 (1993), URL <http://link.aps.org/doi/10.1103/PhysRevB.47.9289>.

- [103] Y. Yeo, T. Chong, and M. Li, “Electronic band structures and effective-mass parameters of wurtzite gan and inn,” *Journal of Applied Physics* **83**, 1429 (1998).
- [104] S. Bloom, G. Harbeke, E. Meier, and I. Ortenburger, “Band structure and reflectivity of gan,” *physica status solidi (b)* **66**, 161 (1974).
- [105] M. Leszczynski, H. Teisseyre, T. Suski, I. Grzegory, M. Bockowski, J. Jun, S. Porowski, K. Pakula, J. Baranowski, C. Foxon, et al., “Lattice parameters of gallium nitride,” *Applied Physics Letters* **69**, 73 (1996).
- [106] O. Marquardt, C. Hauswald, M. Wlz, L. Geelhaar, and O. Brandt, “Luminous efficiency of axial inxgalxn/gan nanowire heterostructures: Interplay of polarization and surface potentials,” *Nano Letters* **13**, 3298 (2013), pMID: 23795779, <http://dx.doi.org/10.1021/nl4015183>, URL <http://dx.doi.org/10.1021/nl4015183>.